Title
Novel Frustrated Matter in Artificial Nanomagnets

Author
Saccone, Michael Douglas

Publication Date
2020

UNIVERSITY OF CALIFORNIA
SANTA CRUZ

NOVEL FRUSTRATED MATTER IN ARTIFICIAL NANOMAGNETS

A dissertation submitted in partial satisfaction of the
requirements for the degree of

DOCTOR OF PHILOSOPHY

in

PHYSICS

by

Michael Saccone

June 2020

The Dissertation of Michael Saccone
is approved:

Onuttom Narayan, Chair

Professor Joshua Deustch

Professor Peter Young

Dean Quentin Williams
Acting Vice Provost and Dean of Graduate Studies

Table of Contents

List of Figures **vi**

List of Tables **xxvi**

Abstract **xxvii**

Dedication **xxix**

Acknowledgments **xxx**

1 Introduction **1**

2 Artificial nanomagnets **4**

- 2.1 Array design . . . 5
  - 2.1.1 3D square ice . . . 5
  - 2.1.2 Trident ice . . . 7
  - 2.1.3 Cairo ice . . . 9
  - 2.1.4 Gaussian glass . . . 11
  - 2.1.5 Bethe glass . . . 13
- 2.2 Experimental methods . . . 15
  - 2.2.1 Sample fabrication . . . 15
  - 2.2.2 Photoemission electron microscopy . . . 19
- 2.3 Analysis . . . 20
  - 2.3.1 Magnetic structure factors . . . 20
  - 2.3.2 Debye-Hückel analysis . . . 21
  - 2.3.3 Crystallization order parameter . . . 26
  - 2.3.4 Simulations . . . 29
  - 2.3.5 Correlation Functions . . . 31
  - 2.3.6 Magnetic Susceptibility . . . 31

I Artificial Spin Ice 32

3 The Square Lattice: Monopole-like excitations 33
3.1 Introduction 33
3.2 Results 35
3.2.1 Thermal annealing 37
3.3 Real-time thermodynamics 39
3.4 Discussion 42

4 The Trident Lattice: Out of equilibrium relaxation 47
4.1 Introduction 47
4.2 Results 48
4.2.1 The dipolar trident lattice 48
4.2.2 Direct observation of thermal relaxation 51
4.2.3 Controlling the balance of competing interactions 53
4.2.4 Low-temperature configurations and magnetic structure factors 56
4.3 Discussion 58

5 The Cairo Lattice: Topological frustration and polarons 59
5.1 Introduction 59
5.2 Methods 61
5.3 Results 62
5.3.1 Energy landscape and micromagnetic simulations of coupling strengths 62
5.3.2 Thermal annealing and XMCD imaging 66
5.3.3 Emergent ice-rule and polaronic states 70
5.3.4 Correlations and short-range ordering 72
5.4 Discussion 74

II Artificial Spin Glass 76

6 A first attempt through Gaussian disorder 77
6.1 Introduction 77
6.2 Methods 79
6.3 Results 80
6.3.1 Thermal Annealing 82
6.3.2 Temperature-dependent moment fluctuations 87
6.4 Discussion 90

7 Increasing effective dimension via the Bethe lattice 92
7.1 Introduction 92
7.2 Methods 94
7.2.1 Sample fabrication and XMCD imaging 96
7.3 Results 96

7.3.1 Spin-spin correlations and ordering preferences 96
7.3.2 Effective dimension 98
7.4 Discussion 102

8 Conclusion **104**

Bibliography **107**

List of Figures

2.1 Thermally activated two-dimensional artificial square ice with height offsets between nanomagnets. (a) Tilted-sample scanning electron microscopy (SEM) image of an artificial square ice with an introduced height offset h, which can be varied from sample to sample, until the competing interactions J_1 and J_2 are equalized and an extensive spin ice degeneracy is achieved. Scale bar, 400 nm. (b) XMCD image of the same artificial square ice array. Nanomagnets with moments pointing toward the incoming x-rays (indicated by a yellow arrow) appear dark, while those opposing the x-ray direction appear with bright contrast. (c) The 16 possible moment configurations on a four-nanomagnet vertex are traditionally listed into four topological types. Without a height offset (h = 0 nm), the ice rule–obeying (two-in-two-out) type I and II configurations have a significantly different energy. Once a critical height offset is introduced, their energies are equalized and spin ice degeneracy is realized. Highlighted with magenta, cyan blue, and yellow frames in (b) and (c) are type I, type II, and type III vertices, respectively. 6

2.2 The dipolar trident lattice. a Scanning electron microscope image of a dipolar trident lattice (a = b = 50 nm, L = 450 nm, W = 150 nm). The black scale bar indicates a length of 450 nm. b X-ray magnetic circular dichroism (XMCD) image resolving moment configurations achieved in the trident lattice. Nanomagnets with a magnetization pointing toward the incoming X-ray propagation vector (indicated by a red arrow) appear dark, while moments opposing that direction appear bright. c Vertex and trident types listed with increasing energy. In both b, c green, yellow, and blue frames highlight the realizations of Type I, Type II, and Type III vertices, respectively. Regarding tridents, Type A and B tridents are highlighted with orange and magenta frames, respectively. d Minimization of dipolar interactions in an isolated trident building block would result in a Type A domination. On the other hand, nearest-neighbor nanomagnets at the four-nanomagnet vertices will prefer a head-to-tail moment alignment, which would result in clockwise or anti-clockwise vortices. Satisfying vertex interactions (creation of vortices or Type I vertices) results in frustration of trident moments. Satisfying trident interactions (creation of Type A tridents) results in two of nearest-neighbor vertex moments being aligned head-to-head (red circles) or tail-to-tail (blue circles). 8

2.3 (a) Dipolar Cairo lattice. We see dipolar-coupled Ising-type nanomagnets (stadium-shaped islands) occupy the sites of the pentagonal Cairo lattice (lines the background). Lattice parameters a = 472 nm and b = 344 nm are kept constant, while the lattice parameter c = 376 nm, 450 nm, 500 nm and 600 nm is varied, to tune the coupling strengths between the nanomagnets. (b) Scanning electron microscopy (SEM) image of one of the dipolar Cairo lattices consisting of nanomagnets with lengths and widths of 300 nm and 100 nm, respectively. The coupling parameter c can be varied, so that the balance between the coupling strengths J_1, J_2, J_3 and J_4 can be tuned at the nanoscale. The yellow scale bar indicates a length of 300 nm. 10

2.4 (a) Scanning electron microscope (SEM) image of part of an arrangement consisting of Ising-type nanomagnets with a length L = 300 nm, width W = 100 nm and a thickness t = 2.7 nm arranged onto a collinear ordered fashion with a nearest-neighbor edge-to-edge distance d = 80 nm. (b) SEM image of an array, where disorder in x- and y coordinates of the centers of nanomagnets is introduced in form of Gaussian distribution with a relative deviation σ = 100% around an average edge-to-edge distance of d = 80 nm. In addition to coordinate randomness, the same type of disorder is introduced for the rotational angle ϕ, ensuring maximum randomness possible in two dimensions. Circles representing the area in which spins will be designated nearest neighbor (NN, red line), next-nearest neighbor (NNN, green dashed line), and next-next-nearest neighbor (NNNN, blue dotted line) are drawn to denote categories used to calculate correlation functions. 12

2.5 (a) An illustration of a Bethe lattice with coordination number $k = 3$. Black circles represent nodes connected by grey lines. (b) A Cayley tree modified to be embedded in two dimensions. Each circle represents a step taken from the center of the lattice. (c) Scanning electron microscope (SEM) image of a Cayley tree consisting of Ising-type nanomagnets with a length L = 300 nm, width W = 100 nm and a thickness t = 2.6 nm. The yellow scale bar corresponds to 600 nm. The tree-like structure is best understood when looking at the inter-nanomagnet dipolar couplings, which are highlighted with red (ferromagnetic coupling) and blue lines (antiferromagnetic coupling) connecting centers of nanomagnets. . . 14

2.6 Sample fabrication process. Schematic drawing of the nanofabrication process to create artificial square ice patterns with a controlled height offset. In a first lift-off assisted e-beam lithography step, a chromium mask is generated (left panel). Then, reactive ion etching (RIE) is used to etch the Silicon (100) substrate through the chromium mask, which is followed by a second e-beam exposure (middle panel), which generates the desired permalloy nanomagnets (right panel). 16

2.7 Illustrations of correlated and uncorrelated emergent magnetic monopoles. (a) Illustration of an artificial spin ice with a correlated monopole. To illustrate similarity to a magnetic dipole, field lines are drawn outward from the positive +2q charge (red spheres) to the correlated negative -2q charges (blue spheres). Although other charges interact with the correlated charge, its proximity to its adjacent negative charge ensures that the two will dominantly interact with one another due to energetic stability. In contrast with the uncorrelated charge, most of the field lines converge nearby. (b) Schematic of converging field lines on an uncorrelated charge. The uncorrelated charge interacts with surrounding positive and negative charges. In isolation, the negative charge would tend to correlate with the nearby positive charge. The other randomly distributed charges screen this interaction, which can be seen in the field lines appearing more like those of a point charge and less like those of a dipole. This corresponds with this uncorrelated charge's long-range energy averaging to zero. 21

2.8 (a) Illustration of possible low-energy configurations, whether being a dilute gas of magnetic charges or a magnetic monopole crystalline ground state. Illustrations of possible low energy configurations. The neutral charge sites are left blank, +2*q* charges are red spheres, and negative -2*q*charges are blue spheres. Dilute gas of magnetic charges emerging from a spin glass ground state. There is no global ordering as is the case in our experiments. The charges are free to separate due to low Coulomb attraction compared to the chemical potential. (b) Magnetic monopole crystalline ground state. The charges freeze in one of two global configurations. 27

3.1 Thermally activated two-dimensional artificial square ice with height offsets between nanomagnets. (a) Tilted-sample scanning electron microscopy (SEM) image of an artificial square ice with an introduced height offset *h*, which can be varied from sample to sample, until the competing interactions J_1 and J_2 are equalized and an extensive spin ice degeneracy is achieved. Scale bar, 400 nm. (b) XMCD image of the same artificial square ice array. Nanomagnets with moments pointing toward the incoming x-rays (indicated by a yellow arrow) appear dark, while those opposing the x-ray direction appear with bright contrast. (c) The 16 possible moment configurations on a four-nanomagnet vertex are traditionally listed into four topological types. Without a height offset ($h =$ 0 nm), the ice rule–obeying (two-in-two-out) type I and II configurations have a significantly different energy. Once a critical height offset is introduced, their energies are equalized and spin ice degeneracy is realized. Highlighted with magenta, cyan blue, and yellow frames in (b) and (c) are type I, type II, and type III vertices, respectively. 36

3.2 Vertex populations, magnetic structure factors, and pinch-point analysis. (a to c) Low-energy moment configurations achieved after thermal annealing in artificial square ice arrays with height offsets of (a) h = 55 nm, (b) h = 145 nm, and (c) h = 180 nm. Scale bars, 1 μm. (d) Average vertex-type populations of thermalized artificial square ice, plotted as a function of introduced height offsets. Type I vertices dominate the configuration landscape up to an offset of 40 nm but continue to decrease in population with increasing height offset. A turning point is observed at an offset around 80 nm, where type I and II populations reach nearly identical values. The type II population continues to rise with increasing height offset and reaches twice the population of type I vertices at a height offset between 145 and 155 nm. As the height offset is increased beyond this critical value, type II vertices start to fully dominate the moment configuration in the spin ice. (e) Magnetic structure factor of an artificial square ice with a height offset of 145 nm. The structure factor is calculated from magnetic moment configurations recorded with PEEM imaging and exhibits pinch-point singularities, a typical feature of a magnetic Coulomb phase. The line scan through (q_x, q_y) = (2, 2) is fitted by a Lorentzian function (black curve in inset) from which an average spin-spin correlation length ξ = 10.8a ± 0.1 is derived. r.l.u., reciprocal lattice unit. 44

3.3 Temporal evolution of emergent magnetic monopoles. XMCD image sequence (recorded at T = 190 K) highlighting the thermally driven motion of emergent magnetic monopole defects (blue dots: $Q = -2q$, red dots: $Q = +2q$) in two-dimensional artificial square ice with a height offset h = 145 nm. Arrows of different colors (magenta, cyan blue, and yellow) indicate sequential changes in moment configurations at each instant of time (7, 14, and 21 s). The green bar and the big white arrow indicate a length of 1 μm and the incoming x-ray direction, respectively. Debye-Hückel theory and monopole crystallization . . . 45

3.4 Debye-Hückel behavior and crystallization of emergent magnetic monopoles. (a) Ratio of correlated to uncorrelated monopole defects observed in the h = 145 nm sample (black dots from Eq. 2.10) compared to the prediction from the Debye-Hückel theory with Bjerrum association corrections (blue stars from Eq. 2.6). The error bars correspond to real-time thermal fluctuations over observations of approximately 15 min at each temperature. The best fit is obtained for a magnetic charge Q = 9.765 $\times 10^{-12}$Am and a magnetization M = 54 kA/m in the Debye-Hückel analysis. The overall monopole density ρ as a function of temperature is shown as an inset. (b) Crystallization order parameter over the same temperature range. 46

4.1 The dipolar trident lattice. a Scanning electron microscope image of a dipolar trident lattice (a = b = 50 nm, L = 450 nm, W = 150 nm). The black scale bar indicates a length of 450 nm. b X-ray magnetic circular dichroism (XMCD) image resolving moment configurations achieved in the trident lattice. Nanomagnets with a magnetization pointing toward the incoming X-ray propagation vector (indicated by a red arrow) appear dark, while moments opposing that direction appear bright. c Vertex and trident types listed with increasing energy. In both b, c green, yellow, and blue frames highlight the realizations of Type I, Type II, and Type III vertices, respectively. Regarding tridents, Type A and B tridents are highlighted with orange and magenta frames, respectively. d Minimization of dipolar interactions in an isolated trident building block would result in a Type A domination. On the other hand, nearest-neighbor nanomagnets at the four-nanomagnet vertices will prefer a head-to-tail moment alignment, which would result in clockwise or anti-clockwise vortices. Satisfying vertex interactions (creation of vortices or Type I vertices) results in frustration of trident moments. Satisfying trident interactions (creation of Type A tridents) results in two of nearest-neighbor vertex moments being aligned head-to-head (red circles) or tail-to-tail (blue circles). 50

4.2 Thermal relaxation of the dipolar trident lattice. a–c XMCD images of the dipolar trident lattice undergoing thermally induced magnetic relaxation from a magnetically saturated state to a low-energy equilibrium configuration. The yellow scale bar indicates a length of 1 μm. d Experimentally obtained temporal evolution of vertex-type population extracted from XMCD images recorded at a constant temperature (T = 280 K). e Trident population plotted for the same relaxation process. 52

4.3 Tuning geometrical frustration in dipolar trident lattice. a–c XMCD images of equilibrium configurations of trident lattices with various lattice spacings (a = 50 nm = constant, b = 50, 75, and 100 nm) recorded at T = 300 K (blocking temperature T B = 310 K). The red arrow indicates the direction the X-ray propagation vector. The yellow scale bar indicates a length of 1 μm. d Experimentally observed vertex-type population plotted as a function of lattice parameter b. e Trident-type population plotted with increasing lattice parameter b. Experimental observations (filled symbols) are in satisfactory agreement with equilibrium Monte Carlo simulations (lines). The results reveal the transition from a Type I vertex and Type B trident-ordered state (b = 50 nm), to a disordered configuration (b = 75 nm) with no clear ordering preference, and, finally, to a Type A trident-ordered state (b = 100 nm), as the lattice parameter b is increased. The error bars represent standard deviations originating from ten experimental observations. 55

4.4 Experimental low-temperature observations. a–c XMCD images of equilibrium configurations of the dipolar trident lattice with various lattice spacings (a = 33 nm = constant, b = 33, 50, and 66 nm) recorded at T = 150 K (blocking temperature T B = 160 K). The red arrow indicates the direction the X-ray propagation vector. The yellow scale bar indicates a length of 600 nm. d–f Magnetic scattering patterns of moment configurations achieved in dipolar trident lattices with lattice parameters d a = 33 nm and b = 33 nm, e a = 33 nm and b = 50 nm, and f a = 33 nm and b = 66 nm, following thermal annealing. While long-range order with relatively sharp peaks is seen for b = 33 nm and b = 66 nm, the diffuse patterns for b = 50 nm indicate highly disordered moment configurations with short-range correlations. 57

5.1 (a) Dipolar Cairo lattice. We see dipolar-coupled Ising-type nanomagnets (stadium-shaped islands) occupy the sites of the pentagonal Cairo lattice (lines the background). Lattice parameters a = 472 nm and b = 344 nm are kept constant, while the lattice parameter c = 376 nm, 450 nm, 500 nm and 600 nm is varied, to tune the coupling strengths between the nanomagnets. (b) Scanning electron microscopy (SEM) image of one of the dipolar Cairo lattices consisting of nanomagnets with lengths and widths of 300 nm and 100 nm, respectively. The coupling parameter c can be varied, so that the balance between the coupling strengths J_1, J_2, J_3 and J_4 can be tuned at the nanoscale. The yellow scale bar indicates a length of 300 nm. 60

5.2 (a) Vertex types at four-nanomagnet vertices listed with increasing dipolar energy from Type I to Type IV. Type I and Type II are the so-called ice-rule obeying configurations and exhibit a zero net emergent magnetic charge at the vertex ($Q = 0$). Type III vertices break the ice rules and can be described as vertex defects that possess an non-zero net magnetic charge at the vertex ($Q = \pm 2q$). Type IV vertices have the highest energy and are never observed in our experiments. (b) Vertex types at three-nanomagnet vertices categorized with increasing dipolar energy from Type A to Type C. Red arrows mark those moments that are coupled with each other via J_3, while the red and black arrows are coupled via J_1. 64

5.3 Evolution of all relevant coupling strengths J_1 (blue dots and curve), J_2 (red dots and curve), J_3 (yellow dots and curve) and J_4 (purple dots and curve) plotted as a function of coupling parameter c. 65

5.4 XMCD images (recorded at T = 100 K) of a low-energy moment configuration achieved, following thermal annealing in (a) dipolar Cairo lattice with lattice parameter c = 376 nm, (b) c = 500 nm and (c) c = 600 nm. The incoming X-ray direction is indicated by a large red arrow. The XMCD dark-and-bright contrast gives a direct measure of the magnetization direction relative to the incoming X-ray propagation vector. Magnetic moments pointing towards the incoming X-rays appear dark, while moments opposing the X-ray direction appear bright. The blue bar indicates a length of 1 μm. (d) Vertex type populations at four-nanomagnet vertices plotted as a function of lattice parameter c. (e) Three-island vertex-type population under the variation of c. The error bars in (d) and (e) represent standard deviations of the mean resulting from XMCD measurements performed after each of the five repeated annealing cycles. The dashed curves in (d) and (e) represent the corresponding relative vertex type energies (from micromagnetic calculations) plotted as a function of c. 68

5.5 (a),(b) Magnetic moment and charge configurations achieved after thermal annealing for Cairo lattices with (a) c = 376 nm and (b) c = 600 nm. Positive $+q$ and negative $-q$ charges are depicted in with red and blue circles at three-nanomagnet vertices, respectively. Filled circles represent Type A vertices, while Type B vertices are shown with empty circles. Type III charge defects $\pm 2q$ are represented with red (+) and blue (-) crosses. Grey circles in (b) highlight screened charge defects. (c) Four-vertex plaquettes obeying the emergent ice-rule. Six variations of the two Type A (filled circles) and two Type B (empty circles) vertices within each plaquette obey this emergent ice-rule. (d) Percentage of screened Type III charge defects plotted as a function of lattice parameter c. The error bars represent standard deviations resulting from observations after each one of the five annealing cycles. 69

5.6 Correlation functions and extracted correlation lengths of all annealed ground states. All length scales are stated in proportion to the lattice parameter $a = 472$ nm. (a),(b) Spin-spin correlations between the ”p” subset of spins (a) and the ”s” subset of spins (b). (c) Charge-charge correlation function of all charges in the lattice. All correlation function seem to be exponentially encapsulated as a function of distance. (d) Correlation lengths as a function of lattice parameter c. The error bars represent standard deviations resulting from XMCD measurements performed after each of the five repeated annealing cycles. . . . 71

6.1 (a) Scanning electron microscope (SEM) image of part of an arrangement consisting of Ising-type nanomagnets with a length L = 300 nm, width W = 100 nm and a thickness t = 2.7 nm arranged onto a collinear ordered fashion with a nearest-neighbor edge-to-edge distance d = 80 nm. (b) SEM image of an array, where disorder in x- and y coordinates of the centers of nanomagnets is introduced in form of Gaussian distribution with a relative deviation σ = 100% around an average edge-to-edge distance of d = 80 nm. In addition to coordinate randomness, the same type of disorder is introduced for the rotational angle ϕ, ensuring maximum randomness possible in two dimensions. Circles representing the area in which spins will be designated nearest neighbor (NN, red line), next-nearest neighbor (NNN, green dashed line), and next-next-nearest neighbor (NNNN, blue dotted line) are drawn to denote categories used to calculate correlation functions. 78

6.2 XMCD images of a low-energy moment configuration achieved, following thermal annealing in (a) a fully ordered array of Ising-type nanomagnets, (b) a partially randomized array (σ = 30%) of parallel nanomagnets (no rotational disorder), (c) a fully randomized array (σ = 100%) of parallel nanomagnets (no rotational disorder), (d) a partially randomized array (σ = 30%) with rotational disorder, and (e) a fully randomized array (σ = 100%) with rotational disorder. The red scale bar indicates 1 μm. We see a transition from a long-range ordered anti-ferromagnetic moment alignment for the ordered arrays, showing the characteristic dark- and bright lines (a), to a long-range ordered ferromagnetic state for the arrays with only positional disorder (b-c), ending in short-range ordered phases, when full randomness is introduced with rotational disorder (d-e). . . . 81

6.3 Measures of correlation in the annealed systems. On the left are the absolute value of spatial correlation functions from the (a) non-rotated and (c) rotated samples plotted on a semi-logarithmic scale with their exponential fits indicated with dashed lines. The top right plot (a) displays the non disordered (red circles), partially disordered (green squares), and fully disordered non-rotated cases (blue diamonds), while the bottom left (c) contains the partially (red triangles) and fully (blue stars) disordered rotated systems. The dotted lines represent the fits used to extract the correlation lengths. On the right are the nearest neighbor correlations of the (b) non-rotated and (d) rotated systems as disorder is varied. 83

6.4 Temperature dependence of the non-rotated $\sigma = 100\%$ system (a, c, and e) and the rotated $\sigma = 100\%$ system (b, d, and f). The data points at and to the left of the teal dotted vertical lines are marked with crosses to indicate that they come from frozen configurations of spin islands. a-b) The characteristic relaxation time τ was recorded from a least squares fit of the autocorrelation function (Eqn. 6). The error bars are the standard error of this fit. c) and d) The dimensionless magnetic susceptibility for non-rotated and rotated patterns, respectively. χ was extracted from the spatial correlation function (Eqn. 5) at each frame. The averages from all frames are plotted with error bars representing standard deviations of the mean. The decreasing inverse susceptibility for non-rated patterns (blue squares) indicate long-range ferromagnetic ordering, which also visually evident in Fig. 6.2b. The grey dashed lines in c) and d) are linear Curie-Weiss fit, which imply a critical temperatures of $T_c = 298 \pm 28.8$ K for the non-rotated patterns and $T_c = 11.2 \pm 14.9$ K for the rotated patterns. e-f) The least squares fit to the spatial correlation function (Eqn. 2) produces the correlation length, ξ, whose standard error is represented by the error bars. The curves of best fit plotted as gray dashed lines correspond to critical exponents of $\nu = 1.38 \pm 0.620$ for the non-rotated case and $\nu = 1.82 \pm 0.986$ for the rotated case. 88

7.1 (a) An illustration of a Bethe lattice with coordination number $k = 3$. Black circles represent nodes connected by grey lines. (b) A segment of a Bethe lattice modified to be embedded in two dimensions. Each circle represents a step taken from the center of the lattice. (c) Scanning electron microscope (SEM) image of part of a Bethe lattice consisting of Ising-type nanomagnets with a length L = 300 nm, width W = 100 nm and a thickness t = 2.6 nm. The yellow scale bar corresponds to 600 nm. The tree-like structure is best understood when looking at the inter-nanomagnet dipolar couplings, which are highlighted with red (ferromagnetic coupling) and blue lines (antiferromagnetic coupling) connecting centers of nanomagnets. 93

7.2 (a)-(d) XMCD images of low-energy states achieved in four different Bethe structures, after thermal annealing. Moments pointing towards the incoming x-rays (big red arrow) will appear dark, while moments opposing the incoming x-ray direction will appear bright. The blue bar indicates a length of 600 nm. . 95

7.3 Neighbor correlations in randomized magnetic systems. In (a), the nearest-neighbor ($r/a = 1$), next-nearest-neighbor ($r/a = 2$), and next-next-nearest neighbor ($r/a = 3$) correlations are plotted for the most ferromagnetically ordered Bethe system (red crosses), the average Bethe system (black triangles), the most anti-ferromagnetically ordered Bethe system (blue circles) and the most disordered system from a previously investigated artificial spin system with Gaussian disorder[91] (gray squares). (b) Moment configurations of the Bethe structure with the highest degree of ferromagnetic-type ordering [red crosses and lines in (a)]. (c) Moment configurations of the Bethe structure with the strongest anti-ferromagnetic spin ordering [blue circles and lines in (a)]. 97

7.4 Effective dimension of randomized magnetic systems. (a) $m(r)$ and its fits are plotted to demonstrate effective dimension d. The purple and pink circles represent data from the Bethe lattices with the largest ($d = 2.72$) and smallest ($d = 2.51$) effective dimensions, respectively, while the curves of corresponding color are their fits. The dashed curve represents the average effective dimension of all 21 investigated Bethe structures ($d = 2.61$). The dashed grey line corresponds to the effective dimension ($d = 2.17$) of a system with mere Gaussian disorder [91]. (b) and (c) Representative graphs of interactions for systems with Gaussian disorder and a typical Bethe lattice, respectively. 99

List of Tables

6.1 Correlation length ξ and magnetic susceptibility χ for magnetic configurations achieved after thermal annealing, all summarized as a function of increasing disorder σ for structures without and with rotational disorder. The third column represents the correlation length as multiples of the largest dimension of the islands, L, for greater clarity of interpretation. The first two digits of the values are displayed due to imprecision from the limited sample size. 83

Abstract

Novel Frustrated Matter in Artificial Nanomagnets

by

Michael Saccone

Spin ice is a magnetic system in which the geometry of competing interactions makes it impossible to reach a single ground state. Ice states naturally occur in magnetic pyrochlore systems [12, 42, 81] which have since been emulated by manufactured metamaterials called artificial spin ice [105, 55, 63, 28, 30, 79, 87]. The field of artificial spin ice advanced patterned nanofabrication and X-ray magnetic circular dichromism (XMCD) imaging to the point where researchers can create nearly any two dimensional arrangement of bar magnets such as the kagome [55] and square [30] lattices, and visualize their magnetic orientations [30]. Here we explore three ice-like lattices, the 3D square [33], trident [32], and Cairo [90] lattices, their unique means of achieving geometric frustration, and the resulting emergent states of matter. Beyond ice type behavior, randomized frustration may lead to spin glass behavior [10]. Competing anti-ferro- and ferromagnetic interactions of ice systems lead to complex energy landscapes, slow thermal relaxation, and memory effects beyond simple magnetic hysteresis. We explore pathways of generating artificial spin glass to better experimentally understand this complicated state of matter. We begin by constructing an artificial spin system with Gaussian positional and uniform rotational disorder [91], analyze the nature of the magnetic correlation, then repeat the process through a tree like system with rotational disorder and heightened effective dimension

[89]. As a whole, these meta-materials confirm predictions of foundational statistical mechanics while posing new questions of their precise out of equilibrium dynamics and potential for device applications.

To my late grandma Shirley, and all else who nurture curiosity.

Acknowledgments

Many interesting stories, this one included, begin with a chance encounter. Meeting Alan Farhan at a colloquium 4 years ago inducted me into the world of nanomagnetism. He built my knowledge of the field from the foundations of spin ice, giving me the trust I needed to creatively explore research, but the insight to keep me focused on my goals. His research philosophies and Daniel Plainview impression will forever remain with me.

Research is the world of giants and people standing on their shoulders. However, nothing on earth grows taller than the California Redwood. It's no coincidence that I found plentiful academic support within the forest of UCSC. I could always trust my advisor, Onuttom Narayan, for his uncanny ability to pierce the densest of problems in seconds. His judgment served as an infallible compass in matters of research and school politics. Thank you for entrusting me with your old fig tree, which brought the joy of greenery into my cramped apartment (before economic circumstance forced me into an even smaller one). By complete chance, my two major conceptual subfields, spin ice and spin glass, owe a large part of their development to none other than two UCSC profs: Art Ramirez and Peter Young, respectively. Peter, thank you for your thorough patience and teaching me to follow a logical through line in the messy world of spin glass. Art, you never mince words and laid plain for me the labyrinthine process of research. You will forever possess the second best lattice license plate in the state of California. Josh Deustch, your cheerful approach to EM in my first quarter helped me feel included at a university I thought I had only been admitted to on a fluke. When you offered me a chance to speak at the colloquium (despite my novice understanding of research), any traces of imposter syndrome crumbled away.

Of course, no academic institution would exist without staff managing the entirety of the process. Ben, Cathy, Amy, and David, you all ensured our department constantly provided for its students, grads and undergrads alike. You all deserve the pay of professors and lengthy vacations, but unfortunately the latter is impossible without UCSC physics crumbling in your absence. Your dedication to centering students will constantly guide my pursuits in academia.

The social component of surviving grad school is indispensable. From our cohort's first session cramming for our qualifying exams, I knew I had found a wonderfully cooperative and welcoming peer group. Dana, you're my physics ride or die. Thank you for always answering your phone in a millisecond, inspiring me with your potent work ethic, and always having a pencil and dark chocolate handy. Dana, David, Sarah, Cole, Brett, Johny, Arturo, Drew, and Nico, we created a lasting camaraderie that gave me security in the often uncertain world of academics. Even if time scattered us to the wind, I still trust you all as a vital support network. To my motley crew of roommates and best friends, Jazz, Amy, and Mel, you are my chosen family. Jazz, after surviving a break in, sewage leaks, and countless hours of bad anime, I'm convinced we're immortal. Amy, thank you for never believing my self delusions and half baked assumptions about the world and always being down for fourth meal shenanigans (RIP Pacific st Taco Bell). Mel, we've done everything together. Retreats to the sierras, creating fantasy worlds, professional and emotional growth, the world is constantly new with you.

Further, the creation of new knowledge is nothing without teaching. My students consistently inspired me to better understand physics and pedagogy to ground knowledge in the conversation of learning. The chance talk through the fundamentals of our discipline restored my enthusiasm week after week. This goes doubly for my wonderful mentees, Isabel, Jacob, Arushi, Jeff, Kenny, Aika, and Rebecca. I can't wait to see what you create with your lives!

I would also like to thank my Finland dwelling friends for welcoming me to a new country and thriving research community for a summer. Sebastiaan, Alan (again), Rasmus, Felix, Maria, Urho, and Taddäus, your hospitality and lively lunchtime antics made me feel at home despite being flung thousands of kilometers from my birthplace.

I quite literally wouldn't be here without my family. My mom and dad always encouraged my explorations of science, very rarely refusing my constantly shifting, obsessive interests. Perhaps this was because my too permissive grandparents would always find some way to sneak me a book I wanted. It was an incredible privilege to grow up with this white, male, middle class security and my difficulty in achieving a PhD is nothing compared to those from more discouraging circumstances.

And finally, the greatest of thanks to my best friend, Jacob Serpa. We braved adolescence together, loving each other in ever shifting ideologies and geographies. You'll forever be a cornerstone of my life.

Chapter 1

Introduction

In magnetism, when interactions between magnetic moments are in conflict with each other, frustration arises. Systems incorporating frustrated interactions are characterized by extensive degeneracies, exotic emergent phenomena, and non-trivial ground states [42, 36, 16, 33]. Two prominent classes of these systems are spin ice [12, 42, 81] and spin glass [10, 68]. Though the two have numerous similarities and differences that will be explored within this thesis, their main distincion is as follows: spin ice systems have periodic interactions with multiple competing ground states while spin glass systems have aperiodic, randomized interactions with a single, if difficult to achieve, ground state. The distinct features of these systems are worth exploring for the sake of both fundamental science and industrial applications. The field of artificial spin ice emerged to fill this need [105]. Made of nanomagnets fabricated in virtually any two dimensional pattern imaginable, artificial spin ice creates analogues to complex systems that may be directly visualized and tweaked in parameter ranges previously inaccessible. Until recently, no researchers had sought an “artificial” version of spin glass, despite their shared origins as frustrated Ising type systems. Our work within is split into two predominant parts: one in which we explore systems with emergent disorder via ice type behavior and another in which we attempt to cleverly randomize systems to produce spin glass states.

Spin ices [12, 42, 81] represent a class of geometrically frustrated magnetic materials that, at low temperatures, enter a phase that is strongly dominated by short-range moment correlations and the absence of long-range order [81]. They are composed of corner-sharing tetrahedra, where the rare-earth ion moments occupy the corners of these tetrahedra. Local constraints force these moments to obey the so-called ice rules [42, 74] of two moments pointing in and two moments pointing out of each tetrahedron.

Artificial spin ice systems [69], comprising Ising-type nanomagnets, are printed metamaterials simulating ice like physics. Prominent examples are systems in which nanomagnets are lithographically arranged onto two-dimensional square [105, 63] and kagome [55, 87] geometries. In particular, artificial spin ices exhibiting thermally induced moment fluctuations [52, 29, 33] paved the way for a whole new line of research, where Ising-type nanomagnets are arranged onto novel two-dimensional magnetically frustrated geometries, leading to emergent phenomena that do not necessarily exist in nature.

Spin glasses have been another one of the most prominent examples of frustrated magnetism. They usually consist of randomized interactions creating a jumble of competing ferro- and antiferromagnetic order, leading to frustration [10, 68], degenerate energy landscapes and non-trivial pathways to their ground states [10]. In fact, the spin glass ground state question has long been an extensively investigated optimization problem [93, 41]. Theoretical spin glass models became, among other examples, the basis of error-correcting codes [96], problems of optimization [93], and brain science paradigms [82, 47]. Spin glass phase transition, most prominently characterized by a sharp cusp in ac-susceptibility measurements, became an area of intense research efforts since the early 1970's, both experimentally and theoretically [68]. The variety of characteristic phenomena in spin glass systems have mostly been investigated using macroscopic or spectroscopic characterization techniques, ranging from magnetometry [2], Mössbauer spectroscopy [84], to neutron diffraction and μSR spectroscopy [3]. Spin glass does not possess the regular and ordered geometries common to all previous artificial frustrated systems. This raises the question whether an artificial Ising spin glass system can be created from the same Ising-type nanomagnets arranged into random and disordered patterns. If so, what types of magnetic configurations are accessed, following thermal annealing protocols [34, 32]? How would the directly observable thermal fluctuations behave, as temperature and disorder are varied? Can a two dimensional spin glass be experimentally realized, despite theoretical predictions only discovering zero temperature glass phases [43, 8]?

These systems in which novel two-dimensional lattices comprising Ising-type nanomagnets are designed to exhibit exotic emergent phenomena beyond simple spin ice physics. Prominent examples are the observation of emergent magnetic charge screening and polaronic states in systems with mixed coordination numbers [38, 34, 18], field-induced phase coexistence in a quadrupole lattice [95], in addition to systems exhibiting topological frustration [26, 35, 94, 11] and the ability to directly control the degree of spin frustration at the nanoscale [32, 77]. All these artificial frustrated systems have also shown promise in potential applications in the field of spintronics and magnonics [106, 73, 40, 50, 9].

Chapter 2

Artificial nanomagnets

The conceit of artificial spin systems is that an array of nanomagnets can be designed so that their interactions and resulting magnetic ordering represent an interesting physics problem. Individual nanomagnets are shaped so that they consist of a single magnetic domain that switches direction under the influence of their neighbors' dipolar fields. Arrays of these magnets, tacitly referred to as "lattices" despite their finite nature, approximate Ising systems with interaction strengths set by how their constituent's positions and orientations alter the dipolar interaction strengths. The resulting nanomagnetic configurations may be recorded over various temperatures and system geometries using a combination of photon emission electron microscopy (PEEM) and the X-ray magnetic circular dichroism (XMCD) effect, both of which will be described below. The result is a system whose magnetic configuration may be entirely imaged within seconds within a select temperature range. The upper bound to this is the blocking temperature, the temperature where thermally induced moment reorientations of the nanomagnets start to occur at the time scale of several seconds. The lower bound is the freezing temperature, below which the time scale of nanomagnet reorientations is longer than several minutes. This expository section describes the design of the systems we studied, the details of their fabrication and magnetic imaging, and data analysis methods incorporated to discern ordering and frustration.

2.1 Array design

2.1.1 3D square ice

The square lattice in the context of artificial spin ice is a set of nanomagnets placed on the edges of a mathematical square lattice, as illustrated in Fig. 2.1. A height offset out of the plane is added to modify interaction strengths and encourage degeneracy, elevating this system to a "3D" square lattice. This quasi–three-dimensional lattice is realized by placing nanomagnets with lengths L = 400 nm, widths W = 100 nm, and thicknesses d = 3 nm onto a square lattice with lattice parameter a = 550 nm on top of a pre-etched silicon (100) substrate (Fig. 2.1a). While one set of nanomagnets (Fig. 2.1a) is grown on the base of the pre-etched substrate, the second set (Fig. 2.1a) is grown on top of plateaus whose height can be accurately controlled.

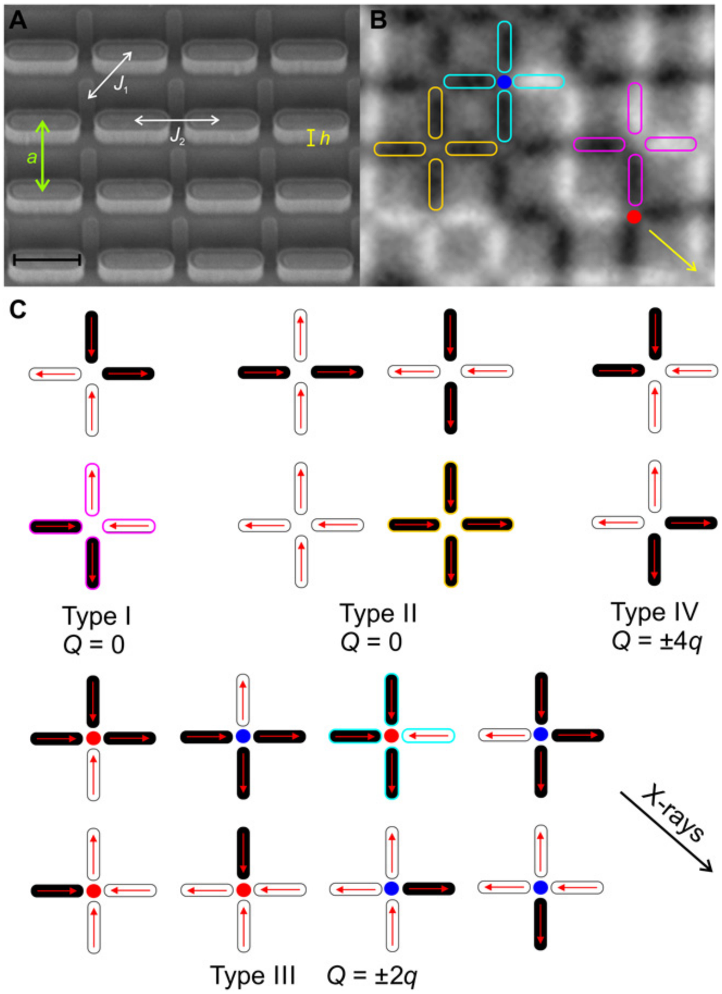

Figure 2.1: Thermally activated two-dimensional artificial square ice with height offsets between nanomagnets. (a) Tilted-sample scanning electron microscopy (SEM) image of an artificial square ice with an introduced height offset h, which can be varied from sample to sample, until the competing interactions J_1 and J_2 are equalized and an extensive spin ice degeneracy is achieved. Scale bar, 400 nm. (b) XMCD image of the same artificial square ice array. Nanomagnets with moments pointing toward the incoming x-rays (indicated by a yellow arrow) appear dark, while those opposing the x-ray direction appear with bright contrast. (c) The 16 possible moment configurations on a four-nanomagnet vertex are traditionally listed into four topological types. Without a height offset (h = 0 nm), the ice rule–obeying (two-in-two-out) type I and II configurations have a significantly different energy. Once a critical height offset is introduced, their energies are equalized and spin ice degeneracy is realized. Highlighted with magenta, cyan blue, and yellow frames in (b) and (c) are type I, type II, and type III vertices, respectively.

2.1.2 Trident ice

The trident lattice consists of three-nanomagnet (trident) building blocks periodically arranged in a perpendicular fashion (Fig. 2.2a). The “checkerboard” pattern of horizontal and vertical islands creates “pinwheel” like meeting points of adjacent tridents. The ordering at these pinwheels competes with that within each trident because a system of both low energy pinwheels and tridents is impossible, creating the frustration necessary for an ice state.

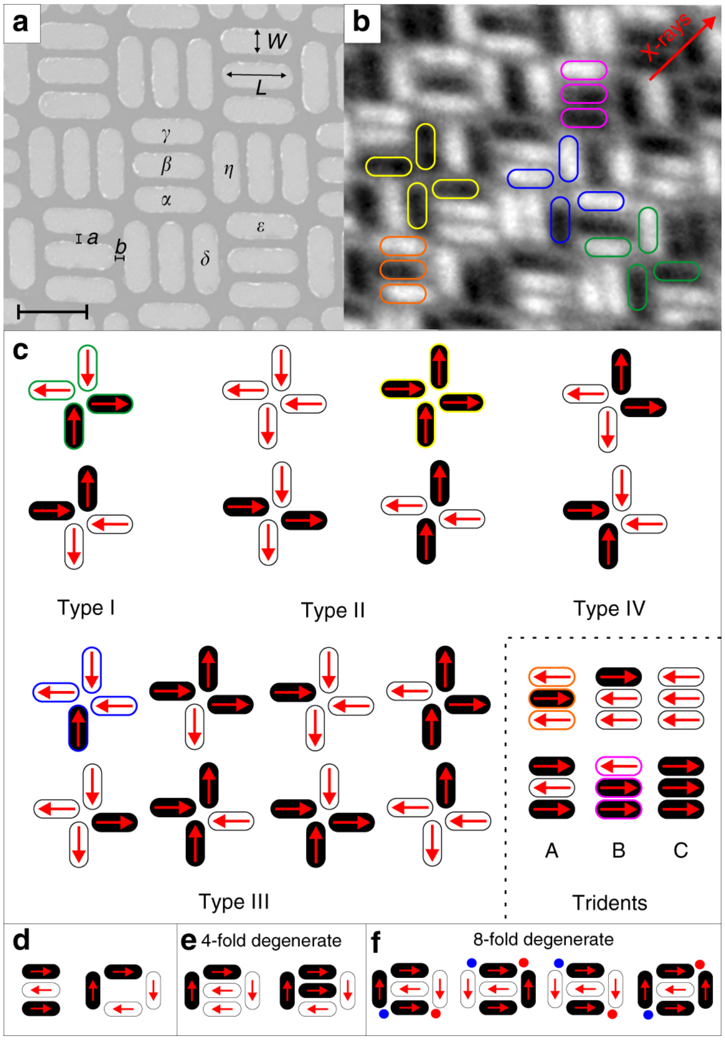

Figure 2.2: The dipolar trident lattice. a Scanning electron microscope image of a dipolar trident lattice (a = b = 50 nm, L = 450 nm, W = 150 nm). The black scale bar indicates a length of 450 nm. b X-ray magnetic circular dichroism (XMCD) image resolving moment configurations achieved in the trident lattice. Nanomagnets with a magnetization pointing toward the incoming X-ray propagation vector (indicated by a red arrow) appear dark, while moments opposing that direction appear bright. c Vertex and trident types listed with increasing energy. In both b, c green, yellow, and blue frames highlight the realizations of Type I, Type II, and Type III vertices, respectively. Regarding tridents, Type A and B tridents are highlighted with orange and magenta frames, respectively. d Minimization of dipolar interactions in an isolated trident building block would result in a Type A domination. On the other hand, nearest-neighbor nanomagnets at the four-nanomagnet vertices will prefer a head-to-tail moment alignment, which would result in clockwise or anti-clockwise vortices. Satisfying vertex interactions (creation of vortices or Type I vertices) results in frustration of trident moments. Satisfying trident interactions (creation of Type A tridents) results in two of nearest-neighbor vertex moments being aligned head-to-head (red circles) or tail-to-tail (blue circles).

2.1.3 Cairo ice

The concept of the Cairo lattice derives from a class of irregular pentagonal tilings. To create ice physics, the pentagons are chosen such that their vertices where four edges meet only contain right angles and their corners where three edges meet only contain 120° angles. The edges are replaced with nanomagnets which may be adjusted to balance the dominance of coordination four and three vertex ordering Fig. 2.3.

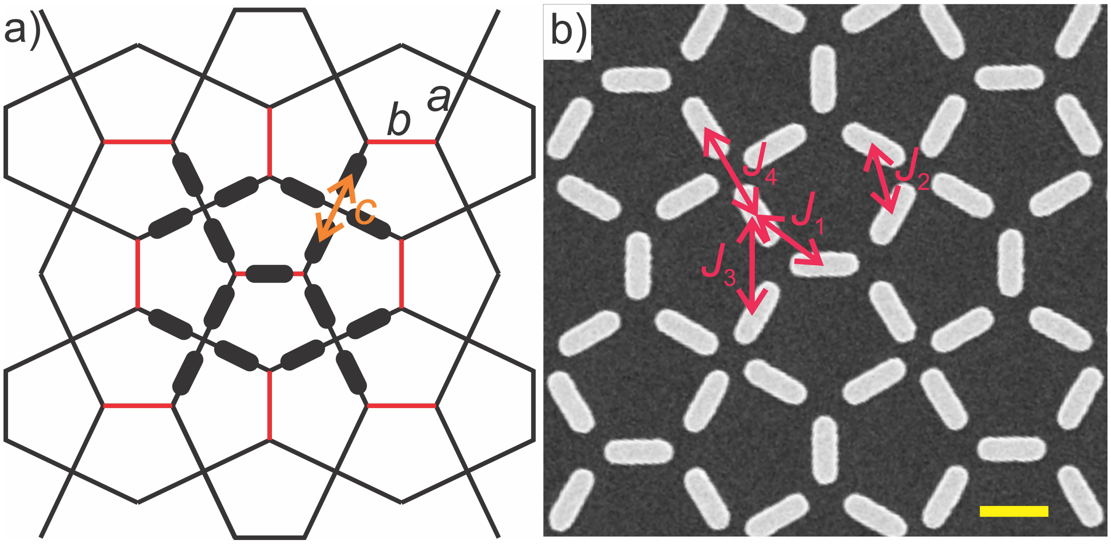

Figure 2.3: (a) Dipolar Cairo lattice. We see dipolar-coupled Ising-type nanomagnets (stadium-shaped islands) occupy the sites of the pentagonal Cairo lattice (lines the background). Lattice parameters $a = 472$ nm and $b = 344$ nm are kept constant, while the lattice parameter $c = 376$ nm, 450 nm, 500 nm and 600 nm is varied, to tune the coupling strengths between the nanomagnets. (b) Scanning electron microscopy (SEM) image of one of the dipolar Cairo lattices consisting of nanomagnets with lengths and widths of 300 nm and 100 nm, respectively. The coupling parameter c can be varied, so that the balance between the coupling strengths J_1, J_2, J_3 and J_4 can be tuned at the nanoscale. The yellow scale bar indicates a length of 300 nm.

2.1.4 Gaussian glass

To introduce a controlled disorder in the lattice, the islands are shifted from their lattice sites, $\mathbf{r}_{ij} = (W+d)i\hat{\mathbf{x}} + (L+d)j\hat{\mathbf{y}}$, where $W = 300$ nm is the nanomagnet width, $L = 100$ nm is the nanomagnet length, and $d = 80$ nm is nearest-neighbor edge-to-edge spacing (see Fig. 2.4). The x and y coordinates are displaced by values drawn from a normal distribution with a mean of zero and a standard deviation of varying percentages of d. For convenience, a standard deviation of xd is referred to as $\sigma = 100x\%$. Introducing disorder in the x- and y-coordinates results in patterns consisting of horizontal (non-rotated) nanomagnets arranged at random x and y sites. For simplicity, we call these structures the "*non-rotated*" arrays. Further disorder is induced by introducing the same type of randomness to the orientation angle ϕ of the nanomagnets (see Fig. 2.4b). The rotational distribution is defined around 0 degrees (islands are aligned along the x-axis) with a deviation of σ_ϕ=180°σ. Since XMCD contrast in the X-PEEM experiments is angle sensitive [30] with maximum contrast, when an angle of 0° is present between the incoming X-rays and the magnetization direction (zero contrast is present for an angle of 90°), the rotation of the nanomagnets is limited to a maximum of 80°. Again, for simplicity, we call these patterns with additional rotational disorder as the "*rotated*" arrays. Three kinds of disorder are investigated, σ= 0% (ordered), 30% (distorted) and 100% (disordered), for an edge-to-edge distance d = 80 nm. Furthermore, to ensure that nanomagnets do not overlap as a result of the introduced randomness, we define a minimum of 20 nm edge-to-edge distance when generating the random patterns. This minimum edge-to-edge distance also ensures a smooth and clean lift-off process in acetone. The overall number

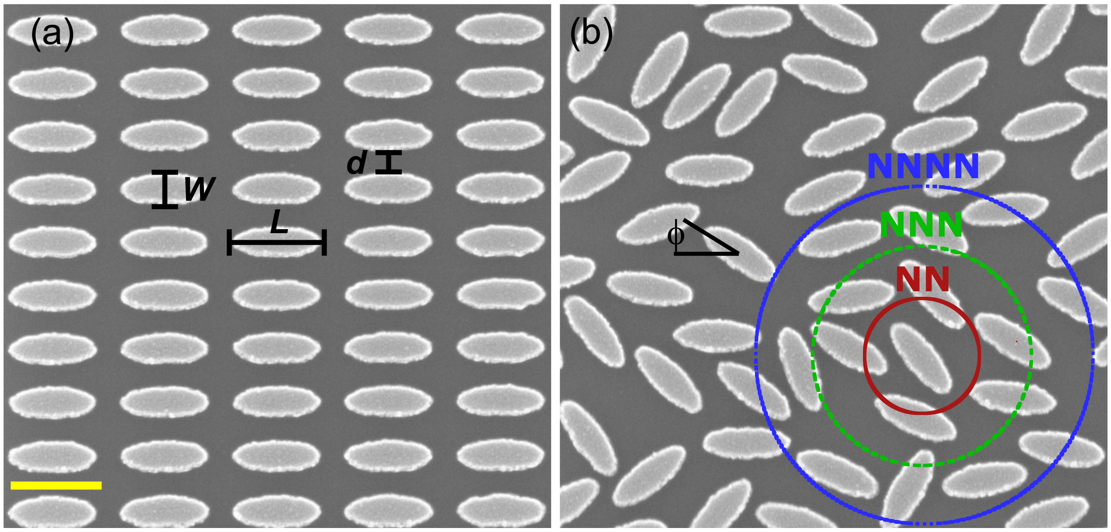

Figure 2.4: (a) Scanning electron microscope (SEM) image of part of an arrangement consisting of Ising-type nanomagnets with a length L = 300 nm, width W = 100 nm and a thickness t = 2.7 nm arranged onto a collinear ordered fashion with a nearest-neighbor edge-to-edge distance d = 80 nm. (b) SEM image of an array, where disorder in x- and y coordinates of the centers of nanomagnets is introduced in form of Gaussian distribution with a relative deviation σ = 100% around an average edge-to-edge distance of d = 80 nm. In addition to coordinate randomness, the same type of disorder is introduced for the rotational angle ϕ, ensuring maximum randomness possible in two dimensions. Circles representing the area in which spins will be designated nearest neighbor (NN, red line), next-nearest neighbor (NNN, green dashed line), and next-next-nearest neighbor (NNNN, blue dotted line) are drawn to denote categories used to calculate correlation functions.

of nanomagnets in each individual array was 7200, occupying areas of 26-30 μm^2. These system sizes are comparable to previously studied artificial frustrated spin systems [34, 29, 32], reducing potential finite-size effects to a negligible minimum.

2.1.5 Bethe glass

Cayley trees are finite subset of infinite Bethe lattices. A Bethe lattice (see Fig. 2.5a) is a tree-like graph with the helpful property that many models in statistical physics are exactly solvable on it [71]. To construct a Bethe lattice with a coordination number k, the number of connections per node, is chosen. k nodes are connected to a central lattice site. From each of these nodes $k-1$ new nodes are attached, then $k-1$ additional nodes are attached from each of those. This continues ad infinitum in the case of a Bethe lattice and to a finite number of layers for a Cayley tree. Fig. 2.5a shows an example where $k=3$. Multiple studies suggest a non-zero spin glass transition temperature could be obtained if spins would be mapped onto a Bethe lattice [101, 15, 60], which is here emulated by the patterning of Ising-type nanomagnets. To observe glassy dynamics, the spin glass transition temperature needs to be higher than the so-called blocking temperature T_B of the patterned nanomagnets, as spin freezing occurs below T_B [30, 31, 34, 32, 91].

Our nanomagnet samples mimic the essence of the Cayley tree's structure to create higher dimensional interaction networks. However, they differ from Cayley trees in three major ways. First, the spins interact via dipolar coupling. This increases the significance of next nearest neighbor effects, enabling the interaction network to leap from one branch to another. The finite-size nature of the fabricated Cayley trees serves as an advantage, as the increasing

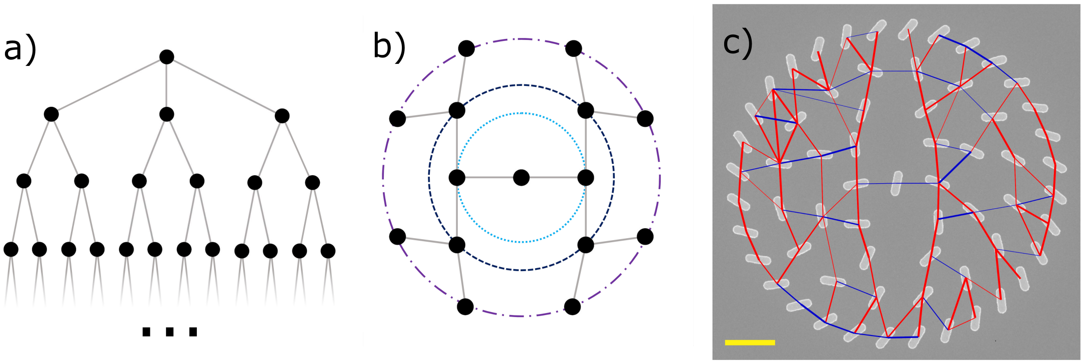

Figure 2.5: (a) An illustration of a Bethe lattice with coordination number $k = 3$. Black circles represent nodes connected by grey lines. (b) A Cayley tree modified to be embedded in two dimensions. Each circle represents a step taken from the center of the lattice. (c) Scanning electron microscope (SEM) image of a Cayley tree consisting of Ising-type nanomagnets with a length L = 300 nm, width W = 100 nm and a thickness t = 2.6 nm. The yellow scale bar corresponds to 600 nm. The tree-like structure is best understood when looking at the inter-nanomagnet dipolar couplings, which are highlighted with red (ferromagnetic coupling) and blue lines (antiferromagnetic coupling) connecting centers of nanomagnets.

network density would cause nanomagnets to overlap and interactions between next nearest neighbors to grow. Finally, the central spin is only given two neighbors to reduce the eventual crowding at the sample boundary. Implementing these compromises, we design modified Cayley trees for embedding in two dimensions (see Fig. 2.5b). The positions of the islands are uniformly spaced on concentric circles. The size of the circles is chosen to keep the distance of connected nodes constant (see gray lines in Fig. 2.5b). Here this sets the nearest neighbor distance to $a = 500$ nm. The orientation of the magnets is chosen to create random interactions while simultaneously supporting the Bethe structure. To do so, one nanomagnet per circle has its orientation selected randomly from a uniform distribution. The members of the same circle should not interact with one another, to maintain the tree-like structure. Thus, their orientations are chosen to place them perpendicular to the dipolar magnetic field of their direct neighbors within each circle. Circles are added until next-nearest neighbor interactions begin to break down the tree-like structure, allowing for five circles in our systems. In Fig. 2.5c we show a typical structure and the network of interactions created by its geometry.

2.2 Experimental methods

2.2.1 Sample fabrication

All lattices were fabricated using variations of electron beam lithography [34, 28]. This method of nanofabrication begins with a “resist” layer, typically a hydrocarbon glass that may be dissolved by the electrons in a desired pattern, on a silicon substrate. The electron beam precisely etches the shape of the nanomagnets, ferromagnetic material is deposited on the exposed substrate, and the remainder of the resist is dissolved, leaving only the patterned nanomagnet array on a non-magnetic substrate. The precise parameters vary as follows:

3D spin ice fabrication

The spin ice structures with height offsets were fabricated in two separate electron beam lithography exposure steps (Fig. 2.6) for the plateau definition and then for the nanomagnets. First, gold marks were fabricated on a silicon substrate to align both electron beam exposure steps to the same set of marks. PMMA (polymethyl methacrylate) 950k C2 was spun at 2000 rpm to give a thickness of 170 nm. The pattern for the raised plateau was then exposed with a Vistec VB300 electron beam lithography tool at 100 kV in four separate quadrants of the silicon wafer to allow four different etch depths on the same substrate. The PMMA was

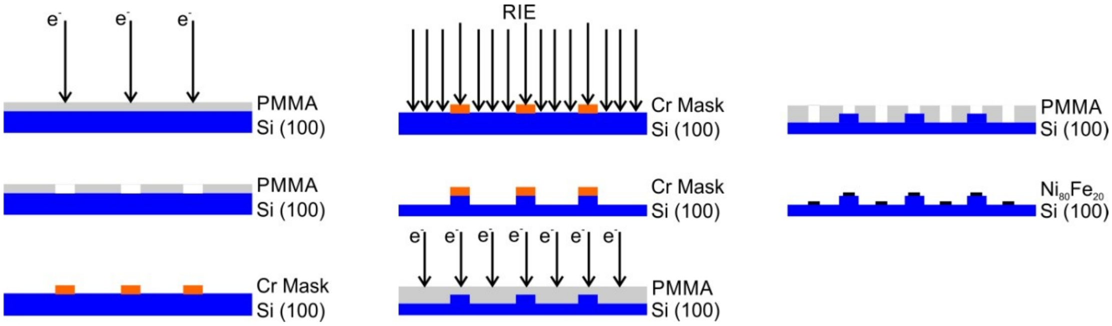

Figure 2.6: Sample fabrication process. Schematic drawing of the nanofabrication process to create artificial square ice patterns with a controlled height offset. In a first lift-off assisted e-beam lithography step, a chromium mask is generated (left panel). Then, reactive ion etching (RIE) is used to etch the Silicon (100) substrate through the chromium mask, which is followed by a second e-beam exposure (middle panel), which generates the desired permalloy nanomagnets (right panel).

then developed using a high-contrast cold development process consisting of 7:3 isopropyl alcohol (IPA):water solution ultrasonicated for 100 s. Cr (10 nm) was evaporated and lifted off to create the etch mask for the raised plateau. The silicon was etched in an Oxford Instruments reactive ion etcher with gas flow of 40-SCCM (standard cubic centimeter per minute) CHF3 and 8-SCCM SF6 at a pressure of 20 mtorr and a power of 50 W. Varying etch times gave the desired variation in etch depth. After stripping the Cr, PMMA was spun again on the substrate at 1000 rpm for the electron beam lithography exposure defining the nanomagnets. After exposure and cold development, a layer of 2.5-nm (TB = 160 K) and 3-nm (TB = 330 K) permalloy (Ni80Fe20) and a capping layer of 3 nm Al were evaporated and lifted off in dichloromethane. The exact values of the etched height offsets were determined using atomic force microscopy (AFM).

Dipolar trident lattices

A silicon (100) substrate was first spin-coated with a 70-nm-thick layer of polymethylmethacrylate resist. Then, trident lattices with various lattice spacings were defined onto the sample with a VISTEC VB300 electron beam writer. Next, using a Semicore SC600 e-beam evaporator, a ferromagnetic permalloy ($Ni_{80}Fe_{20}$) film was deposited at a base pressure of 1.2 x 10^{-7} Torr, which was followed by lift-off in acetone at a temperature of 50 °C. Thermally driven moment fluctuations in one set of artificial spin ice samples were realized by fabrication of ultrathin nanomagnets with length L = 450 nm and width W = 150 nm. The samples discussed in this work had thicknesses of 2.7 nm and 3 nm, resulting in blocking temperatures of 270 and 310 K, respectively. For low-temperature measurements, the blocking temperature was moved down to 160 K by preparing nanomagnets with lengths, widths, and thickness of 300, 100, and 2.4 nm, respectively.

Dipolar cairo lattice fabrication

Following e-beam exposure and development of a 70-nm-thick polymethylmethacrylate (PMMA) resist layer on a silicon (100) substrate, a 2.6 nm thick Permalloy ($Ni_{80}Fe_{20}$) thin film was deposited (base pressure: 2×10^{-7} Torr), along with a 2 nm thick aluminum capping layer to avoid fast oxidation of the sample. Next, a lift off process in acetone removed all unwanted magnetic material.

Spin glass fabrication

The samples were fabricated by lift-off assisted electron beam lithography. A 1 × 1 cm^2 silicon (100) substrate was first spin-coated with a 70-nm-thick layer of polymethylmethacrylate (PMMA) resist. Patterns of interest are then exposed on the substrate using a VISTEC VB300 electron beam writer. Next, a 2.7 nm thick ferromagnetic permalloy ($Ni_{80}Fe_{20}$) film was thermally evaporated at a base pressure of 1.4×10^{-7} torr, together with 1.5 nm thick aluminum capping layer, to avoid fast oxidation of the structures. This was followed by lift-off in acetone at a temperature of 50° C. The resulting nanomagnets had lengths L = 300 nm and widths W = 100 nm (see Fig. 2.4a-b). The elongated shape of the patterned single-domain nanomagnets are chosen, so that the magnetization within each individual nanomagnet can only point in one of two possible direction along the long axis of the nanomagnet. Thus, each nanomagnet represents an individual Ising macrospin. The nanomagnet dimensions are chosen to ensure a blocking temperature T_B of 190-240 K. Generally, we define the blocking temperature as the temperature where thermally induced moment reorientations of the nanomagnets start to occur at the time scale of several seconds [34, 29].

Bethe lattice fabrication

We used lift-off assisted electron-beam lithography to fabricate our samples (see Fig. 2.5). First, a 70-nm-thick layer of polymethylmethacrylate (PMMA) resist was spin-coated on top of a 1 × 1 cm^2 silicon (100) substrate. Designed Bethe patterns are then exposed on the substrate using a VISTEC EBPG 5000PlusES system. A 2.6 nm permalloy ($Ni_{80}Fe_{20}$) thin film was then evaporated at a base pressure of 3.6×10^{-6} mbar, together with a 1.5 nm thick aluminum capping layer, to avoid fast oxidation of the structures. This is followed by a lift-off process in acetone, where all unwanted material is removed from top of the substrate. This results in Bethe structures consisting of nanomagnets with lengths L = 300 nm and widths W = 100 nm. The size of the nanomagnets is chosen to ensure a mono-domain state and their elongated shape is set, so that the magnetization within each individual nanomagnet can only point in one of two possible direction along the long axis of the nanomagnet. Therefore, each individual nanomagnets represents a macroscopic Ising macrospin. Similar to our previous work [31, 34, 32, 33, 91], the individual volume of the nanomagnets is chosen so that the blocking temperature T_B = 140-180 K. With regard to XMCD imaging (see below), we define the blocking temperature as the temperature where magnetic moment re-orientations within the patterned nanomagnets start to occur at timescales equivalent to the time needed to record an XMCD image, which is about 7 seconds per image.

2.2.2 Photoemission electron microscopy

All measurements were performed using the cryogenic photoemission electron microscope PEEM3 at beamline 11.0.1 at the Advanced Light Source [25]. Magnetic images were captured by taking advantage of XMCD at the Fe L3-edge [97]. The obtained contrast is a measure of the projection of the magnetization on the X-ray polarization vector, so that nanomagnets with a magnetization parallel or anti-parallel to the X-ray polarization either appear black or white. Nanomagnets with moments having ±45° and ±135° angles with respect to the incoming X-rays appear dark and bright, respectively. In the case of the 3D systems, the silicon plateaus do not generate any disturbing background or shadow signal [75].

2.3 Analysis

2.3.1 Magnetic structure factors

Reciprocal space measurements, from Fourier transforms to scattering experiments, illustrate the dominant patterns in a system. Ordering patterns scattered throughout a system in real space separate as peaks in reciprocal space, with features such as peak width and location providing information about the consistency, dominance, and identity of real space patterns. The most relevant reciprocal space measurement for magnetic systems is neutron scattering. Since scattering on thin films is limited by their low mass, we use its mathematical equivalent, the magnetic structure factor.

This magnetic structure factor may assess whether or not a system is frustrated. Sharp scattering peaks correspond to system-wide order while diffuse peaks and reciprocal space filling patterns indicate disorder. The magnetic structure factor is calculated as

$$I(\mathbf{q}) = \frac{1}{N} \sum_{i=1}^{N} \sum_{j=1}^{N} \mathbf{S}_i^{\perp} \cdot \mathbf{S}_j^{\perp} \exp(i\mathbf{q} \cdot \mathbf{r}_{i,j}) \tag{2.1}$$

where $\mathbf{S}_i^{\perp} = \mathbf{S}_i - (\hat{\mathbf{q}} \cdot \mathbf{S}_i)\hat{\mathbf{q}}$ is the component of the spin vector of each island, $\mathbf{S}_i$, perpendicular to the reciprocal space vector $\mathbf{q}$; the unit vector is given by $\hat{\mathbf{q}} = \mathbf{q}/||\mathbf{q}||$; $\mathbf{r}_{i,j}$ is the vector from island i to j; and N is the total number of islands. This equation has the same form as in neutron scattering experiments and has previously been used to analyze artificial spin ice configurations.

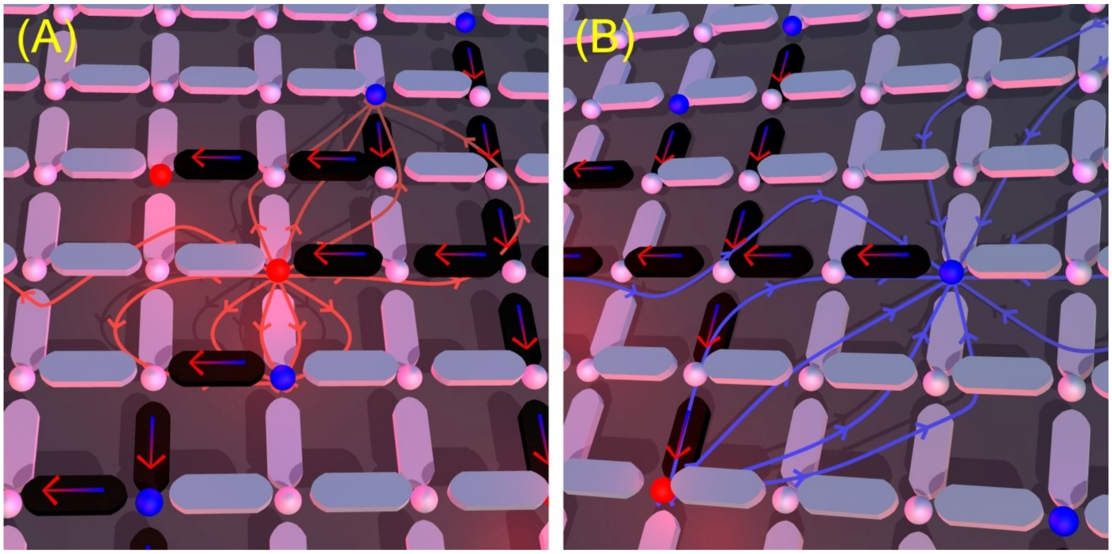

Figure 2.7: Illustrations of correlated and uncorrelated emergent magnetic monopoles. (a) Illustration of an artificial spin ice with a correlated monopole. To illustrate similarity to a magnetic dipole, field lines are drawn outward from the positive +2q charge (red spheres) to the correlated negative -2q charges (blue spheres). Although other charges interact with the correlated charge, its proximity to its adjacent negative charge ensures that the two will dominantly interact with one another due to energetic stability. In contrast with the uncorrelated charge, most of the field lines converge nearby. (b) Schematic of converging field lines on an uncorrelated charge. The uncorrelated charge interacts with surrounding positive and negative charges. In isolation, the negative charge would tend to correlate with the nearby positive charge. The other randomly distributed charges screen this interaction, which can be seen in the field lines appearing more like those of a point charge and less like those of a dipole. This corresponds with this uncorrelated charge's long-range energy averaging to zero.

2.3.2 Debye-Hückel analysis

To experimentally define and measure magnetic charges, we use the so-called dumbbell model [16, 62]. Dipoles are the fundamental source of magnetic interaction, but not the only means of accounting for magnetic properties. To better understand frustrated systems, it is common to use the relationship between electric dipoles and charges as an analogy to define a magnetic charge. This approach converts dipole moment to two charges with opposite sign at a finite separation, creating the appearance of a dumbbell. The magnitude of these charges Q

is the magnetic moment divided by the dipole length L. This approximation is well established enough to serve as a description of the charged excitations in our system.

The Debye-Hückel theory of plasmas [53] can be seen as a means to understand the liquid-gas transition and emergent magnetic monopole dynamics in pyrochlore spin ice. The basic idea is to describe the emergence of different categories of charges as carriers of energy. In this model of plasma, the charges emerge through Bjerrum ion pairing [58], splitting the population into correlated and uncorrelated charges. In the following analysis, the correlated monopoles are located adjacent another correlated monopole of opposite charge and otherwise homogeneously distributed, while the distribution of the uncorrelated monopoles is completely uniform. The density of the correlated charges, number per total charge sites, is predicted as a function of uncorrelated charge density, temperature, and material parameters. Levin's work on electrostatic correlations [58] outlines these predictions. The relationship between the correlated and uncorrelated charge density predicted by this theory is

$$\tilde{\rho}_2 = \frac{1}{4}\tilde{\rho}_1^2 \xi_2 \exp(2\beta\mu). \tag{2.2}$$

Here $\tilde{\rho}_1$ is the number density of uncorrelated charges, and $\tilde{\rho}_2$ is the number density of correlated charges. $\beta = 1/k_B T$, where T is the temperature and k_B is the Boltzmann constant. The chemical potential is $\mu = \frac{\partial f}{\partial \rho_1}$. ξ_2 is a constant with the dimension of volume,

$$\xi_2 = 4\pi \int_a^{R_{min}} r^2 dr \exp(\frac{\beta Q^2}{\varepsilon r}). \tag{2.3}$$

Q is the magnitude of a single charge, a is the lattice spacing, ε is the permittivity of free space, and V is the volume the charges may occupy. R_{min} is the value of r for which the integrand is a minimum. The free energy of this system is

$$f = -\frac{1}{4\pi a^3 \beta}\left[\ln(\kappa a + 1) - \kappa a + \frac{(\kappa a)^2}{2}\right] \tag{2.4}$$

where

$$\kappa = \sqrt{\frac{4\pi q^2(\rho_1 + \rho_2)\beta}{\varepsilon}}. \tag{2.5}$$

To deunitize these equations, we recognize common parameters $C_1 = \frac{4\pi Q^2}{k_B \varepsilon a}$, $C_2 = \frac{a^3}{V}$, $\rho_1 = \frac{\tilde{\rho}_1}{V}$, and $\rho_2 = \frac{\tilde{\rho}_2}{V}$. Elementary calculus gives $R_{min} = \frac{C_1 a}{8\pi}$. Simplifying, rewriting, and combining a few terms yields

$$\rho_2 = \frac{C_1^3 C_2}{128\pi T^3}\rho_1^2 \exp\left[\frac{1}{2\pi C_2}\left(\frac{1}{2\sqrt{\frac{T\rho_1}{C_1 C_2}}} - \frac{1}{2\rho_1 + 2\sqrt{\frac{T\rho_1}{C_1 C_2}}} - \frac{C_1 C_2}{2T}\right)\right]\int_2^{\frac{C_1}{4\pi T}} \frac{e^u}{u^4}\,du \tag{2.6}$$

In making the analogy to a magnetic system, ε is replaced with $1/\mu_0$.

This theory does not constrain total charge density or temperature. These parameters were drawn from experiment. We first measure the total charge density from XMCD data. ρ_1 may be written in terms of this total charge density, $\rho = \rho_1 + \rho_2$. This places ρ_2 on the right hand side of Eq. (2.6), converting it into a self-consistency problem. This is solved using the method of relaxation to produce pairs of ρ_1 and ρ_2 for given values of C_1 and C_2. Though C_1 and C_2 may be estimated from experimental parameters, better agreement with experimental data is attained by using them as parameters of best fit when comparing ρ_1 and ρ_2 pairs from the method above, deriving from a plasma theory, to the method below, only assuming the dumbbell approximation and utilizing the directly observed charge positions from XMCD images. Data will be fit by varying C_1 and C_2 as parameters over the entire temperature range measured. This will compare a plasma theory generated prediction for the correlated charge density with the magnetic configurations hypothesized to generate magnetic plasmas.

Correlated and uncorrelated charge densities can be determined through a calculation of the configurational energy and measurement of the total charge density. To do so, the square grid of dipoles is converted to a square grid of charges using the dumbbell model approximation [16]. The charges meeting at the corners of the square lattice are added together and approximated as one charge, $q_j = Q_j/2$. The energy of nearest-neighbor interaction is mapped onto a q_j^2 term, while the long-range interactions take a Coulomb form:

$$E = J_{nn} \sum_j q_j^2 + J_{lr} \sum_{j<k} \frac{q_j q_k}{r_{j,k}} \tag{2.7}$$

where $r_{j,k}$ is the distance between two charges in number of lattice parameters and all dimensional quantities are absorbed into J_{nn} and J_{lr}, which can be calculated as functions of dipolar and exchange energies (exchange energies absent in our systems) but will cancel in this analysis due to its geometric nature. The assertion that the system of charges acts like a plasma motivates a mean field approximation of the energy using correlated and uncorrelated charge populations as the average parameters. This mean field approximation allows the correspondence of the dumbbell energy to the correlated and uncorrelated charge densities.

Each configuration has an associated total energy in this approximation. The long-range interactions in the uncorrelated charges are between an equal number of positive and negative charges at random distances. These interactions average to zero, making the uncorrelated charge energy contribution just the energy of emerging from the vacuum, $E_1 = J_{NN} \sum_j q_j^2$. Every charge will either be +1 or -1 in the theoretical plasma and $N\rho_1$ charges are present, where N is the number of total charge sites. This simplifies the energy to $E_1 = NJ_{nn}\rho_1$. The correlated charges share this first term, but their long-range interactions are nonzero due to a constant adjacent charge of opposite sign. All other long-range interactions will cancel, making the total correlated energy $E_2 = NJ_{nn}\rho_2 - NJ_{lr}\rho_2$. The total energy is

$$\frac{E}{N} = J_{nn}(\rho_1 + \rho_2) - J_{lr}\rho_2 \tag{2.8}$$

In reality, correlations need not take place at just neighboring charges, which introduces another set of energies from decreasingly correlated charges. Fortunately, any weakly correlated charges will have nearly the same energy as the uncorrelated charges and any close to completely correlated charges will approach the correlated charge energy. Measuring density in this way rather than imposing a direct classification of correlated and uncorrelated charges maintains the information of these partially correlated charges. One could correct this approximation in the future by including more correlated charge groups, ρ_3, ρ_4, etc., that constitute the system.

Both the total charge density, $\rho = \rho_1 + \rho_2$, and the energy as represented by the individual charges are immediately calculable from the data. Isolating ρ_2 yields

$$\rho_2 = \frac{E}{NJ_{lr}} - \frac{J_{nn}}{J_{lr}}\rho \tag{2.9}$$

$$\rho_2 = \frac{1}{N}\sum_{j<k}\frac{q_j q_k}{r_{j,k}} \tag{2.10}$$

As expected, this is a quantity purely derived from the arrangement of the charges. Once ρ_2 is calculated, ρ_1 is what remains of the total charge density.

These two models state independent expressions for the correlated charge density. Eq. 2.6 corresponds to plasma theories of charge densities, while Eq. 2.10 relies on the verified dumbbell approximation and the experimental state of the spin ice system.

For this paper, the 145-nm offset array data at six temperatures were processed to yield charge densities as calculated by Eq. 2.10. Error bars for these values were derived from the standard deviation of the mean from real-time observations of thermal fluctuations for a period of approximately 20 min at each temperature. These densities were fitted to the Debye-Hückel theory as derived in Eq. 2.6 by scaling the magnetization of the dipoles within the expected range. C_1 and C_2 were left as fitting parameters, while the experimental data provided T and ρ.

2.3.3 Crystallization order parameter

As another measure of charge ordering, a crystallization order parameter was calculated as defined by Brooks-Bartlett et al. [13]

$$M_c = \left\langle \left| \frac{1}{N} \sum_{i=1}^{N} q_i \Delta_i \right| \right\rangle. \tag{2.11}$$

Here, the sum is taken over all N charge sites. The charge sites are checkered with $\Delta_i = \pm 1$ so that a complete tiling of the charge sites with alternating plus and minus charges would result in $M_c = 1$. In contrast, a low-temperature spin ice has an order parameter of zero because most charge sites are vacant, and any emerging charges are independent of one another. This parameter quantifies global charge ordering, complementing the more local measure of correlated versus uncorrelated charges. The temperature dependence of this parameter may be compared to curves from Brooks-Bartlett et al. [13] as further confirmation of spin ice behavior and lack of charge crystallization.

The presence of either a crystallized or spin ice ground state can be determined from the chemical potential of charges in relationship to the energy necessary to separate charges. If the chemical potential is small, then charges will dominantly populate the system without

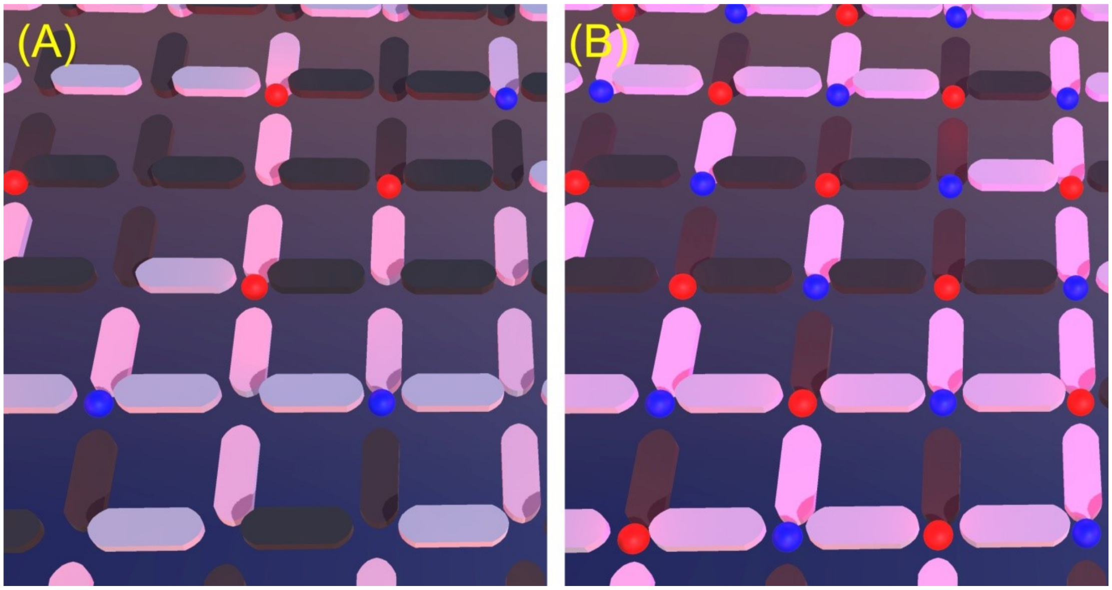

Figure 2.8: (a) Illustration of possible low-energy configurations, whether being a dilute gas of magnetic charges or a magnetic monopole crystalline ground state. Illustrations of possible low energy configurations. The neutral charge sites are left blank, +2q charges are red spheres, and negative -2$q$charges are blue spheres. Dilute gas of magnetic charges emerging from a spin glass ground state. There is no global ordering as is the case in our experiments. The charges are free to separate due to low Coulomb attraction compared to the chemical potential. (b) Magnetic monopole crystalline ground state. The charges freeze in one of two global configurations.

dissociating, forming a crystal of charges. Higher chemical potential prevents charges from emerging until the temperature is high enough to immediately dissociate introduced charges. This latter description is required to facilitate the low density of monopoles characteristic of a spin ice [16].

The critical chemical potential equals the energy of a single charge interacting with a lattice otherwise filled by a charge crystal. We have already labeled the interaction energy with a single opposing charge as J_{lr}. Units may be restored to these calculations by $J_{lr}\frac{\mu_0 m^2}{4\pi a^3}$ [16], where m is the magnetic moment of a single-spin island. Finding an entire crystal's ionic energy in relationship to this interaction strength is a well-explored numerical problem. The total energy is simply J_{lr} times an irrational determined by geometry number named the Madelung constant [16]. Here, we seek the Madelung constant divided by two, as the energy belongs equally to the charge in question and every other charge in the system. For the square lattice, this constant is about 1.61554 [7], which makes the critical energy $0.80777 J_{lr}$, translating to a critical chemical potential of $\mu_c = 0.80777 J_{lr}$. De-unitizing in the same fashion as in the study of Brooks-Bartlett et al. [13], we write $\mu_c^* = \frac{\mu_c}{J_{lr}} = 0.80777$. A system with a chemical potential below this will enter a charge crystal phase at low temperatures.

The chemical potential of the square ice can be found by flipping one spin in a charge-free state. Here, we assume that the energy of this spin is entirely found in dipole-dipole nearest-neighbor interactions. As seen in Fig. 2.8, J_1 is reduced by the height offset to approximately equal J_2. In the dipole approximation

$$J_2 = \frac{\mu_0 m^2}{4\pi a^3} |\hat{\mathbf{m}}_1 \cdot \hat{\mathbf{m}}_2 - 3(\hat{\mathbf{m}}_1 \cdot \hat{\mathbf{r}})(\hat{\mathbf{m}}_2 \cdot \hat{\mathbf{r}})|. \tag{2.12}$$

Because the spins referred to in 3D spin ice, $\hat{\mathbf{m}}_1$ and $\hat{\mathbf{m}}_2$, and the unit vector joining them, $\hat{\mathbf{r}}$, are all orthogonal when calculating the collinear J_2 interaction, all dot products are one, so $J_2 = 2J_{lr}$.

A single spin in a charge-free state has four favorable interactions and two unfavorable interactions, making the net energy $-2J_1$. Flipping the spin to create two charges negates these interactions, resulting in an energy of $2J_1$. This costs the system $4J_1$ for two charges, making the chemical potential $\mu = 2J_1 = 4J_{lr}$. This is de-unitized to $\mu^* = 4$, which is comfortably above the critical chemical potential. Charge crystallization is therefore not expected in 3D spin ice.

2.3.4 Simulations

Kinetic Monte-Carlo simulations were used to understand the relaxation of the trident lattice. We model each nanomagnet as an infinitesimally thin compass needle with a uniform magnetic moment density $|mL|$. The magnetic moment points along the long axis of the island. This description is equivalent to placing a magnetic charge at each end of the island [34, 62, 16]. The inter-island interaction is given by the Hamiltonian

$$H_{ij} = \frac{\mu_0 m}{24nL^2}\left[\frac{1}{||r_{ai} - r_{aj}||} - \frac{1}{||\vec{r}_{ai} - \vec{r}_{bj}||} - \frac{1}{||\vec{r}_{bi} - \vec{r}_{aj}||} + \frac{1}{||\vec{r}_{bi} - \vec{r}_{bj}||}\right], \tag{2.13}$$

where $\vec{r}_{ai}$ and $\vec{r}_{bi}$ are the locations of the positive and negative magnetic charge on the ith nanomagnet, μ_0 is the magnetic permeability, L is the island length, and $|m| = MV$ is the magnetic moment of each nanomagnet with M being the saturation magnetization and V the nanomagnet volume. The system size is 1200 islands, and only interactions with a magnitude of at least 2% of the nearest-neighbor interaction are included in the simulation (35 neighbors per spin).

To simulate the dynamics of the system, we use the kinetic Monte Carlo method [30, 28], which evolves the system through single-spin flips. A particular spin flip move is selected with a probability proportional to its rate. Assuming an Arrhenius-type switching behavior, the rate of a spin flip is given by $v = v_0 \exp(-E/k_B T)$, where k_B =8.62 x 10-5 eV K^{-1} is the Boltzmann constant, v_0 is the so-called attempt frequency, T is the temperature, and E is the reorientation barrier, which is equal to the intrinsic energy barrier E_0 plus half the dipolar energy gain associated with moment re-orientations (Eq. (2.13)). The simulation parameters, M = 240 kA m^{-1}, E = 0.887 eV, and v_0 = 1012 s^{-1}, were fit using the experimental relaxation results of Fig. 4.2. These values are in good agreement with previous studies on thermally activated artificial spin ice [34, 30, 28]. In addition to the assumption of a uniform system, where all nanomagnets have the same intrinsic energy barrier, we also investigated the role of disorder [30]. This is included by assuming a random variation in E_0, which follows a Gaussian distribution with mean E_0 = 0.893 eV and standard deviation $\sigma = 0.05$ eV.

To generate equilibrium configurations, for the results presented in Fig. 4.3, we use the parallel tempering technique [27, 98]. Replicas of the system are simulated at a number of temperatures simultaneously using kinetic Monte Carlo. After every Monte Carlo sweep a move is proposed which swaps the configuration of a pair of replicas at neighboring temperatures T_n and T_m. This move is accepted with a probability

$$P_{swap(n,m)} = \min\left\{1, \exp[-(\frac{1}{k_B T_m} - \frac{1}{k_B T_n})(E_n - E_m)]\right\}, \tag{2.14}$$

where E_n is the energy of replica n. The set of temperatures is selected such that the acceptance ratio of a swap move at each temperature is greater than 0.2. A value of M = 362 kA m^{-1} is used to obtain the results in Fig. 4.3. The equilibration time is estimated with the exponential autocorrelation time [108], τ. This is defined by the decay of the autocorrelation function, $\gamma \propto exp[-t/\tau]$. It is calculated for the autocorrelation function of the spin overlap function between two concurrent independent simulations, its absolute value, and the configuration energy throughout the parallel tempering simulation. Taking the largest of these calculated exponential autocorrelation times, the first 20 $\times \tau$ exp time steps are treated as equilibration time and discarded.

2.3.5 Correlation Functions

To quantify the ordering in the dipolar Cairo lattice and spin glass systems, the spatial correlation function, conventional in analysis of ferromagnets and anti-ferromagnets, was calculated:

$$C(\mathbf{r}_{ij}) = \langle S_i S_j \rangle_T \tag{2.15}$$

where $S_i = \pm 1$ to represent the Ising state of spin i, r_{ij} is the distance between spins i and j, and $\langle \cdots \rangle_T$ denotes a thermal average. This function was averaged over subsets of r_{ij} in methods appropriate to the system geometry to capture the dominant ordering.

2.3.6 Magnetic Susceptibility

The dimensionless magnetic susceptibility χ was calculated from this correlation using the fluctuation dissipation theorem [1]. This susceptibility χ was returned to appropriate dimensions by an additional factor m (the magnetic moment of a single spin, referred to as μ in the source):

$$\chi = \frac{m^2}{k_B T} \sum_{ij} C(\mathbf{r}_{ij}). \tag{2.16}$$

For the arrays discussed here, the magnetic moment m is calculated from a saturation magnetization, $M = 85$ kA/m found for similarly thin-film permalloy kagome structures [30], to be $m = 5.41 \times 10^{-18}$ Am^2.

Part I

Artificial Spin Ice

Chapter 3

The Square Lattice: Monopole-like excitations

3.1 Introduction

Two-dimensional artificial square spin ice [105] was initially introduced to mimic ice rule constraints, with the attractive prospect of directly visualizing the consequence of geometrical frustration using appropriate imaging techniques [105, 30]. However, it has been shown to lack typical spin ice degeneracy and residual entropy, mainly due to nonequivalent nearest-neighbor distances of nanomagnets meeting at four-nanomagnet vertices [105, 61]. Simple thermal annealing procedures have been shown to lead artificial square ice to access long-range ordered ground-state configurations [30, 79, 109]. The introduction of height offsets between the two sub-lattices of the square geometry has long been proposed as means to restore spin ice degeneracy by equalizing the relevant vertex interactions (J_1 and J_2 in Fig. 3.1a) [61], but a first experimental realization of such square ice systems could only be most recently achieved [75]. An extensive degeneracy was achieved, accessing the Coulomb phase, a state in which the energy of the system is in approximate correspondence to the Coulomb interaction of magnetic charges [16]. Specifically, each dipole moment is replaced by a dimer of two opposite magnetic charges. Configurations obeying the ice rule can be mapped onto a divergence-free field, which acts like a vacuum for local excitations that behave like emergent magnetic monopoles [16]. These monopoles arise in the form of ice rule breaking type III vertex defects (Fig. 3.1, b and c). These monopole defects result in an overall net magnetic charge $Q = \pm 2q$ residing at the corresponding four-nanomagnet vertex site (Fig. 3.1c). In contrast to that, ice rule–obeying moment configurations (types I and II) result in neutral $Q = 0$ vertex sites. So far, the patterned nanomagnets had blocking temperatures far above room temperature, making thermal annealing impractical and direct observations of the real-time thermodynamics of emergent magnetic monopoles impossible. Therefore, in analogy to previous work on athermal two-dimensional artificial spin ices [105, 59, 80], a demagnetization protocol was used to access quasi-frozen low-energy states in the patterned square ice arrays [75]. Previously, researchers have sought Coulombic behavior in the highly frustrated artificial kagome spin ice [55]. Although it does feature some analogies to pyrochlore spin ice [4, 17], the thermodynamics of emergent magnetic charge defects in this lattice have been shown to be strongly confined in nature [29], which is typical for all known two-dimensional artificial spin ice systems [30, 34]. The introduction of XY-mesospins, single domain circles of permalloy where the macrospin may point in any direction in the XY plane, within four-nanomagnet vertices [72] allows a two-dimensional square ice system to access a spin liquid-type phase. However, it is not clear how one can accurately account for emergent magnetic monopoles because the magnetic charge is less localized when compared to elongated spin islands. Thus, the gap toward a direct comparison to both theoretical and experimental studies on the statistical physics of pyrochlore spin ice and emergent magnetic monopoles is not overcome until an artificial square ice system with variable height offsets [75] is realized that exhibits moment fluctuations, ideally at experimentally accessible temperatures [34, 32]. In addition, these fluctuations are ideally visualized with an appropriate imaging technique.

Here, we present two-dimensional artificial square ice patterns consisting of nanomagnets with variable height offsets and thermally induced moment reorientations at experimentally accessible temperatures. This quasi–three-dimensional lattice is realized by placing nanomagnets with lengths $L = 400$ nm, widths $W = 100$ nm, and thicknesses $d = 3$ nm onto a square lattice with lattice parameter a = 550 nm on top of a pre-etched silicon (100) substrate (Fig. 3.1a). While one set of nanomagnets (Fig. 3.1a) is grown on the base of the pre-etched substrate, the second set (Fig. 3.1a) is grown on top of plateaus whose height can be accurately controlled. Magnetic configurations and thermal fluctuations are then directly visualized using synchrotron-based photoemission electron microscopy (PEEM) [97], using x-ray magnetic circular dichroism (XMCD; Fig. 3.1b) (24), which gives a direct measure of the magnetization direction of each individual nanomagnet. More details on sample fabrication and characterization are provided in Chapter 2.

3.2 Results

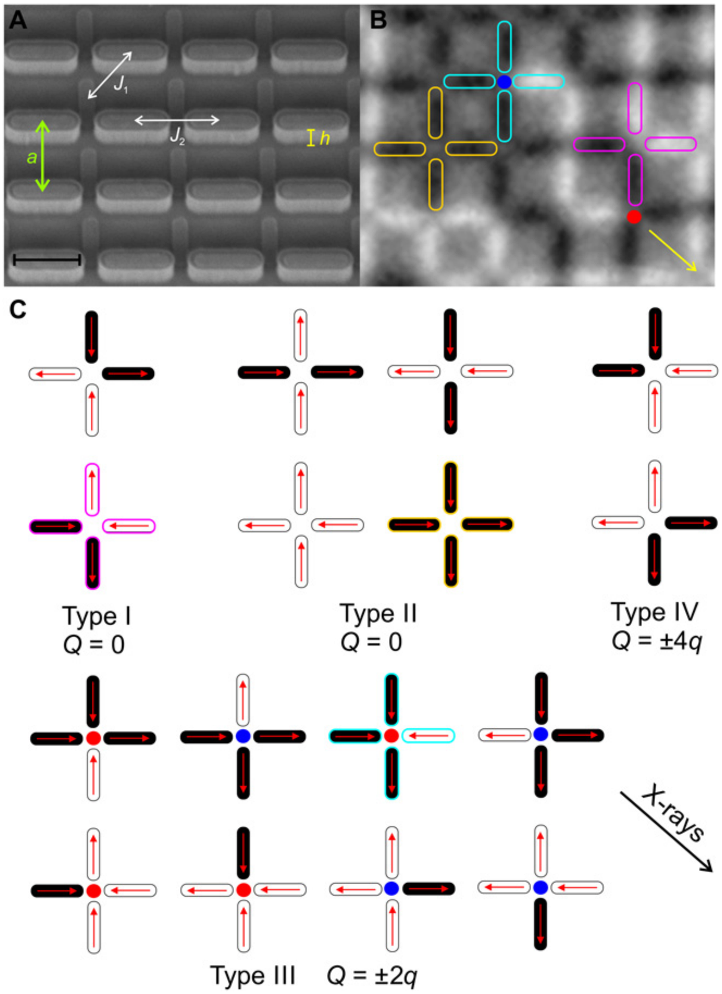

Figure 3.1: Thermally activated two-dimensional artificial square ice with height offsets between nanomagnets. (a) Tilted-sample scanning electron microscopy (SEM) image of an artificial square ice with an introduced height offset h, which can be varied from sample to sample, until the competing interactions J_1 and J_2 are equalized and an extensive spin ice degeneracy is achieved. Scale bar, 400 nm. (b) XMCD image of the same artificial square ice array. Nanomagnets with moments pointing toward the incoming x-rays (indicated by a yellow arrow) appear dark, while those opposing the x-ray direction appear with bright contrast. (c) The 16 possible moment configurations on a four-nanomagnet vertex are traditionally listed into four topological types. Without a height offset (h = 0 nm), the ice rule–obeying (two-in-two-out) type I and II configurations have a significantly different energy. Once a critical height offset is introduced, their energies are equalized and spin ice degeneracy is realized. Highlighted with magenta, cyan blue, and yellow frames in (b) and (c) are type I, type II, and type III vertices, respectively.

3.2.1 Thermal annealing

As a first step, we apply a thermal annealing protocol on our artificial square ice structures with various height offsets. The patterned structures had blocking temperatures around 330 K. Therefore, the sample is heated to 390 K, with a waiting time of 100 min, before cooling down below the blocking point to 300 K. The achieved moment configurations at all height offsets are then imaged (Fig. 3.2, a to c) and first analyzed in terms of vertex-type populations (Fig. 3.2d). The results reveal a transition from a long-range ordered (type I) ground state at low values of h [30] to increasingly disordered configurations with an increasing number of type III vertex defects as h increases. Furthermore, square ice systems with height offsets of 145 to 155 nm feature twice as many type II as type I vertices, indicating the restoration of spin ice degeneracy within this critical height offset regime. This is further confirmed by the average magnetic structure factor of an artificial square ice array with a height offset of 145 nm (Fig. 3.2e). The data reveal that the system accessed a phase that features properties of a cooperative paramagnet, exhibiting pinch-point singularities in the magnetic structure factor, indicative of algebraically decaying correlations resulting from the local ice rule [44]. That is, an effective Coulomb phase [44] is accessed with topological defects (type III vertices) that can be described as emergent magnetic monopoles [16, 44, 75]. The ice phase in square and kagome lattices produces "pinch points," structure factor singularities at the corners of frustrated regions of reciprocal space. Pinch points are visible in the structure factor map of the h = 145 nm sample, for example, at the point (2,2). To analyze this quantitatively, we extracted a line scan of the structure factor through the pinch point, from the point (3/2,5/2) to the point (5/2,3/2), plotted in

Fig. 3.2. Through a continuum approximation of spins on a pyrochlore lattice, it was previously determined that a line scan of pinch points should approximate a Lorentzian function scaled by the correlation length of the system [45, 75]. We calculated this correlation length, ξ, from a Lorentzian fit to the intensity profile

$$I(q) = A\frac{\xi^{-2}}{(q-q_0)^2+\xi^{-2}}+B \tag{3.1}$$

where q is the distance along the line scan, q_0 is the location of the pinch point, and A and B are constants. Fitting the data of Fig. 3.2E, we find A = 4.75, B = 0.25, and ξ = 10.8$a\pm$ 0.1. The locations of the pinch points are determined by the symmetry of the lattice. Analyzing one pinch point singularity in detail [we choose the point (q_x = 2, q_y = 2) for consistency with previous experiments [75]), we find an intensity distribution that fits well into a sharp Lorentzian curve (Fig. 3.2e) from which a spin-spin correlation length [75] of $10.8a \pm 0.1$ is obtained. The finite width of our pinch points is a result of both the finite size of the lattice and disruptions of ice rule ordering by topological defects. The correlation length calculated from the width is related to the average ice rule–obeying string length connecting emergent magnetic monopole defects. Magnetic structure factors as a function of introduced height offsets are shown in fig. S3. As we increase the height offset between nanomagnets beyond the critical regime of 145 to 155 nm, we observe a transition toward phases featuring multidomain type II vertex patterns (Fig. 3.2c).

3.3 Real-time thermodynamics

In pyrochlore spin ice, emergent magnetic monopoles are predicted to behave as classical magnetic analogs to electric charges with a Coulomb-type interaction [16]. Evidence regarding their existence and behavior has relied heavily on scattering or macroscopic measurement techniques [37, 66], while the macroscopically degenerate artificial square ice discussed here offers the unique opportunity to shed light into the dynamic behavior of emergent magnetic monopole defects via real-space imaging. For this, we fabricated a second sample with a height offset of 145 nm and a blocking temperature of 160 K consisting of nanomagnets with length L = 400 nm, width W = 100 nm, and thickness d = 2.5 nm. Obtaining XMCD image sequences (7 to 10 s per image) at various temperatures between 160 and 210 K, we are able to directly visualize real-time thermal fluctuations and motion of emergent magnetic monopoles (see Fig. 3.3) and characterize their temperature-dependent behavior. In Fig. 3.3, a short sequence of XMCD images recorded at 190 K is shown, with a time frame of 14 s separating them. Following sequential changes in the XMCD contrast, when going from frame to frame (marked by correspondingly colored arrows in each frame of Fig. 3.3), we are able to track the motion of emergent magnetic monopoles as a function of time. We find that the motion of magnetic monopoles is free in all possible directions, with the only limitation being that certain motion steps are unlikely, as they would require the generation of type IV ($Q = \pm 4q$) defects, which is energetically unfavorable and never detected within all our observations. This “free” motion of emergent magnetic monopoles in a two-dimensional lattice with a critical height offset between nanomagnets stands in contrast to the purely two-dimensional artificial square ice (h = 0 nm), where magnetic monopoles are highly confined within domain boundaries separating type I domains. As a consequence of this restricted motion, the concept of freely moving Coulomb-type magnetic monopoles becomes highly questionable in purely two-dimensional spin ice systems [30, 104].

A collection of free charges should act according to the predictions of a plasma theory. These theories typically account for a process that dissociates dipoles into monopoles, much like electrolytes dissolve in a solution. Commonly used to model electrolyte and plasma systems, the Debye-Hückel theory [53] describes a plasma in which charge pairs may spontaneously enter the system and separate through Bjerrum-ion dissociation [58]. While the Debye-Hückel theory was successfully applied in modeling the dynamics of emergent magnetic monopoles in pyrochlore spin ice [17, 48], it is only with a thermally activated and macroscopically degenerate artificial square ice realized in this work that a direct visual interpretation of magnetic monopole motion within the framework of the Debye-Hückel theory can be delivered. Using this theory, we view the square ice lattice as a plasma of emergent magnetic charges. Charge populations (see inset in Fig. 3.4a for the overall monopole density plotted as a function of temperature) are divided into correlated and uncorrelated magnetic monopoles. Correlated charges are uniformly distributed in pairs, while uncorrelated charges are simply uniformly distributed (Fig. 2.7). Analyzing the aforementioned XMCD sequences, we extract both the densities of correlated (ρ_2) and uncorrelated (ρ_1) magnetic monopoles (see section 2.3.2) and plot the ratio ρ_2/ρ_1 as a function of temperature (black dots in Fig. 3.4a calculated from Eq. 2.10). This experimentally derived temperature dependence is in good agreement with the theoretical prediction (blue stars in Fig. 3.4a calculated from Eq. 2.6 in section 2.3.2), implying Coulombic-type interactions between the emergent magnetic monopoles. The agreement is achieved for an emergent magnetic monopole charge of $Q = 9.765 \times 10^{-12}$Am, which corresponds to a saturation magnetization of the permalloy nanomagnets of $M \approx 54$ kA/m. This value is substantially lower than the saturation magnetization for bulk permalloy, but it is not far off from 85 kA/m reported for patterned 3.2-nm-thick permalloy kagome structures [28]. A similar reduction in the saturation magnetization has been reported on patterned FePd thin films [65], which indicates that the apparent decrease in M can be attributed to smaller activation volumes that initiate moment reversals, once thermal effects gain significance in these nanostructured thin films.

The Bjerrum association approach assumes charges to be either correlated or uncorrelated. However, images of charge distributions reveal that charges also exist in more complicated states [107]. For example, charges may slightly correlate by aligning with next-next nearest neighbors, lie adjacent to two or more charges, or any other combinatoric possibilities. To investigate the extent of charge ordering, a crystallization order parameter (see chapter 2.3.3) [13] is calculated and plotted versus temperature in Fig. 3.4b. Because this parameter remains well below 1, we can conclude that the global ordering needed for crystallization is absent. The parameter increases to an asymptotic value at higher temperatures due to crowding of magnetic charges into cohabiting neighboring sites. The jump toward this asymptote occurs around 180 K, the temperature associated with the spike in the charge density ratio. Both total monopole density (Fig. 3.4a, inset) and the ρ_2/ρ_1 ratio (Fig. 3.4a) show a sudden rise at 180 K. Barring any complex, non-monotonic behavior missed by theoretical studies and previous experiments, this jump in total monopole density is likely a result of the limited field of view of approximately 17 μm. The large standard deviation in this measurement corroborates this. The ρ_2/ρ_1

ratio implicitly depends on total charge density, adding an outlier within otherwise monotonic temperature dependencies. The lack of monopole crystallization in our quasi–three-dimensional artificial square ice stands in contrast to charge crystallites observed in two-dimensional artificial kagome spin ice [109]. This can be attributed to the chemical potential in this type of system being well above the critical chemical potential [107] of $\mu_c = 0.80777$ under which charge crystallization can be expected.

3.4 Discussion

Although the finite-temperature blocking temperature of the patterned nanomagnets prevents measurements of dynamics at even lower temperatures, a comparison of chemical potential to crystallization energy leads us to conclude that this system supports a spin ice ground state. A system of magnetic charges on the pyrochlore lattice with a tunable chemical potential is expected to form low temperature arrangements of alternating positive and negative charges (Fig. 2.8) when the chemical potential is smaller than a critical value [13]. By basic energetic considerations (see [13] and section 2.3.3), the critical chemical potential is half the Madelung constant of the lattice in question. Alternatively, if the chemical potential is high compared to the energy required to ionize a pair of charges, then the pair will separate at temperatures where charges form in the system. Although the square ice chemical potential is less than that of the pyrochlore lattice, it is still comfortably higher than the critical value (see chapter 2.3.3), coinciding perfectly with the qualitative behavior of the order parameter and suggesting the existence of a spin ice ground state and pure Coulomb phase with zero ice rule violations at lower temperatures.

The Coulomb phase is further validated by the data's correspondence to Debye-Hückel theory. At its core, this theory describes point charges that interact with one another via Coulomb's law. These charges can emerge and disappear within the system via thermal activity or whenever energetically favorable. Because they are attracted to opposite charges and repelled by charges of the same sign, some portion of the charges spend more time near one another. This portion of the charges is referred to as the correlated charge density, leaving the rest as the uncorrelated charge density. Combining the fundamental physics of Poisson's equation with charge density governed by Maxwell-Boltzmann statistics, these point charge densities are predicted to change as a function of temperature. The magnetic defects observed in our study obey these fundamental laws of thermodynamics and electrostatics through their agreement with the Debye-Hückel theory. The Coulomb interaction at the core of this theory further affirms the defects' identity as emergent monopoles.

The current study focuses on field-free thermodynamics of emergent magnetic monopoles in extensively degenerate artificial square ice with height offsets between nanomagnets. Future research might take advantage of the real-space imaging aspect to explore field-dependent non-equilibrium response of emergent magnetic monopoles and establishing links to electro-diffusion theories [51]. Furthermore, advances in nanofabrication techniques will allow researchers to fabricate similar artificial square ice patterns consisting of significantly smaller nanomagnet sizes and lower blocking temperatures [4] that will finally answer the long-standing question regarding the true spin ice ground state [81, 78].

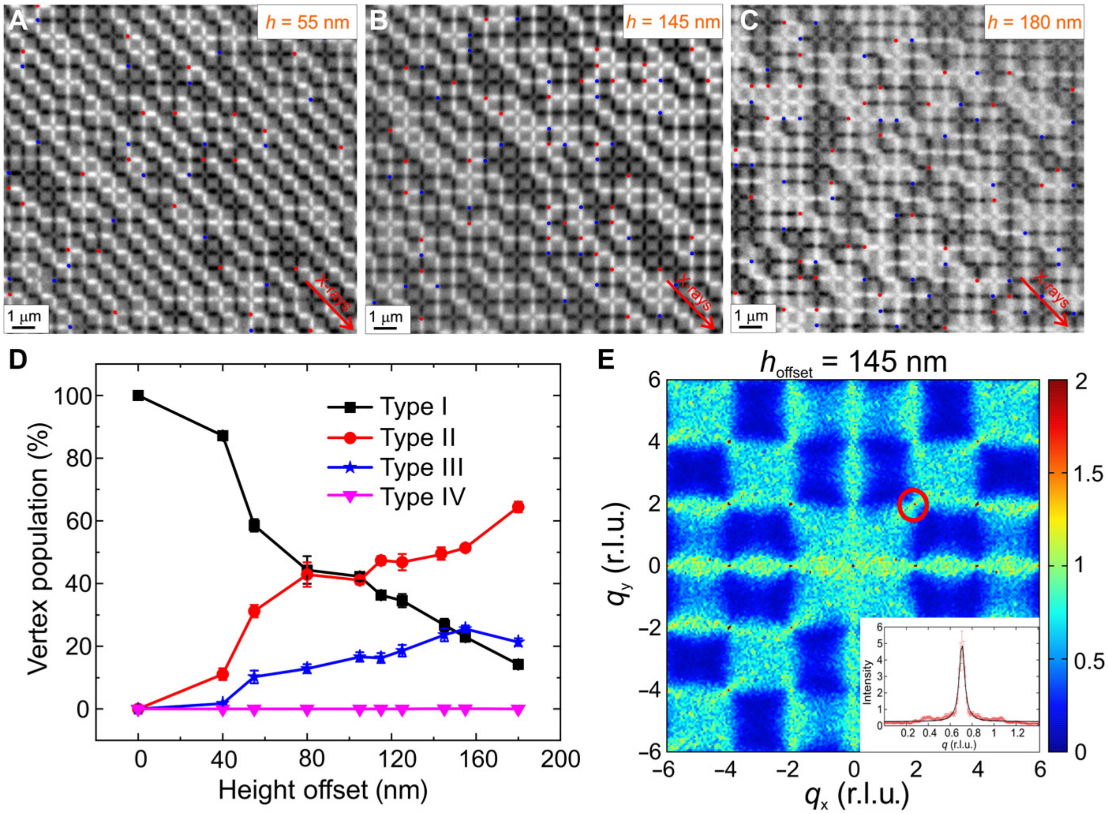

Figure 3.2: Vertex populations, magnetic structure factors, and pinch-point analysis. (a to c) Low-energy moment configurations achieved after thermal annealing in artificial square ice arrays with height offsets of (a) h = 55 nm, (b) h = 145 nm, and (c) h = 180 nm. Scale bars, 1 μm. (d) Average vertex-type populations of thermalized artificial square ice, plotted as a function of introduced height offsets. Type I vertices dominate the configuration landscape up to an offset of 40 nm but continue to decrease in population with increasing height offset. A turning point is observed at an offset around 80 nm, where type I and II populations reach nearly identical values. The type II population continues to rise with increasing height offset and reaches twice the population of type I vertices at a height offset between 145 and 155 nm. As the height offset is increased beyond this critical value, type II vertices start to fully dominate the moment configuration in the spin ice. (e) Magnetic structure factor of an artificial square ice with a height offset of 145 nm. The structure factor is calculated from magnetic moment configurations recorded with PEEM imaging and exhibits pinch-point singularities, a typical feature of a magnetic Coulomb phase. The line scan through (q_x, q_y) = (2, 2) is fitted by a Lorentzian function (black curve in inset) from which an average spin-spin correlation length ξ = 10.8a ± 0.1 is derived. r.l.u., reciprocal lattice unit.

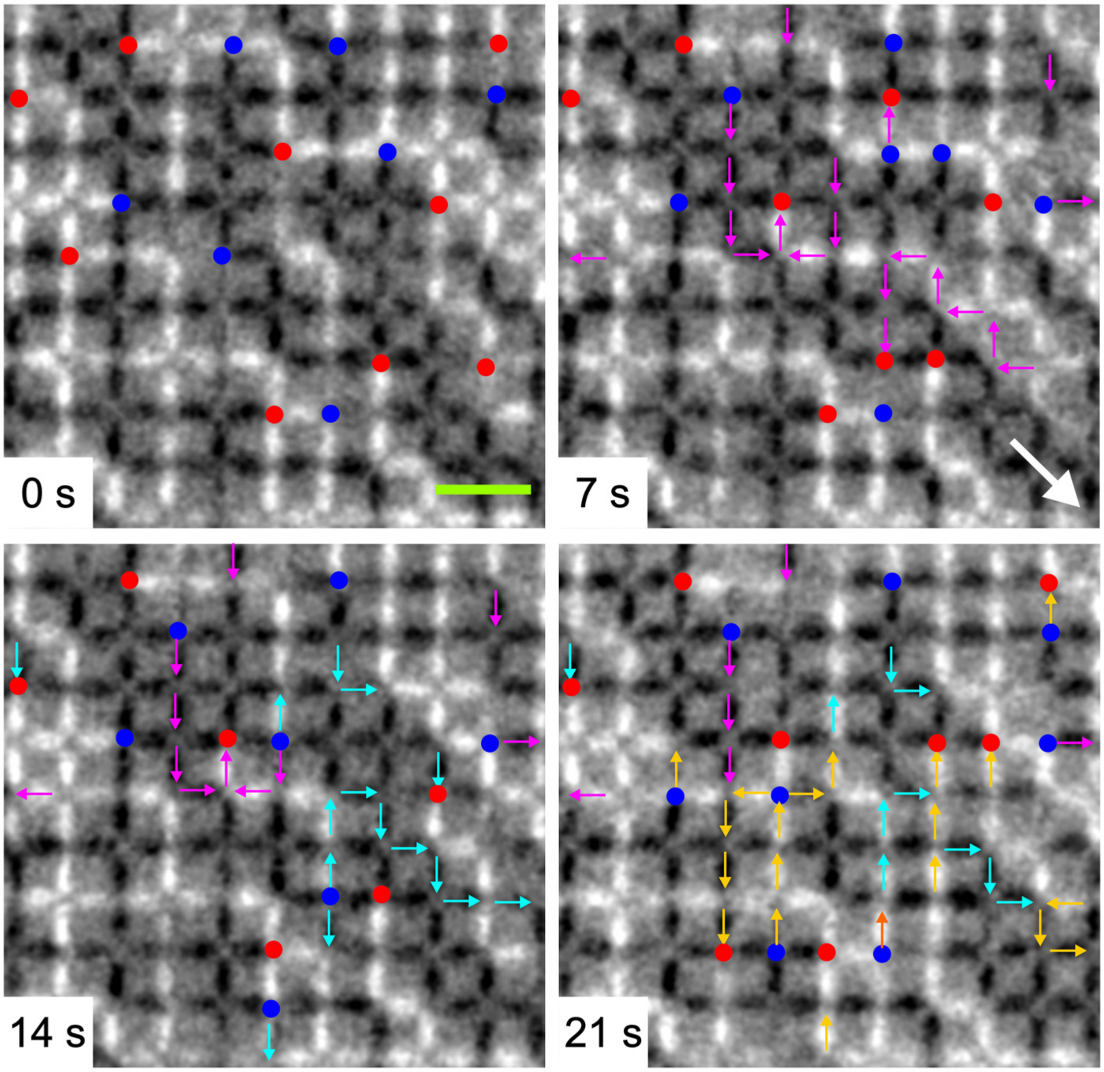

Figure 3.3: Temporal evolution of emergent magnetic monopoles. XMCD image sequence (recorded at T = 190 K) highlighting the thermally driven motion of emergent magnetic monopole defects (blue dots: $Q = -2q$, red dots: $Q = +2q$) in two-dimensional artificial square ice with a height offset h = 145 nm. Arrows of different colors (magenta, cyan blue, and yellow) indicate sequential changes in moment configurations at each instant of time (7, 14, and 21 s). The green bar and the big white arrow indicate a length of 1 μm and the incoming x-ray direction, respectively. Debye-Hückel theory and monopole crystallization

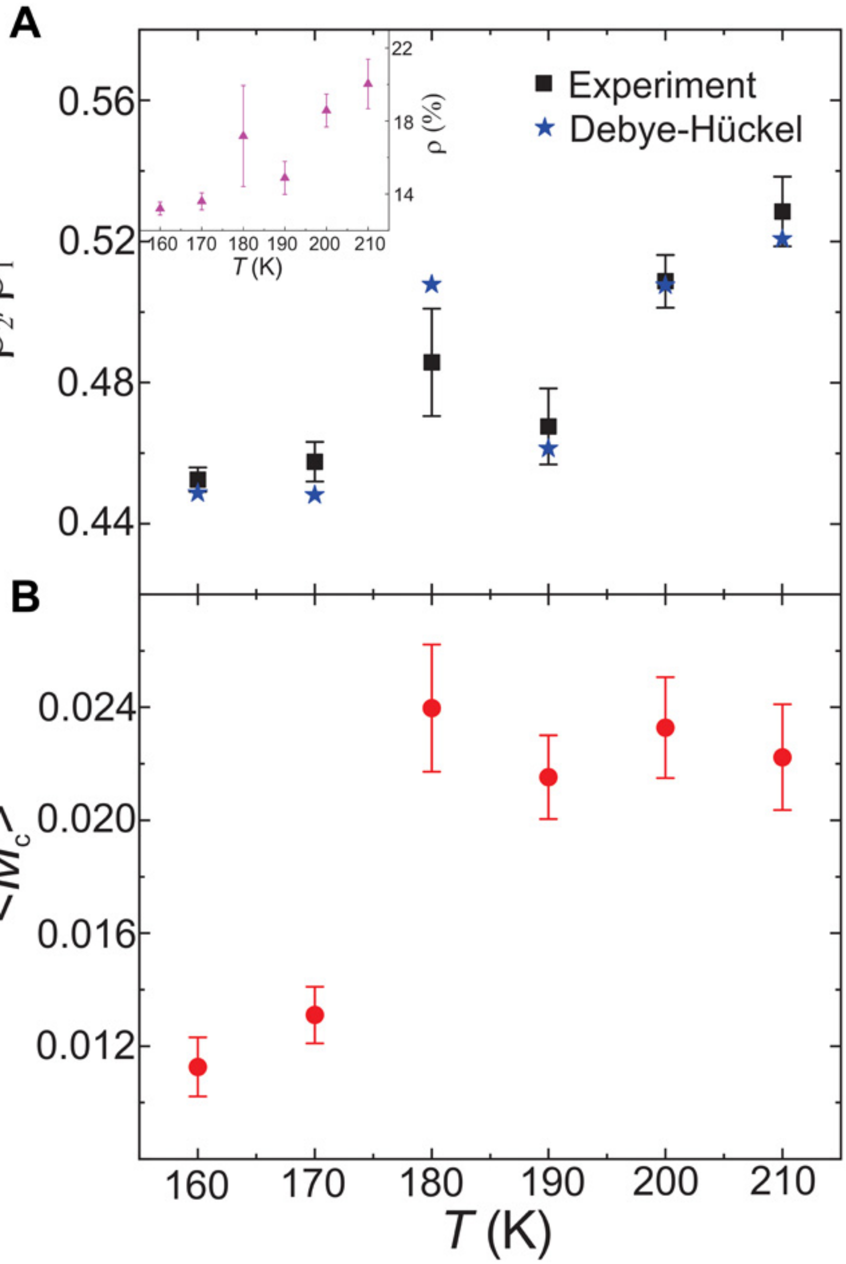

Figure 3.4: Debye-Hückel behavior and crystallization of emergent magnetic monopoles. (a) Ratio of correlated to uncorrelated monopole defects observed in the $h = 145$ nm sample (black dots from Eq. 2.10) compared to the prediction from the Debye-Hückel theory with Bjerrum association corrections (blue stars from Eq. 2.6). The error bars correspond to real-time thermal fluctuations over observations of approximately 15 min at each temperature. The best fit is obtained for a magnetic charge $Q = 9.765 \times 10^{-12}$Am and a magnetization $M = 54$ kA/m in the Debye-Hückel analysis. The overall monopole density ρ as a function of temperature is shown as an inset. (b) Crystallization order parameter over the same temperature range.

Chapter 4

The Trident Lattice: Out of equilibrium relaxation

4.1 Introduction

Though the offset square lattice appropriately restores degeneracy to artificial spin ice, it is not technically simple to achieve. Alternatively, highly frustrated artificial kagome spin ice has been extensively investigated, as it exhibits some analogy to pyrochlore spin ice [99], including a spin liquid phase with short-range correlations [4, 19, 62, 14, 21]. Still, long-range dipolar interactions have been shown to overcome the fixed degree of frustration at low-temperature regimes, leading the system to access a long-range ordered ground state [4, 19, 62]. This raises the question whether a two-dimensional geometrical concept can be proposed that shares some similarities to the square ice geometry, while exhibiting a higher degree of geometrical frustration. In the following, we address this point by exploring moment configurations achieved in a two-dimensional artificial frustrated system consisting of nanomagnets occupying the sites of a so-called trident lattice. Following thermal annealing, we observe how accessible low-energy configurations can be directly manipulated by tuning the balance of competing interactions.

4.2 Results

4.2.1 The dipolar trident lattice

We introduce an artificial frustrated system consisting of three-nanomagnet (trident) building blocks periodically arranged in a perpendicular fashion (Fig. 4.1a). Each nanomagnet is small enough to be single-domain and elongated, so that the magnetization points toward one of two possible directions along the long axis of each nanomagnet, thus representing a single Ising-type moment. As these moments couple via dipolar magnetic fields, we refer to this system as the dipolar trident lattice. Using synchrotron-based photoemission electron microscopy PEEM [25] (section 2.2.2), we directly visualize thermally induced magnetic relaxation of the trident lattice, and demonstrate the inability of the system to access a fully ordered state down to temperatures around 150 K, when tuning the balance of competing interactions. We show how, above 150 K, the ordering preferences of the system can be altered between two long-range ordered phases via an intermediate disordered state, exhibiting a continuous presence of vertex defects, which through their migration control the relaxation process and configurational fluctuations in thermal equilibrium. Upon cooling, the disordered phase also evolves toward long-range order, exhibiting a mixture of the two magnetic configurations.

Energetically, moment configurations in the trident lattice (Fig. 4.1b) can be characterized by four vertex types [105, 30] listed with increasing dipolar energy in Fig. 4.1c. In addition to the vertex types, the so-called trident types need to be taken into account, which are listed with increasing energy as Type A, B, and C in Fig. 4.1c. In order to understand the concept of competing interactions in the trident lattice, one has to be aware of the consequence of dipolar interactions: First, at four-nanomagnet vertices (for example, α, δ, ε, and ν in Fig. 4.1a), nearest neighbors will preferably exhibit a head-to-tail moment alignment, giving rise to Type I vertices (Fig. 4.1c) and vortex-like states (Fig. 4.1d). Second, the tridents (α, β, and γ in Fig. 4.1a) favor an anti-parallel moment alignment (Fig. 4.1d). In a long-range picture, a system where vertex interactions are mostly minimized (Type I vertex domination) cannot satisfy all trident interactions, as Type B tridents will dominate the configuration landscape (Fig. 4.1e). In contrast, if trident interactions are minimized (Type A trident domination), the energetically higher Type II vertices will exhibit a dominating presence (Fig. 4.1f). In other words, it is impossible to simultaneously satisfy both vertex interactions and trident interactions and the system is expected to be frustrated.

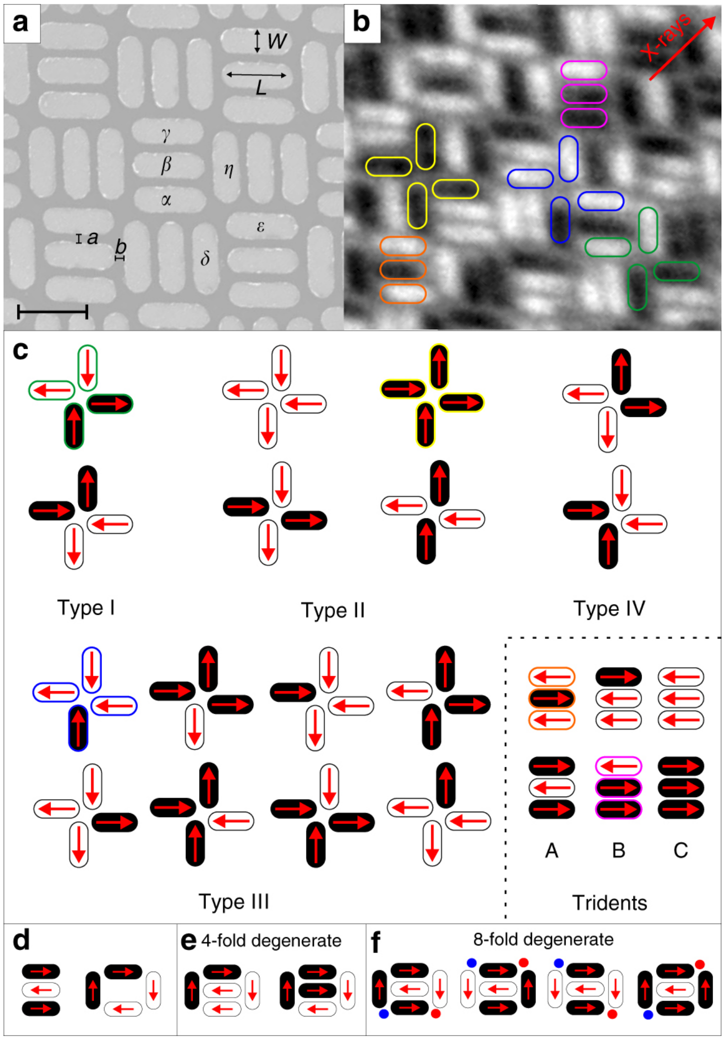

Figure 4.1: The dipolar trident lattice. a Scanning electron microscope image of a dipolar trident lattice (a = b = 50 nm, L = 450 nm, W = 150 nm). The black scale bar indicates a length of 450 nm. b X-ray magnetic circular dichroism (XMCD) image resolving moment configurations achieved in the trident lattice. Nanomagnets with a magnetization pointing toward the incoming X-ray propagation vector (indicated by a red arrow) appear dark, while moments opposing that direction appear bright. c Vertex and trident types listed with increasing energy. In both b, c green, yellow, and blue frames highlight the realizations of Type I, Type II, and Type III vertices, respectively. Regarding tridents, Type A and B tridents are highlighted with orange and magenta frames, respectively. d Minimization of dipolar interactions in an isolated trident building block would result in a Type A domination. On the other hand, nearest-neighbor nanomagnets at the four-nanomagnet vertices will prefer a head-to-tail moment alignment, which would result in clockwise or anti-clockwise vortices. Satisfying vertex interactions (creation of vortices or Type I vertices) results in frustration of trident moments. Satisfying trident interactions (creation of Type A tridents) results in two of nearest-neighbor vertex moments being aligned head-to-head (red circles) or tail-to-tail (blue circles).

4.2.2 Direct observation of thermal relaxation

As a first step, we aim to visualize the consequence of geometrical frustration on the ordering mechanism in a trident lattice consisting of nanomagnets with length, width, and thickness of 450, 150, and 2.7 nm, respectively (section 2.2.1). The lattice spacing was chosen, so that the two relevant parameters a and b (Fig. 4.1a), which control the strength of trident and vertex interactions, respectively, are set to be 50 nm each. The blocking temperature T B, which we define as the temperature at which moment re-orientations start to occur within the timescale needed to acquire a single-PEEM image (7–10 s per image)[30, 34]was determined to be 270 K. The sample was kept at a constant temperature of 280 K and a saturating magnetic field (B = 30 mT) was shortly applied along the incoming X-ray direction. After the field is switched off, the system undergoes thermally induced magnetic relaxation from a well-defined energetically excited state toward a highly disordered equilibrium state (Fig. 4.2a–c).

A quantitative analysis of the relaxation mechanism is obtained by looking at the vertex-type and trident-type populations plotted as a function of time (Fig. 4.2d, e). Starting from a 100% Type II vertex and Type C trident background (saturated state), the system experiences a rapid drop and rise in Type II and Type III vertex populations, respectively, while Type I vertices are moderately on the rise (Fig. 4.2d). In parallel, the population of Type C tridents decreases rapidly, while Type A and B tridents are showing an almost equal increase (Fig. 4.2e). As the system continues to relax, the high number of generated Type III vertex defects converts into Type I vertices, while new defects are continuously generated with an ongoing decrease in Type II vertices. Thus, the system stagnates in terms of Type III population during this stage

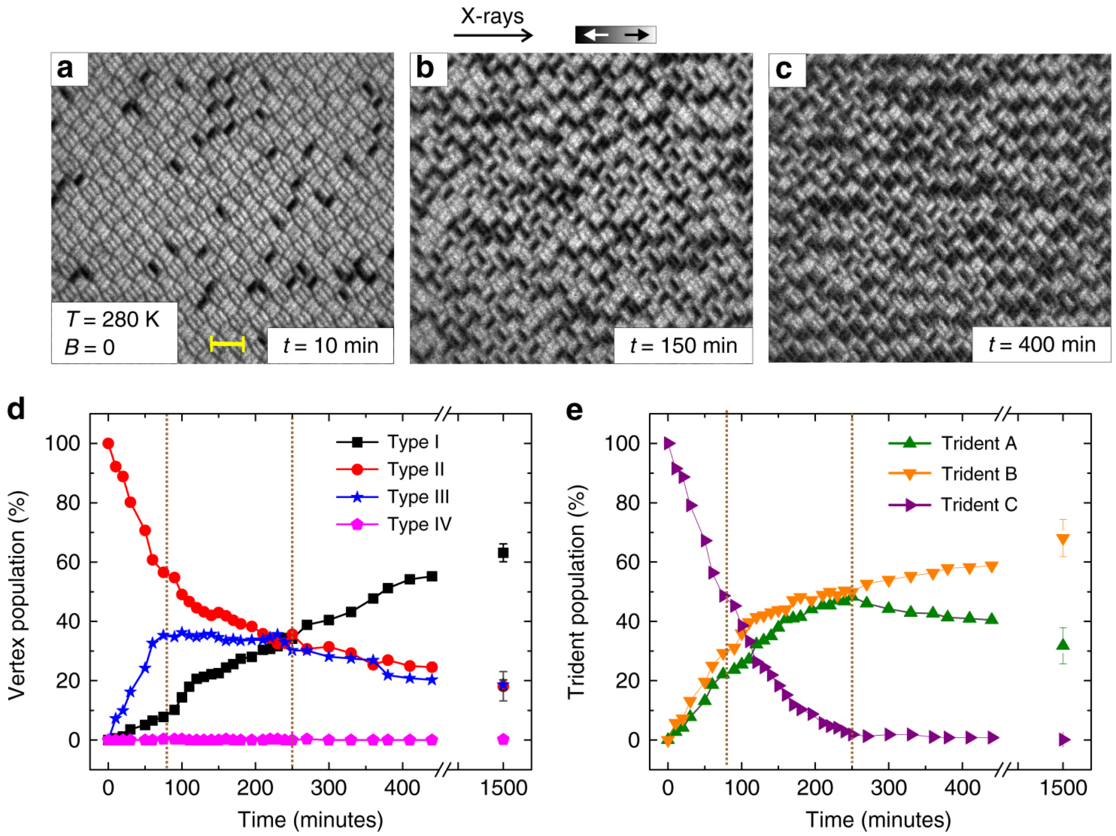

Figure 4.2: Thermal relaxation of the dipolar trident lattice. a–c XMCD images of the dipolar trident lattice undergoing thermally induced magnetic relaxation from a magnetically saturated state to a low-energy equilibrium configuration. The yellow scale bar indicates a length of 1 μm. d Experimentally obtained temporal evolution of vertex-type population extracted from XMCD images recorded at a constant temperature (T = 280 K). e Trident population plotted for the same relaxation process.

(Fig. 4.2d). Finally, the system enters a stage where the Type I vertex population rises continuously at the cost of Type II and Type III vertices, until equilibrium is achieved. Kinetic Monte Carlo simulations (section 2.3.4)[62] are in good agreement with the experimental observations.

4.2.3 Controlling the balance of competing interactions

The dominance of Type I vertices for a = b = 50 nm indicates that the competition between vertex interactions and trident interactions is not perfectly balanced and, as a result, a high degree of frustration is not obtained. This balance of competing interactions can be tuned by varying the b/a ratio. Therefore, a second set of trident arrays are fabricated (section 2.2.1), where a = 50 nm is set to stay constant, while b is varied to be 50, 75, and 100 nm. The sample was kept at a constant temperature of 330 K (T B = 310 K) for 24 h before it was cooled down to 300 K and magnetic images were obtained (Fig. 4.3a–c). Plotting the vertex populations and trident populations as a function of b (Fig. 4.3d, e), we see a transition from a largely ordered phase with Type I vertex and Type B trident domination (b = 50 nm), through a disordered phase with short-range order and no clear preference for any vertex types (b = 75 nm), to, finally, a phase that shows trends toward Type II vertex and Type A trident preference (b = 100 nm).

This balancing act between competing trident interactions and vertex interactions indicates that accessible low-energy states can be directly tuned by a variation of the b/a ratio. This is a direct consequence of the enforced lattice constraints, making it impossible for the involved entities to simultaneously minimize both trident interactions and vertex interactions. Similar to previous work [31, 59], calculating the energy spectrum of an isolated five-nanomagnet building block, clarifies the degeneracies listed in Fig. 4.1e, f. For a system with b/a = 1, the building block ground state is four-fold degenerate, with a clear gap to the second energy band, which consists of eight quasi-degenerate states. This gap can be tuned by varying the b/a ratio. The critical ratio b/a = 1.5 of the relevant lattice parameters can be further comprehended, when comparing the dipolar energies for fully ordered magnetic configurations of Type A/Type II and Type B/Type I trident types and vertex types as a function of b, while a is kept constant at 50 nm. Dipolar energies are equalized when b reaches a value around 75 nm. In other words, this is the point where the dipolar trident lattice reaches maximum degeneracy with no preference for any of the twelve states listed in Fig. 4.2e, f.

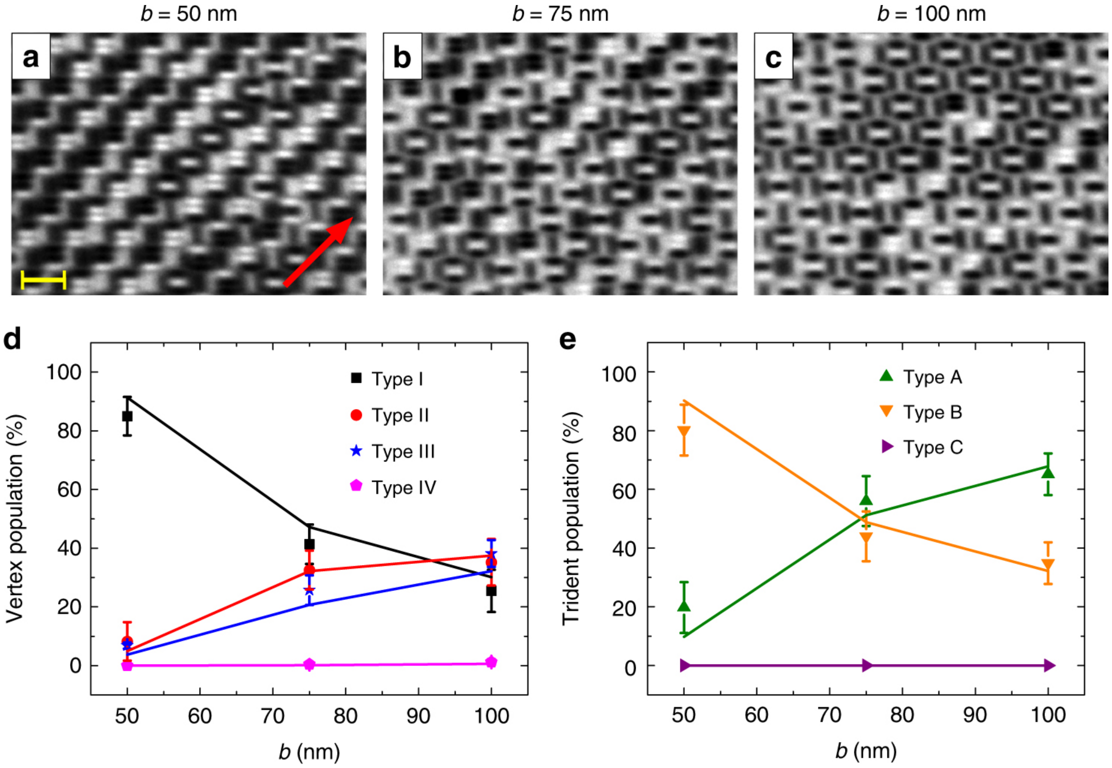

Figure 4.3: Tuning geometrical frustration in dipolar trident lattice. a–c XMCD images of equilibrium configurations of trident lattices with various lattice spacings (a = 50 nm = constant, b = 50, 75, and 100 nm) recorded at T = 300 K (blocking temperature T B = 310 K). The red arrow indicates the direction the X-ray propagation vector. The yellow scale bar indicates a length of 1 μm. d Experimentally observed vertex-type population plotted as a function of lattice parameter b. e Trident-type population plotted with increasing lattice parameter b. Experimental observations (filled symbols) are in satisfactory agreement with equilibrium Monte Carlo simulations (lines). The results reveal the transition from a Type I vertex and Type B trident-ordered state (b = 50 nm), to a disordered configuration (b = 75 nm) with no clear ordering preference, and, finally, to a Type A trident-ordered state (b = 100 nm), as the lattice parameter b is increased. The error bars represent standard deviations originating from ten experimental observations.

4.2.4 Low-temperature configurations and magnetic structure factors

As a next step, we study how the degeneracy of low-energy building block states affects moment configurations at lower temperatures. Previous work on highly frustrated artificial kagome spin ice [4, 31, 92] showed that despite an extensive degeneracy and short-range ordering at higher temperatures, the long-range nature of dipolar interactions gives rise to ordered configurations at lower temperatures. Therefore, it is our purpose here to see whether any signatures of long-range ordering can be observed in the dipolar trident lattice, particularly in the case of highest degeneracy, when b/a = 1.5.

We prepared another set of trident lattices, consisting of nanomagents with lengths L = 300 nm, widths W = 100 nm, and thickness d = 2.4 nm, together with the corresponding lattice parameters a = 33 nm = constant and b = 33, 50, and 66 nm. This reduction of nanomagnet size resulted in a lowering of the blocking temperature down to 160 K. The sample was kept in vacuum at room temperature for 20 days, before it was cooled down to 150 K for XMCD image acquisition (Fig. 4.4a–c). While long-range ordered patterns are observed for b = 33 and 66 nm, the b = 50 nm array remains disordered at 150 K. Similar to the room-temperature data (Fig. 4.3), tuning of geometrical frustration can again be inferred from the evolution of vertex populations and trident populations as a function of lattice parameter b. Our results thus indicate that for the case b/a = 1.5, the system is caught in a short-range ordered phase, while both the b/a = 1 and 2 cases exhibit long-range ordered ground state configurations.

A deeper quantitative insight into the experimentally accessed low-temperature configurations is achieved by calculating the respective magnetic structure factors [75](section

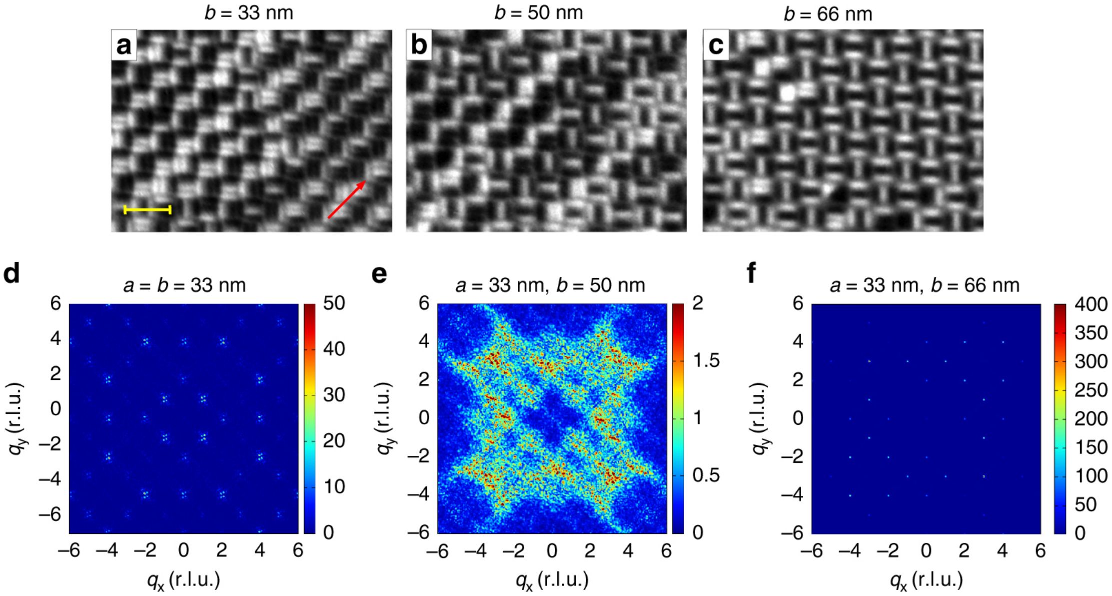

Figure 4.4: Experimental low-temperature observations. a–c XMCD images of equilibrium configurations of the dipolar trident lattice with various lattice spacings (a = 33 nm = constant, b = 33, 50, and 66 nm) recorded at T = 150 K (blocking temperature T B = 160 K). The red arrow indicates the direction the X-ray propagation vector. The yellow scale bar indicates a length of 600 nm. d–f Magnetic scattering patterns of moment configurations achieved in dipolar trident lattices with lattice parameters d a = 33 nm and b = 33 nm, e a = 33 nm and b = 50 nm, and f a = 33 nm and b = 66 nm, following thermal annealing. While long-range order with relatively sharp peaks is seen for b = 33 nm and b = 66 nm, the diffuse patterns for b = 50 nm indicate highly disordered moment configurations with short-range correlations.

2.3.1), which are shown in Fig. 4.4d–f. For both b = 33 nm and b = 66 nm (Fig. 4.4d, f), we see relatively sharp peaks in the magnetic structure factors. The splitting of the magnetic peaks into four satellites for b = 33 nm reflects multi-domain long-range ground state ordering for b = 33 nm (Fig. 4.4d). Figure 4.4f (b = 66 nm) shows sharp magnetic peaks that stand for an almost single-domain long-range ordered ground state consisting mostly of a tile of two Type A tridents, as can also be seen from real-space images (Fig. 4.4c). However, a dramatic change in the magnetic structure factor is observed for the lattice parameter combination of a = 33 nm and b = 50 nm (Fig. 4.4e), where the diffuse patterns indicate the presence of a disordered phase consisting of a complex arrangements of possible low-energy configurations (Fig. 4.1e, f), where neither of these states dominate. Similar patterns are also observed in the structure factor of the simulated b = 50 nm system. To ensure that these simulated configurations are in fact in thermal equilibrium, we use the parallel tempering technique [27, 98, 108](section 2.3.4), where the equilibration time is estimated by calculating the so-called exponential autocorrelation time [108], τ exp, which itself is defined by the temporal decay of the autocorrelation function, $\Gamma \propto \exp[-t/\tau]$ (section 2.3.5). The agreement between experimental and simulated configurations provides evidence that the experimental observations also represent states in thermal equilibrium.

4.3 Discussion

In summary, we presented a magnetically frustrated meta-material, which provides the possibility to directly control competing dipolar interactions at the nanoscale, thus allowing versatile tuning of geometrical frustration and ground state configurations. The complex phase into which the system gets trapped, when competing interactions are balanced, opens up multiple questions regarding the physics of the dipolar trident lattice, in particular the question regarding possible phase transitions toward complex long-range ordered states at lower temperature regimes [4, 19, 62]. Experimentally, this will require the fabrication of trident lattices consisting of nanomagnets with lateral dimensions that go beyond the spatial resolution of known magnetic imaging techniques [4], and will therefore rely on emerging scattering and spectroscopic techniques [4, 92, 64, 76].

Chapter 5

The Cairo Lattice: Topological frustration and polarons

5.1 Introduction

Artificial spin ice candidates need not comprise a single vertex geometry (coordination number three for the kagome lattice, coordination number four for the square lattice). Many systems with mixed coordination numbers [38, 34, 18], while exhibiting high degeneracy levels, have been shown to exhibit long-range charge-ordered states at lower temperatures. This raises the question whether another system with mixed coordination numbers can be proposed, which exhibits a high degree of spin frustration and remains in a state that is dominated by short-range spin correlations, thus adding an additional system to the family of artificial frustrated systems [70].

In this paper we address this question, by exploring geometrical frustration achieved

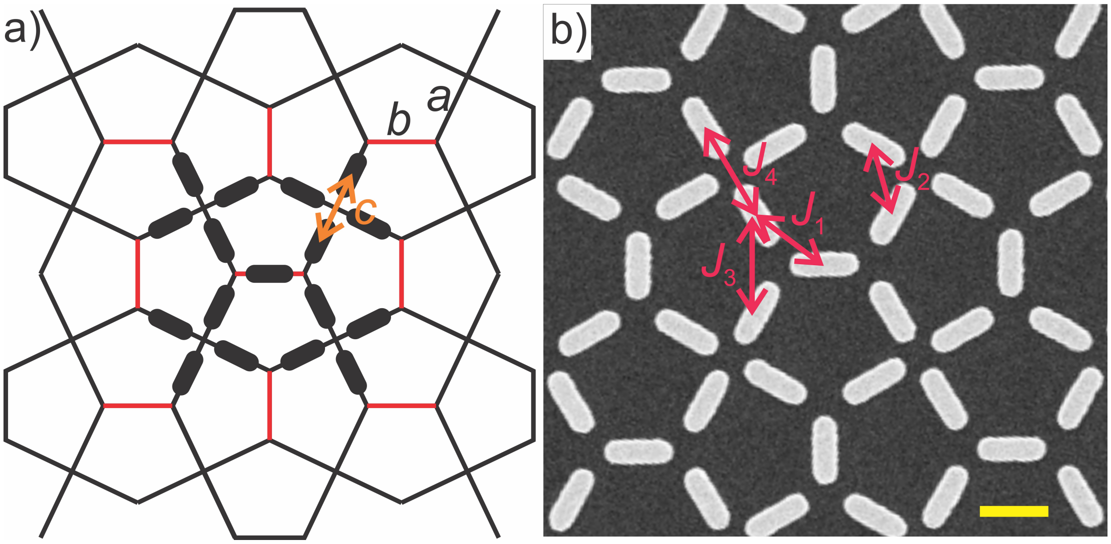

Figure 5.1: (a) Dipolar Cairo lattice. We see dipolar-coupled Ising-type nanomagnets (stadium-shaped islands) occupy the sites of the pentagonal Cairo lattice (lines the background). Lattice parameters $a = 472$ nm and $b = 344$ nm are kept constant, while the lattice parameter $c = 376$ nm, 450 nm, 500 nm and 600 nm is varied, to tune the coupling strengths between the nanomagnets. (b) Scanning electron microscopy (SEM) image of one of the dipolar Cairo lattices consisting of nanomagnets with lengths and widths of 300 nm and 100 nm, respectively. The coupling parameter c can be varied, so that the balance between the coupling strengths J_1, J_2, J_3 and J_4 can be tuned at the nanoscale. The yellow scale bar indicates a length of 300 nm.

in a two-dimensional artificial spin system, where Ising-type nanomagnets are placed onto the sites of a so-called Cairo lattice (see Fig. 5.1). The Cairo lattice geometry has risen to prominence as an alternative approach in achieving geometrical spin frustration leading to a variety of new properties and ground state configurations [88, 86, 102, 86].

This chapter is organized as follows: in the methods section, we describe the process of sample fabrication and the magnetic imaging technique. Micromagnetic simulations of relevant coupling strengths are also described. This is followed by a report on thermal annealing and magnetic imaging experiments including a quantitative analysis of all observations. The data obtained are discussed in terms of short-range spin correlations, highlighting the high degree of geometrical spin frustration achieved in this artificial spin system. We conclude with a summary and outlook on potential future investigations featuring the dipolar Cairo lattice.

5.2 Methods

We used electron beam lithography to fabricate dipolar Cairo lattices. The resulting patterned nanomagnets have a length of 300 nm and a width of 100 nm and they are arranged onto a Cairo lattice with lattice parameters a = 472 nm and b = 344 nm (see Fig. 5.1a). The coupling strengths J_i (see Fig. 5.1b) are directly tuned by varying the lattice parameter c (see Fig. 5.1a), which is given values of 376 nm, 450 nm, 500 nm and 600 nm. Each array covered an area of $60 \times 60\ \mu\mathrm{m}^2$.

Magnetic imaging was performed by synchrotron-based photoemission electron microscopy (PEEM) [25], employing x-ray magnetic circular dichroism (XMCD) at the Fe L_3 edge [97]. XMCD images were obtained by pixel-wise division of images recorded with circular right and left polarized light. The resulting dark and bright contrast provides a direct measure of the orientation of the local magnetization. Magnetic moments pointing towards the incoming X-rays will appear dark and moments opposing the X-ray direction will appear bright. If a magnetic moment is oriented 90° with respect to the X-ray direction, it does not show contrast and appears gray. Because the nanomagnets of the dipolar Cairo lattice are patterned along different directions, deterministic imaging of all magnetic moments is challenging (see Fig. 5.1b). To ensure that all magnetic moments have a non-zero projection onto the incoming X-rays, we rotated the sample by 15°.

We performed micromagnetic simulations using MuMax3 [103] to determine the coupling energies in the dipolar Cairo geometry. In the simulations, nanomagnets with a size of $300 \times 100 \times 3$ nm^3 were discretized into $1.95 \times 1.95 \times 3$ nm^3 cells. Typical material parameters for Permalloy were used: $M_\mathrm{s} = 790$ kA/m, $A = 13 \times 10^{-12}$ J/m. The magnetic anisotropy was set to zero. As the Gilbert damping parameter we used $\alpha = 1.0$ to allow the simulations to relax quickly. The coupling energies were derived from simulating different nearest-neighbor nanomagnet pairs. To do this, we first determined the low and high energy states E_1 and E_2, which are given by $E_1 = 2E_\mathrm{nanomagnet} - E_\mathrm{coupling}$ and $E_2 = 2E_\mathrm{nanomagnet} + E_\mathrm{coupling}$. Here, only the coupling energy E_coupling depends on the orientation and distance between the nanomagnets. The coupling energy is then given by $E_\mathrm{coupling} = (E_2 - E_1)/2$. The simulations were performed for a lattice parameter c varying from 350 nm to 600 nm in 12.5 nm steps.

5.3 Results

5.3.1 Energy landscape and micromagnetic simulations of coupling strengths

Before we summarize the experimental observations, it is important to understand and characterize the dipolar Cairo lattice energetically. As in other artificial spin ice systems [105, 38, 34, 29, 77], the magnetic configurations can be categorized into vertex types (see Fig. 5.2). The dipolar Cairo lattice exhibits four- and three-nanomagnet vertices similar to those observed in the square- and kagome spin ice geometry, respectively [105, 30]. The four-nanomagnet vertex types are listed with increasing dipolar energy in Fig. 5.2a, going from Type I to Type IV. Type I and Type II obey the so-called ice rules, which dictate two moments to point into the vertex and two moments to point out of the vertex (see Fig. 5.2a). In an emergent magnetic charge picture [75, 33, 16, 62], these vertices exhibit a zero magnetic charge at the vertex of $Q = 0$. Type III vertices break the ice rule, as three moments point into the vertex and one out or vice versa. In the magnetic charge representation, they can be seen as topological defects bearing a non-zero effective magnetic charge residing at the vertex ($Q = \pm 2q$). Type IV vertices (($Q = \pm 4q$) represent the highest energy states and are energetically so unfavorable that they are not observed in our experiments. The three-nanomagnet vertices can be compared to the known kagome vertices [30, 29, 80], however, with one crucial difference:

Because $a \neq b$ and the varying lattice parameter c, the distances between nanomagnets at the three-nanomagnet vertices can be non-equal, resulting in different coupling strengths ($J_1 \geq J_3$). Therefore, the six-fold degenerate ice-rule (two-moments-in-one-moment-out or vice versa) configurations are now split into two different vertex types. Moment alignments that minimize the stronger J_1 interactions (coupling between black and red moments in Fig. 5.2b) are lower in energy and are labeled Type A (see Fig. 5.2b). Configurations that minimize the weaker interaction J_3, but maximize one of the two J_1 interactions, are higher in energy and are labeled Type B vertices. Configurations breaking the ice-rule remain energetically equivalent and are now branded Type C.

The unique feature in the dipolar Cairo lattice is that the balance between the competing interactions J_1 and J_3 can be tuned at the nanoscale from being vastly different to being totally equal. In the latter case, Type A and Type B vertices become energetically equivalent again. In other words, one can turn the spin ice degeneracy at the three-nanomagnet vertices on and off, by varying the lattice parameter c. In Fig. 5.3 we plot all coupling strengths J_1 to J_4 as

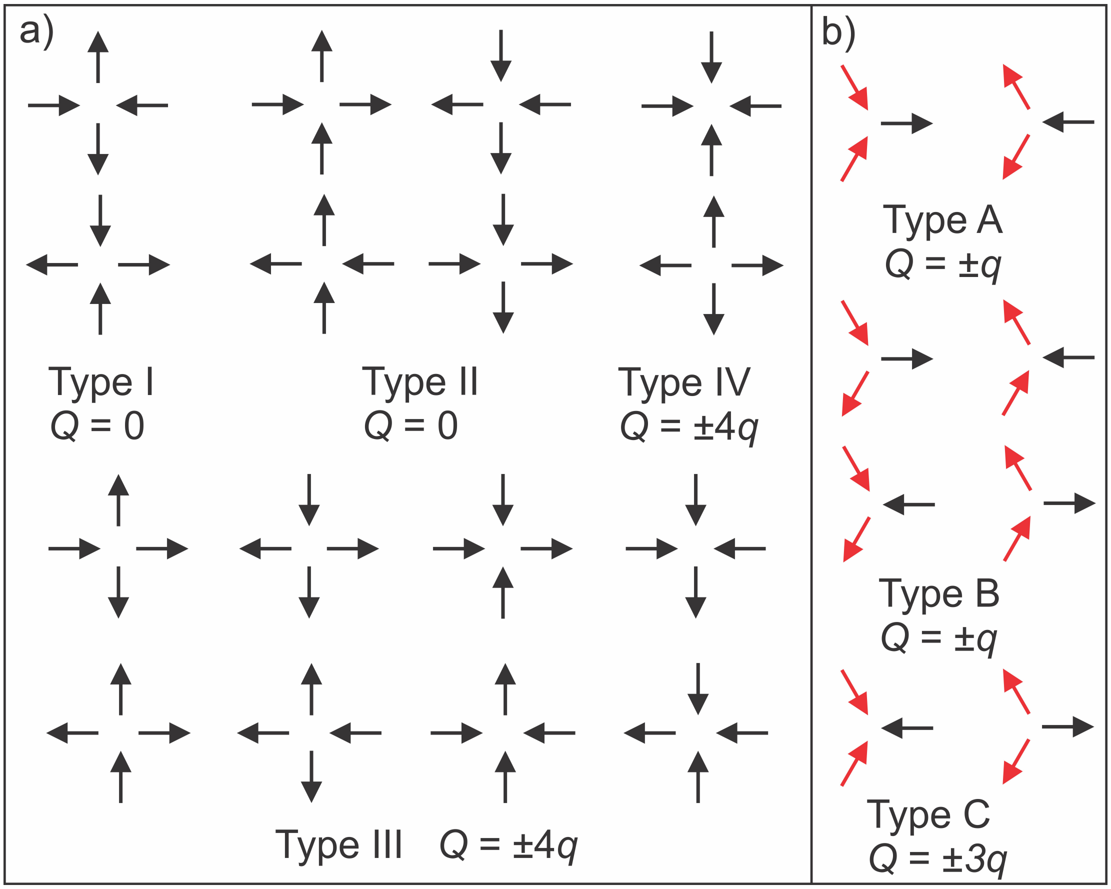

Figure 5.2: (a) Vertex types at four-nanomagnet vertices listed with increasing dipolar energy from Type I to Type IV. Type I and Type II are the so-called ice-rule obeying configurations and exhibit a zero net emergent magnetic charge at the vertex ($Q = 0$). Type III vertices break the ice rules and can be described as vertex defects that possess an non-zero net magnetic charge at the vertex ($Q = \pm 2q$). Type IV vertices have the highest energy and are never observed in our experiments. (b) Vertex types at three-nanomagnet vertices categorized with increasing dipolar energy from Type A to Type C. Red arrows mark those moments that are coupled with each other via J_3, while the red and black arrows are coupled via J_1.

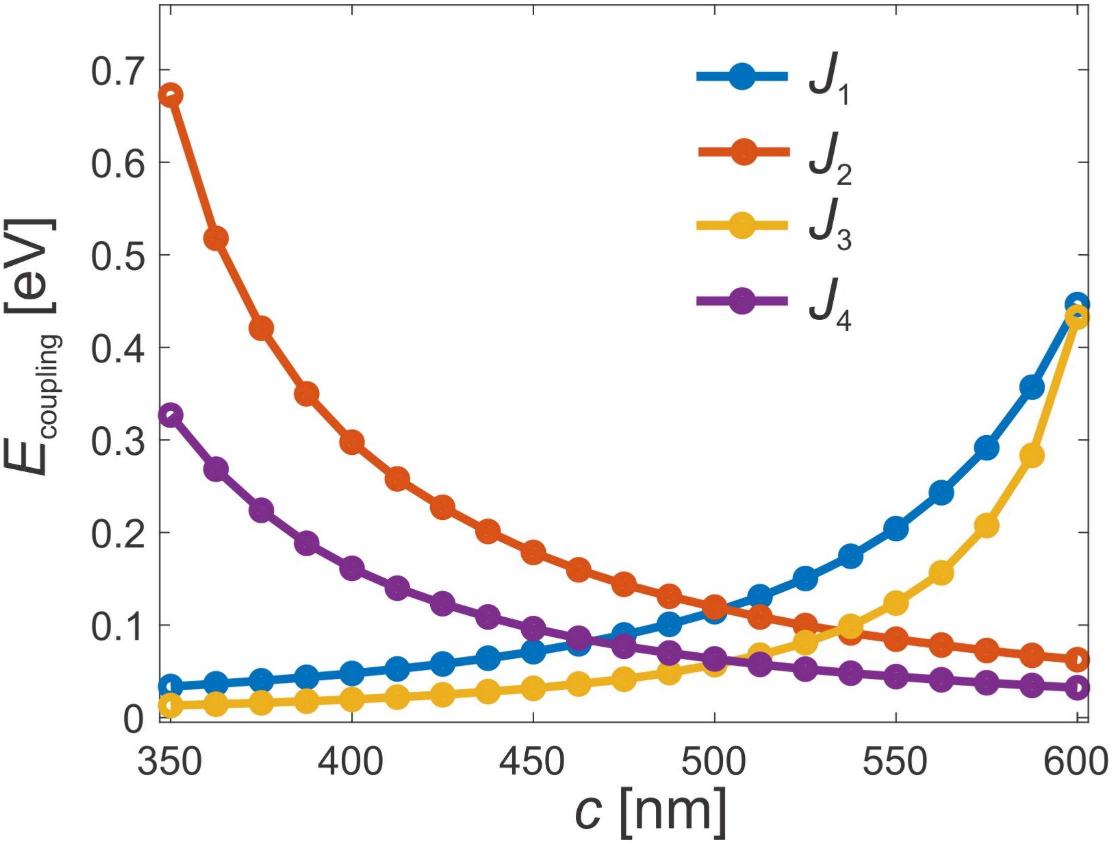

Figure 5.3: Evolution of all relevant coupling strengths J_1 (blue dots and curve), J_2 (red dots and curve), J_3 (yellow dots and curve) and J_4 (purple dots and curve) plotted as a function of coupling parameter c.

a function of c (see Methods). According to these simulation results, J_1 and J_2 as well as J_3 and J_4 equalize around $c = 500$ nm. Equalization of J_1 and J_3 and thus a restoration of the spin ice degeneracy (Type A Energy = Type B Energy) is predicted around coupling parameter $c = 600$ nm (blue and yellow curves in Fig. 5.3). This can also be seen when looking at micromagnetic vertex type energy calculations (see Fig. 4d and e).

5.3.2 Thermal annealing and XMCD imaging

Now that the dipolar Cairo lattice has been introduced, we turn our attention to thermal annealing experiments. Similar to previous work on artificial frustrated systems [28, 30, 34, 32, 33], the prepared structures were kept at room temperature and in vacuum for several days. Then, the samples were transferred into the PEEM and cooled down 20-30 K below the temperature where thermally-induced moment fluctuations start to occur within the nanomagnets on the time scale of several seconds [34, 32, 33]. Cooling below the so-called blocking temperature (T_B = 130 K in our system) ensures that configurations remain frozen during XMCD imaging after thermal annealing. For each lattice parameter (c = 376 nm, 450 nm, 500 nm and 600 nm), this annealing procedure is performed five times of each to ensure sufficient statistics. To ensure that observations are not linked to lithographic defects, a different array on the sample was imaged, after each annealing protocol.

Figure 4 shows XMCD images of dipolar Cairo lattices. For all values of the lattice parameter c, long-range ordering is absent by pure visual inspection. A first quantitative characterization of these observations is obtained by plotting the vertex type populations achieved as a function of lattice parameter c (see Fig. 4d and 4e). The four-nanomagnet vertices show a nearly linear decrease in the Type I ground state population, while Type II vertices are rising with increasing lattice parameter c. Type III vertex defects are almost absent up to c = 450 nm, but appear in lattices with c = 500 nm and c = 600 nm. The diminishing energy difference between all four-nanomagnet vertices (see dashed curves in Fig. 4d) is likely what allows these ice rule violations to occur. In contrast to the four-nanomagnet vertices, the populations of three-nanomagnet vertex Types do not depend much on c (see Fig. 4e). Intuitively, one would expect, that full dominance by ground state Type I vertices would lead to the ergodicity of Type A and Type B three-nanomagnet vertices, comprising 1/3 and 2/3 of the population, respectively. However, the number of Type A and Type B vertices is approximately equal, implying that another mechanism is at play. Curiously, only the 600 nm system moves towards ergodicity as the Type A and B vertices equalize in energy (see dashed curves in Fig. 4e) and ice rule obedience at the four-nanomagnet vertices diminishes. In summary, the dipolar Cairo lattice aims to establish a Type I ground state configuration at the four-island vertex sites, while the three-island vertices strictly obey the ice rule (almost no Type C vertices). However, the proportion of Type A vertices remains higher than expected. These observations provide a first glance as to why the dipolar Cairo lattice lacks features of long-range order, standing in contrast to other dipolar systems with mixed coordination numbers [34, 18].

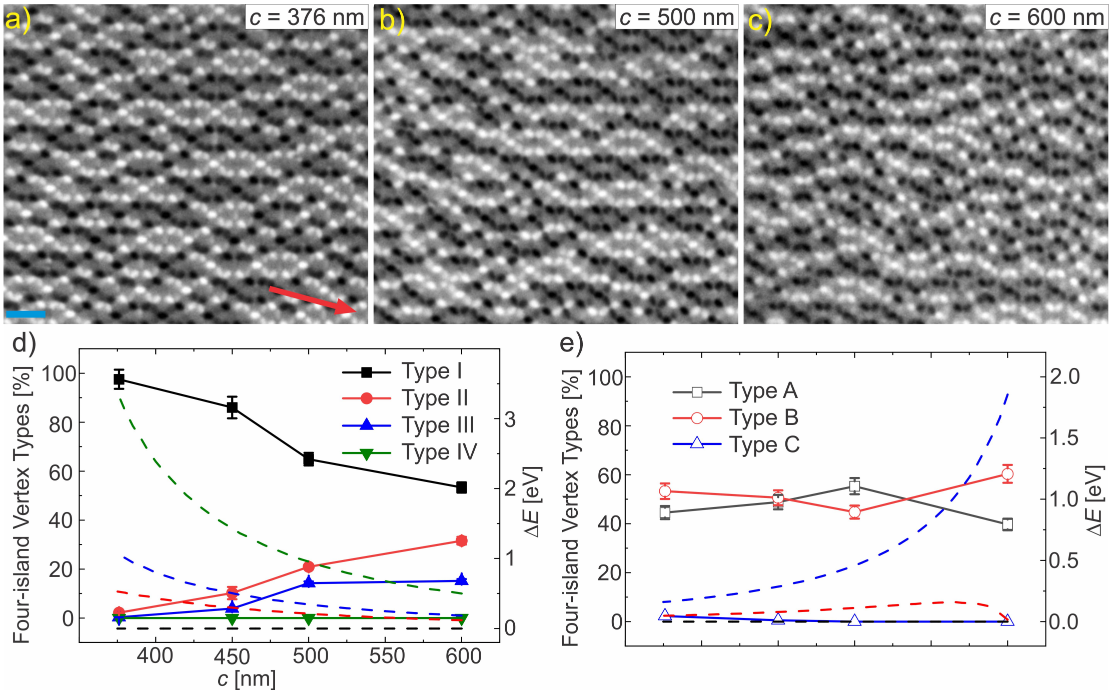

Figure 5.4: XMCD images (recorded at T = 100 K) of a low-energy moment configuration achieved, following thermal annealing in (a) dipolar Cairo lattice with lattice parameter c = 376 nm, (b) c = 500 nm and (c) c = 600 nm. The incoming X-ray direction is indicated by a large red arrow. The XMCD dark-and-bright contrast gives a direct measure of the magnetization direction relative to the incoming X-ray propagation vector. Magnetic moments pointing towards the incoming X-rays appear dark, while moments opposing the X-ray direction appear bright. The blue bar indicates a length of 1 μm. (d) Vertex type populations at four-nanomagnet vertices plotted as a function of lattice parameter c. (e) Three-island vertex-type population under the variation of c. The error bars in (d) and (e) represent standard deviations of the mean resulting from XMCD measurements performed after each of the five repeated annealing cycles. The dashed curves in (d) and (e) represent the corresponding relative vertex type energies (from micromagnetic calculations) plotted as a function of c.

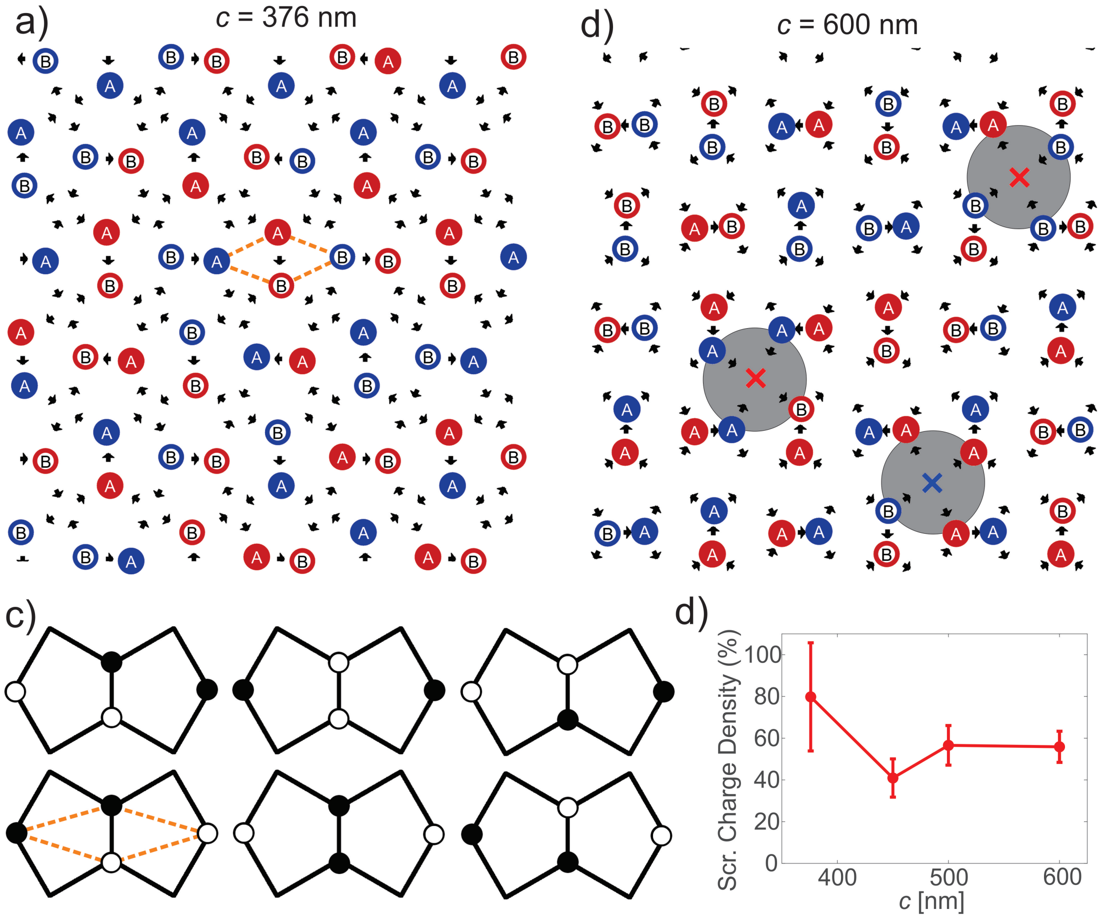

Figure 5.5: (a),(b) Magnetic moment and charge configurations achieved after thermal annealing for Cairo lattices with (a) c = 376 nm and (b) c = 600 nm. Positive $+q$ and negative $-q$ charges are depicted in with red and blue circles at three-nanomagnet vertices, respectively. Filled circles represent Type A vertices, while Type B vertices are shown with empty circles. Type III charge defects $\pm 2q$ are represented with red (+) and blue (-) crosses. Grey circles in (b) highlight screened charge defects. (c) Four-vertex plaquettes obeying the emergent ice-rule. Six variations of the two Type A (filled circles) and two Type B (empty circles) vertices within each plaquette obey this emergent ice-rule. (d) Percentage of screened Type III charge defects plotted as a function of lattice parameter c. The error bars represent standard deviations resulting from observations after each one of the five annealing cycles.

5.3.3 Emergent ice-rule and polaronic states

The Cairo lattice is topologically equivalent to the recently investigated Shakti lattice [38, 72]. implying that the same mode of toplogical frustration prevents long range order in the system. Looking at magnetic moment configurations (see arrows in Fig. 5.5a and b) and magnetic charge patterns (blue and red circles in Fig. 5.5a and b), long-range order seems absent. In analogy to the Shakti lattice, the Cairo lattice largely obeys an emergent ice-rule. This rule dictates that a system with this geometry and only Type A, B, and I vertices must distribute Type A and Type B vertices (filled and empty circles in Fig. 5.5a, b and c, respectively) equally within a four-vertex plaquettes (see Fig. 5.5c). The emergent ice rule explains the discrepancy from ergodic vertex populations by bringing them closer to 50% (see Fig. 5.4e). This strict emergent ice-rule obedience is particularly striking in the case of strong nearest-neighbor coupling at the four-nanomagnet vertices (c = 376 nm) due to the lack of Type II-IV vertices and provides a direct explanation why the Cairo lattice lacks features of long-range order. As the lattice parameter c is increased, we see an increasing number of violations to this emergent ice-rule (see Fig. 5.5b) because coupling strengths of the coordination number four vertices (J_2 and J_4) no longer dominate. Interestingly, this is coupled to an increase in Type III vertex defects at the four-nanomagnet vertex sites (blue and red crosses in Fig. 5.5b). These vertex defects can be seen as emergent magnetic charge defects ($Q_{z4} = \pm 2q$), with a major part of them getting screened by surrounding magnetic charges ($Q_{z3} = \pm q$), which reside at neighboring three-nanomagnet vertices (see Fig. 5.5d). In other words, the sum of magnetic charges residing at four- and three-nanomagnet vertices becomes zero ($\sum Q_{z4} + Q_{z3}$ = 0). The fraction

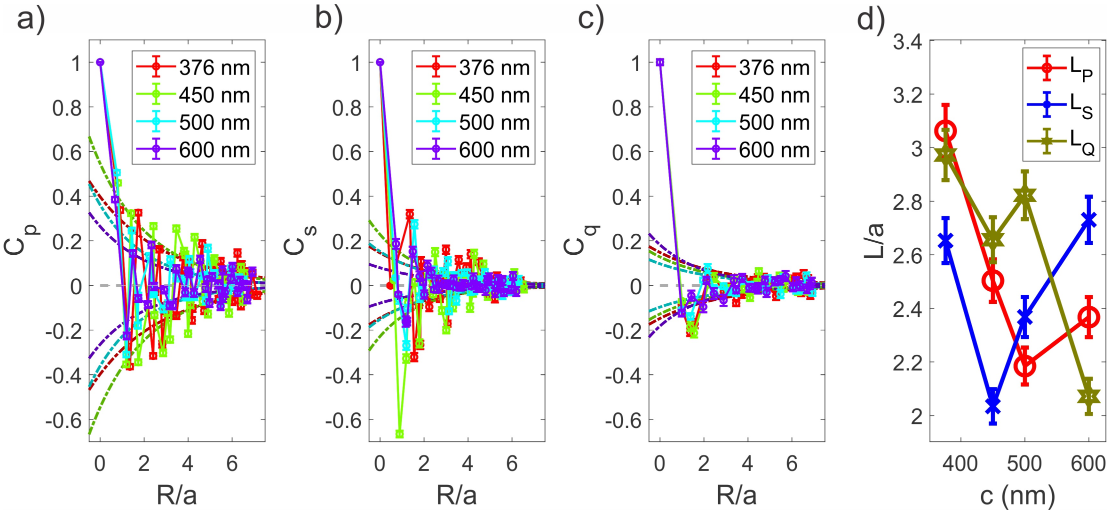

Figure 5.6: Correlation functions and extracted correlation lengths of all annealed ground states. All length scales are stated in proportion to the lattice parameter $a = 472$ nm. (a),(b) Spin-spin correlations between the ”p” subset of spins (a) and the ”s” subset of spins (b). (c) Charge-charge correlation function of all charges in the lattice. All correlation function seem to be exponentially encapsulated as a function of distance. (d) Correlation lengths as a function of lattice parameter c. The error bars represent standard deviations resulting from XMCD measurements performed after each of the five repeated annealing cycles.

of Type III vertices that are perfectly screened is plotted in Fig. 5.5d. A random distribution of Q_{z3} charges would only screen four out of sixteen possible states, but all fractions remain significantly higher than 25%. The outlying point at $c = 376$ nm is likely a result of the low number of Type III vertices (9) at this offset. These polaronic states are a typical feature for structures with mixed coordination numbers as predicted and observed in the dipolar dice and pentagonal lattice [34, 18]. However, in contrast to these cases, which feature long-range charge ordered ground states, the dipolar Cairo lattice does not seem to show any tendency towards long-range ordering, whether defined by magnetic charges or magnetic moments.

5.3.4 Correlations and short-range ordering

The existence of preferred vertex types and emergent ice rule obedience suggests quantifiable short-range ordering within the system. Additionally, the emergent magnetic charges may possess some hidden order [20], providing another structure to the system not immediately apparent in the magnetic orientation of the islands. Here we extract the spin-spin and charge-charge correlation functions, fit these functions to an exponential, and from those fits compute the spin and charge correlation lengths.

The geometry of the Cairo lattice creates two subsets of spins, those only partaking in three island vertices and those in both three and four island vertices. The former we label ”p” spins because they are parallel and perpendicular to each other and the latter we label ”s” spins as they are skewed from one another. The two subsets experience different types of interactions and therefore should not be assumed to have correlation functions that behave the same. The correlation functions themselves are calculated in a manner typical of Ising type systems:

$$C(\mathbf{r}_{ij}) = S_i S_j \tag{5.1}$$

where $S_i = \pm 1$ to represent the Ising state of spin i and r_{ij} is the distance between spins i and j. There is normally a thermal average, but it is omitted here as the analysis is performed on single configurations. The correlation functions are made a function of distance, r, by averaging over C_{ij} where $r - \Delta/2 < r_{ij} < r + \Delta/2$:

$$[C(r)]_{av} = \frac{1}{N_{pair}} \sum_{ij}' C(\mathbf{r}_{ij}). \tag{5.2}$$

Here, N_{pair} is the number of pairs of ij over which the sum is taken. A charge correlation function is defined similarly as

$$C_{Q,ij} = \Theta(Q_iQ_j), \tag{5.3}$$

where Q_i is the magnetic charge at a vertex labeled i and $\Theta(x)$ returns the sign of the argument or zero if the argument is zero. Again, the function is averaged over similar distances to create $C(r)$. The magnitude of this parameter and the spin correlations are fitted to an exponential decay function, $|C(r)| = A\exp(-r/L)$, where A is merely a fitting constant and L is the correlation length (see dashed curves in Fig. 5.6a-c). Three categories of lengths are extracted for the p spins, s spins, and charges (L_p, L_s, and L_Q respectively). The correlation lengths are plotted as a function of c in Fig. 5.6d.

All correlation functions (Fig. 5.6a-c) are fit to exponentials with confidence intervals of 95%. They typically oscillate between positive and negative values as antiferromagnetic spin ordering and alternating charge ordering are preferred. The higher value of the spin correlation functions (Fig. 5.6a-b) compared to the charge-charge correlation function (Fig. 5.6c) indicates a dominant preference for spin ordering over charge ordering. Though they are less likely to correlate, the lengths over which charges correlate are similar to the spin correlation lengths (Fig. 5.6d). In accord with the topological frustration picture, the spin-spin correlation lengths are all on the order of 2-3 lattice parameters a, approximately the size of a single plaquette. Long-range order is clearly absent, consistent with the vertex and pattern frustration. Despite the absence of a clear trend, the ”p”- and ”q” lengths roughly decrease with increasing c and the ”s” length fluctuates up and down with c. Each of the three correlation lengths are dominant for at least one value of c. These non-monotonic behaviors further highlight the flexibility in defining ordering preferences in the dipolar Cairo lattice.

5.4 Discussion

The Cairo lattice presents rich, tunable frustration. Its geometry allows for lattice parameter c to influence 4 magnetic coupling constants (Fig. 5.3). All annealed systems with c varying from 376 nm to 600 nm contained no apparent long-range order (Fig. 5.4) as verified by correlation function and correlation length calculations (Fig. 5.6). The vertex type populations commonly used to motivate frustration do not take on anticipated values in the dipolar Cairo lattice, which indicates that their distribution should be random (Fig. 5.3). Despite this, all lattices still appeared to be highly disordered, reflecting a high degree of frustration and low-energy degeneracy. An effective ice rule (Fig. 5.5a-c) explains the high degree of frustration and the oddity of similar concentrations of Type A and Type B vertices (Fig. 5.4). In contrast to the Shakti lattice where this rule was first observed, long range charge ordering is absent (Fig. 5.5a-b and Fig. 5.6d). Reducing the three island vertex coupling by increasing c enables the system to break the emergent ice rule and developed charge screened states (Fig. 5.5d) similar to the dipolar dice lattice. Both high and low temperature regimes promise greater understanding of the nature of frustration and emergent phenomenon.

However, an important open question remains, namely that of the true ground state of this system and the role of long-range dipolar interactions that go beyond J_1 to J_4 (see Fig. 5.1b). This question might be addressed through computational studies [62] or improvements in the annealing procedure. Just as defects arose for spin ice in the form of emergent magnetic charges, systems deviating from equivalent energy patterns may create similar emergent carriers whose dynamics may be analyzed at higher temperature in future XMCD experiments [34, 29, 32]. The degree to which these charges are screened and their mobility may provide ideal conditions for new Debye–Hückel plasmas [33]. Such dynamic XMCD measurements might also shed light on the potential observation of emergent reduced dimensionality [39], a scenario that cannot be fully excluded with absolute certainty, based on the current results.

Part II

Artificial Spin Glass

Chapter 6

A first attempt through Gaussian disorder

6.1 Introduction

In the present work, we aim to take a first step in addressing the conceit of an artificial spin glass, first by fabricating arrays of nanomagnets exhibiting a controlled disorder and randomness, the major ingredient for the emergence of spin glass behavior. We begin with a methods section that describes the sample fabrication process and the sample characterization, employing synchrotron-based photoemission electron microscopy (PEEM). Then, we move on to a section describing the obtained results, starting from thermal annealing experiments and temperature-dependent moment fluctuations observed in randomized nanomagnetic patterns. We then conclude with a section summarizing the obtained results with conclusions and an outlook for potential future work.

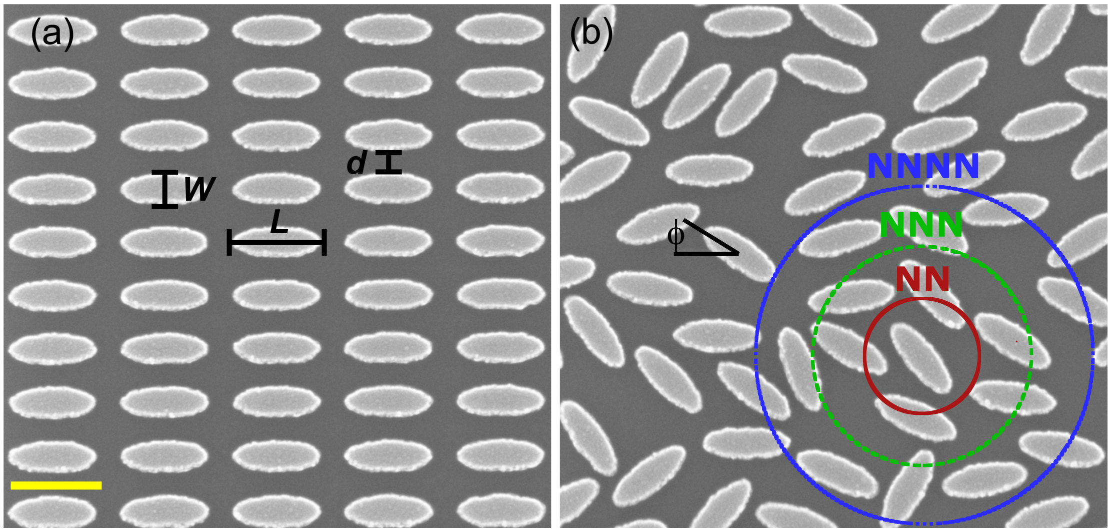

Figure 6.1: (a) Scanning electron microscope (SEM) image of part of an arrangement consisting of Ising-type nanomagnets with a length L = 300 nm, width W = 100 nm and a thickness t = 2.7 nm arranged onto a collinear ordered fashion with a nearest-neighbor edge-to-edge distance d = 80 nm. (b) SEM image of an array, where disorder in x- and y coordinates of the centers of nanomagnets is introduced in form of Gaussian distribution with a relative deviation σ = 100% around an average edge-to-edge distance of d = 80 nm. In addition to coordinate randomness, the same type of disorder is introduced for the rotational angle ϕ, ensuring maximum randomness possible in two dimensions. Circles representing the area in which spins will be designated nearest neighbor (NN, red line), next-nearest neighbor (NNN, green dashed line), and next-next-nearest neighbor (NNNN, blue dotted line) are drawn to denote categories used to calculate correlation functions.

6.2 Methods

To introduce a controlled disorder in the lattice, the islands are shifted from their lattice sites, $\mathbf{r}_{ij} = (W+d)i\hat{\mathbf{x}} + (L+d)j\hat{\mathbf{y}}$, where $W = 300$ nm is the nanomagnet width, $L = 100$ nm is the nanomagnet length, and d = 80 nm is nearest-neighbor edge-to-edge spacing (see Fig. 6.1). The x and y coordinates are displaced by values drawn from a normal distribution with a mean of zero and a standard deviation of varying percentages of d. For convenience, a standard deviation of xd is referred to as $\sigma = 100x\%$. Introducing disorder in the x- and y-coordinates results in patterns consisting of horizontal (non-rotated) nanomagnets arranged at random x and y sites. For simplicity, we call these structures the ”*non-rotated*” arrays. Further disorder is induced by introducing the same type of randomness to the orientation angle ϕ of the nanomagnets (see Fig. 6.1b). The rotational distribution is defined around 0 degrees (islands are aligned along the x-axis) with a deviation of σ_ϕ=180°σ. Since XMCD contrast in the X-PEEM experiments is angle sensitive [30] with maximum contrast, when an angle of 0° is present between the incoming X-rays and the magnetization direction (zero contrast is present for an angle of 90°), the rotation of the nanomagnets is limited to a maximum of 80°. Again, for simplicity, we call these patterns with additional rotational disorder as the ”*rotated*” arrays. Three kinds of disorder are investigated, σ= 0% (ordered), 30% (distorted) and 100% (disordered), for an edge-to-edge distance d = 80 nm. Furthermore, to ensure that nanomagnets do not overlap as a result of the introduced randomness, we define a minimum of 20 nm edge-to-edge distance when generating the random patterns. This minimum edge-to-edge distance also ensures a smooth and clean lift-off process in acetone. The overall number of nanomagnets in each individual array was 7200, occupying areas of 26-30 μm^2. These system sizes are comparable to previously studied artificial frustrated spin systems [34, 29, 32], reducing potential finite-size effects to a negligible minimum.

Magnetic imaging was performed at PEEM3 [25] at the Advanced Light Source, employing x-ray magnetic circular dichroism (XMCD) at the Fe L_3 edge [97]. XMCD images are obtained by pixelwise division of images recorded with right and left circularly polarized x-rays. The resulting XMCD contrast gives a direct measure of the projection of the magnetic moments onto the x-ray propagation vector. Moments pointing towards the incoming x-rays will appear dark, while moments opposing the x-ray direction will appear bright (see Fig. 6.2a-e). For each x-ray polarization, an exposure time of one and a half second is chosen, while switching polarizations regularly takes four seconds. This gives an overall time of roughly seven seconds to obtain an XMCD image. The aforementioned blocking temperature is chosen to fit these timescales.

6.3 Results

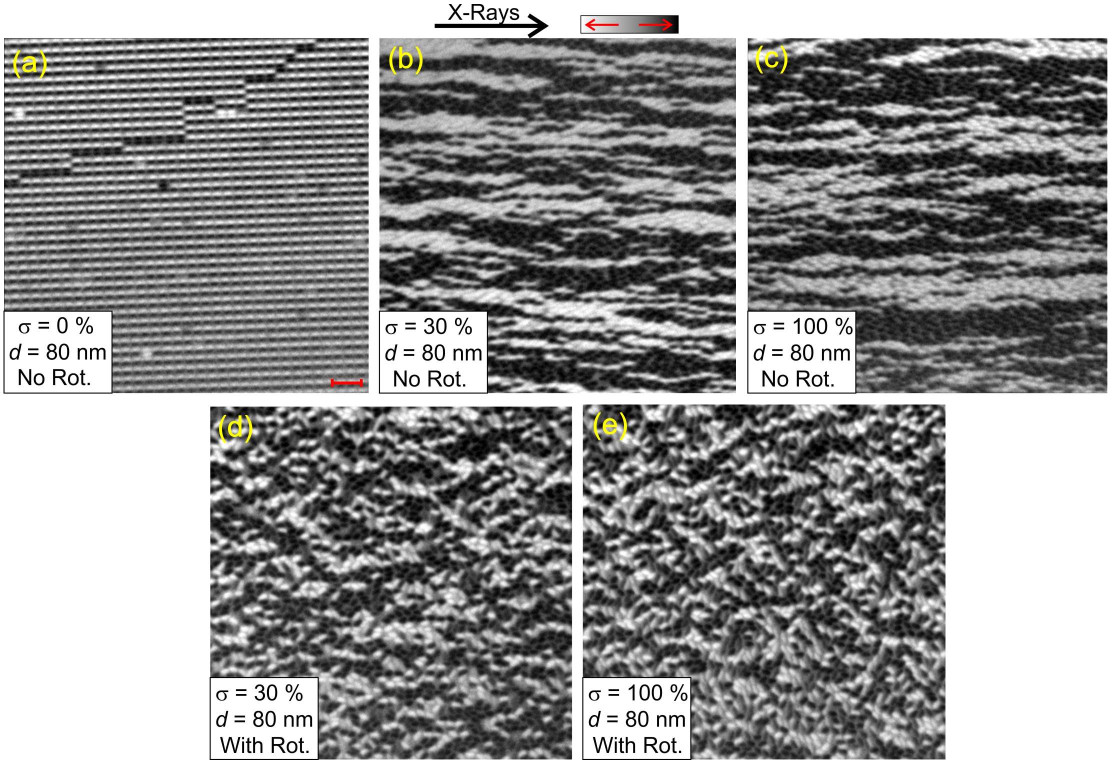

Figure 6.2: XMCD images of a low-energy moment configuration achieved, following thermal annealing in (a) a fully ordered array of Ising-type nanomagnets, (b) a partially randomized array (σ = 30%) of parallel nanomagnets (no rotational disorder), (c) a fully randomized array (σ = 100%) of parallel nanomagnets (no rotational disorder), (d) a partially randomized array (σ = 30%) with rotational disorder, and (e) a fully randomized array (σ = 100%) with rotational disorder. The red scale bar indicates 1 μm. We see a transition from a long-range ordered antiferromagnetic moment alignment for the ordered arrays, showing the characteristic dark- and bright lines (a), to a long-range ordered ferromagnetic state for the arrays with only positional disorder (b-c), ending in short-range ordered phases, when full randomness is introduced with rotational disorder (d-e).

6.3.1 Thermal Annealing

As mentioned above, we aim to explore the effect of increasing disorder and randomness on low-energy magnetic moment configurations achieved, after thermal annealing protocols [38, 34, 29]. For that purpose, the sample is heated in situ up to 350 K, where it is kept for 1-2 hours. Then, the sample is cooled down to 180 K for magnetic imaging of both time dependent dynamics and low temperature states (see Fig.6.2a-e). At these low temperatures, the moment configurations are not observed to change over time and appear to be in a frozen state. Following this annealing procedure, the regular arrays (see Fig. 6.1a) show what appear to be long-range-ordered ground state patterns consisting of anti-ferromagnetic moment alignments, seen as black and white stripes in the XMCD images (see Fig. 6.2a). Closer investigation of correlation functions will later reveal these states to be in a paramagnetic phase, but this subjective picture shows an emerging pattern that is expected to dominate at inaccessibly low temperatures. Considering the dipolar nature of inter-nanomagnet interactions, these moment configurations are not surprising [5]. Interestingly, this anti-ferromagnetic alignment of moments transforms into long-range-ordered configurations exhibiting domains of parallel (or ferromagnetic) moment alignments (see dark and bright patches in Fig. 6.2b-c) for arrays with nanomagnets where randomization is induced for the x- and y-coordinates, but where all nanomagnets remain non-rotated (see Fig. 6.2b-c). Introducing rotational randomness of the Ising-type nanomagnets, as described above, leads to more complex ordering patterns (dark and bright domains in Fig. 6.2d-e), which at least visually appear more short-range ordered compared to the non-rotated arrays.

Lattice Type	ξ (μm)	ξ/L	χ
Non-Rotated $\sigma = 0\%$	7.6	25	0.0×10^{-12}
Non-Rotated $\sigma = 30\%$	3.1	10	2.4×10^{-12}
Non-Rotated $\sigma = 100\%$	3.9	13	1.8×10^{-12}
Rotated $\sigma = 30\%$	1.2	4.1	1.7×10^{-12}
Rotated $\sigma = 100\%$	1.3	4.3	1.5×10^{-12}

Table 6.1: Correlation length ξ and magnetic susceptibility χ for magnetic configurations achieved after thermal annealing, all summarized as a function of increasing disorder σ for structures without and with rotational disorder. The third column represents the correlation length as multiples of the largest dimension of the islands, L, for greater clarity of interpretation. The first two digits of the values are displayed due to imprecision from the limited sample size.

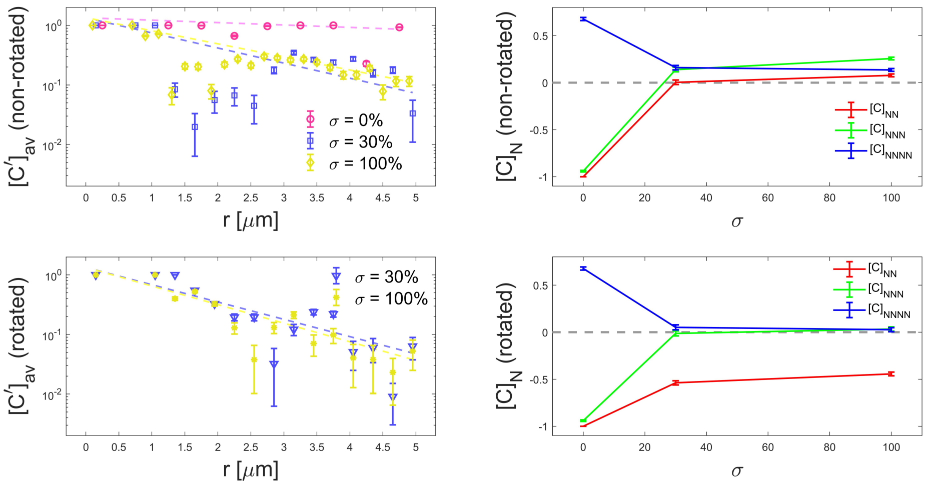

Figure 6.3: Measures of correlation in the annealed systems. On the left are the absolute value of spatial correlation functions from the (a) non-rotated and (c) rotated samples plotted on a semi-logarithmic scale with their exponential fits indicated with dashed lines. The top right plot (a) displays the non disordered (red circles), partially disordered (green squares), and fully disordered non-rotated cases (blue diamonds), while the bottom left (c) contains the partially (red triangles) and fully (blue stars) disordered rotated systems. The dotted lines represent the fits used to extract the correlation lengths. On the right are the nearest neighbor correlations of the (b) non-rotated and (d) rotated systems as disorder is varied.

To quantify this ordering, the spatial correlation function, conventional in analysis of ferromagnets and anti-ferromagnets, was calculated:

$$C(\mathbf{r}_{ij}) = \langle S_i S_j \rangle_T \tag{6.1}$$

where $S_i = \pm 1$ to represent the Ising state of spin i, r_{ij} is the distance between spins i and j, and $\langle \cdots \rangle_T$ denotes a thermal average. The absolute value of this, $C'(\mathbf{r}_{ij}) = |C(\mathbf{r}_{ij})|$, was used for correlation function calculations. After days at room temperature and subsequent gradual cooling, the systems are assumed to be in equilibrium, thus allowing/enabling to take the thermal average over time (in the temperature dependent case). This average is not possible for the annealed, frozen configurations as only one state of the system was accessed after each annealing procedure. To perform a meaningful average for a single spin configuration and more effectively extract correlation lengths in the thermally active cases, a set of bins at evenly spaced values r were chosen. All correlation function values corresponding to $r - \Delta/2 < r_{ij} < r + \Delta/2$, where Δ is the distance between consecutive r_k, were averaged to a single value,

$$[C'(r)]_{av} = \frac{1}{N_{pair}} \sum_{ij}{}' C'(\mathbf{r}_{ij}). \tag{6.2}$$

The fit of the function to the exponential $[C'(r)]_{av} = \exp(-r/\xi)$, ξ being the so-called correlation length, produced the values given in Table I. Notably, this is an order parameter that does not always diverge with spin glass transition [23, 48]. The proper spin glass order parameter is believed to be [48, 10]

$$C_{SG}(\mathbf{r}_{ij}) = \langle S_i S_j \rangle^2. \tag{6.3}$$

This function would always possess the value of one for the frozen configurations of spins, and therefore provides no information about them. For the time dependent measurements that allowed a spatial average,

$$[C_{SG}(r)]_{av} = \frac{1}{N_{pair}} \sum_{ij}' C_{SG}(\mathbf{r}_{ij}), \tag{6.4}$$

all values of this function were within their error bars from zero while $i \neq j$. Though short range correlations are likely present, this information is obscured by the current statistics.

These measures of correlation do not discern whether the system is ferro- or antiferromagnetically correlated. Therefore, a ”neighbor” correlation function is introduced:

$$[C]_{\mathrm{N}} = \frac{1}{N_{pair}} \sum_{ij}^{\mathrm{N}} C(\mathbf{r}_{ij}). \tag{6.5}$$

where the sum was either taken over nearest neighbor (NN, $r_{ij} \leq 180$ nm), next-nearest neighbor (NNN, $180 < r_{ij} \leq 360$ m), or next-next-nearest neighbor (NNNN, $360 < r_{ij} \leq 540$ nm) pairs (see Fig. 6.1b for an illustration of these regions). Since the geometry of these systems is variable, this does not strictly represent nearest neighbor coupling in a traditional sense, but does provide a consistent basis for measuring local correlations. A value below zero indicates predominantly antiferromagnetic coupling while one above zero indicates ferromagnetic coupling. These correlations are plotted for all systems of interest in Fig. 6.3b and 6.3d and confirm qualitative observations of XMCD images such as in Fig. 6.2. The alternating left-oriented stripes and right-oriented stripes of magnetic moments in the ordered system give rise to NN and NNN antiferromagnetic correlation and NNNN ferromagnetic correlation (see σ = 0 in Fig. 3b and d). When position alone is disordered, NN correlation becomes approximately evenly split, as the correlation measure approaches a value of zero (red line in Fig. 3b), while NNN and NNNN correlation is weakly ferromagnetic, strengthening with higher disorder (see Fig. 3b). The inter-nanomagnet coupling prefers ferromagnetic-type coupling when spins are moved away from their ordered state. This is mainly due to the fact that the tips of the nanomagnets exhibit the strongest interaction among each other. So, adding positional disorder leads to an increase in collinear (ferromagnetic) ordering patterns. The tip-to-tip aligned spins interact ferromagnetically by their geometry and with greater strength than anti-ferromagnetic spins aligned side to side. In other words, nanomagnets that have their ends facing each other exhibit a stronger ferromagnetic-type coupling than nanomagnets that are perfectly parallel to one another, which exhibit a weaker anti-ferromagnetic coupling. A similar effect is observed in the so-called dipolar trident lattice [29]. When rotation is introduced, however, this trend disappears. Due to the orientations changing, there is a smaller probability that these strong tip to tip interactions will be accessed. Antiferromagnetic correlation dominates for the NN interactions but equalizes for the NNN and NNNN interactions (see Fig. 6.3d). These orderings influence the critical behavior of the system as is further revealed by the temperature dependent measurements discussed in the next subsection.

The dimensionless magnetic susceptibility χ was calculated from this correlation using the fluctuation dissipation theorem [1]. This susceptibility χ was returned to appropriate dimensions by an additional factor m (the magnetic moment of a single spin, referred to as μ in the source):

$$\chi = \frac{m^2}{k_B T} \sum_{ij} C(\mathbf{r}_{ij}). \tag{6.6}$$

For the arrays discussed here, the magnetic moment m is calculated from a saturation magnetization, $M = 85$ kA/m found for similarly thin-film permalloy kagome structures [30], to be $m = 5.41 \times 10^{-18}$ Am^2. The susceptibility was extracted from the annealed configurations of all samples at 180 K (Table 1). The ordered case shows an essentially vanishing susceptibility. The true ground state of this system possesses equal proportions of positive and negative Ising spin states, corresponds to equal parts positive and negative $C(\mathbf{r}_{ij}$ which makes $\chi = 0$, in correspondence to this experimental observation. All other systems slightly decrease in susceptibility and slightly increase in correlation length with increasing disorder. The results appear contradictory as correlation lengths and susceptibility should be proportional, suggesting more data is required to determine an overarching trend between disorder and correlation.

6.3.2 Temperature-dependent moment fluctuations

Now, we turn to our attention to temperature-dependent observations of thermal fluctuations in our artificial Ising spin glass structures. To further explore the effects of disorder, the characteristic fluctuation time, τ, of both rotated- and non-rotated systems are explored, with a focus on arrays with the highest degree of introduced disorder ($\sigma = 100\%$) and freezing temperatures between 230 K and 240 K (see teal dotted lines in Fig. 6.4a-f). Below these temperatures, only a few spin islands fluctuated due to disorder intrinsic to the fabrication process. In studies of magnetic nanowires and some spin island systems, fabrication disorder can create spatial disorder that pins domain walls [54, 63]. Despite this disorder, no domain pinning effects were apparent in the time evolution of the systems, perhaps being overridden by the disorder introduced in the system's geometry. In a spin glass phase, the fluctuation timescale is expected to not remain constant over time as the system defies thermal equilibrium [83]. XMCD imaging provides the unique opportunity to directly observe this relaxation process and extract these

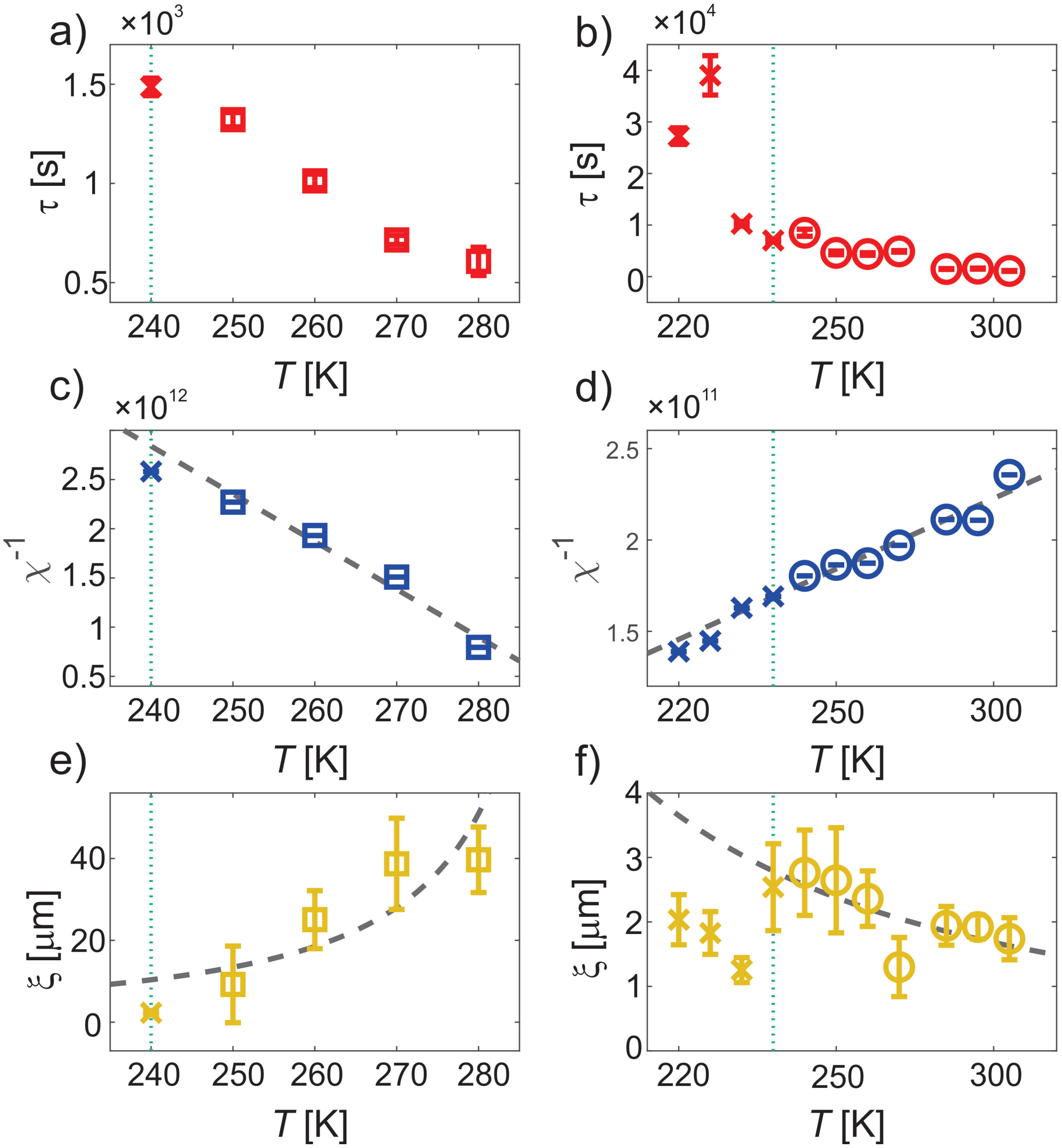

Figure 6.4: Temperature dependence of the non-rotated $\sigma = 100\%$ system (a, c, and e) and the rotated $\sigma = 100\%$ system (b, d, and f). The data points at and to the left of the teal dotted vertical lines are marked with crosses to indicate that they come from frozen configurations of spin islands. a-b) The characteristic relaxation time τ was recorded from a least squares fit of the autocorrelation function (Eqn. 6). The error bars are the standard error of this fit. c) and d) The dimensionless magnetic susceptibility for non-rotated and rotated patterns, respectively. χ was extracted from the spatial correlation function (Eqn. 5) at each frame. The averages from all frames are plotted with error bars representing standard deviations of the mean. The decreasing inverse susceptibility for non-rated patterns (blue squares) indicate long-range ferromagnetic ordering, which also visually evident in Fig. 6.2b. The grey dashed lines in c) and d) are linear Curie-Weiss fit, which imply a critical temperatures of $T_c = 298 \pm 28.8$ K for the non-rotated patterns and $T_c = 11.2 \pm 14.9$ K for the rotated patterns. e-f) The least squares fit to the spatial correlation function (Eqn. 2) produces the correlation length, ξ, whose standard error is represented by the error bars. The curves of best fit plotted as gray dashed lines correspond to critical exponents of $\nu = 1.38 \pm 0.620$ for the non-rotated case and $\nu = 1.82 \pm 0.986$ for the rotated case.

fluctuation timescales. The auto-correlation function,

$$C^{''}(t) = \langle S(t)S(t_0)\rangle, \tag{6.7}$$

where the average is taken over all spins in the system, was measured from an initial time t_0 through a time 1200 seconds later and fit the curves to an exponential decay, $C''(t) = \exp(-t/\tau)$ revealing the characteristic fluctuation time τ at each temperature (see Fig. 6.4a and b). Pearson χ^2 goodness of fit tests [100] indicated that all fits to this curve rejected the null hypothesis with 95% confidence. With only a 5% chance that this model matched the data due to random fluctuation, this result strongly implies single timescale dynamics, inconsistent with the varying timescales found in the glass phase. As seen in 6.4a and b, τ varies inversely with temperature as expected but shows no indication of a spin glass transition.

Furthermore, using the fluctuation dissipation theorem from Eqn. 5, the magnetic susceptibility was calculated at each temperature for both non-rotated and rotated arrays, and plotted in Fig. 6.4c and d, respectively. The non-rotated patterns show a decreasing inverse susceptibility with increasing temperature (see Fig. 6.4c) indicating that the system is well within a long-range ordered ferromagnetic phase, as can be visually seen from the XMCD image in 6.2b. The opposite trend is observed for rotated structures (see 6.4d). Applying a Curie-Weiss fit, $\chi = \frac{C}{T-T_c}$ to both temperature dependencies, where C is the Curie constant and T_c is the critical temperature, yields $T_c = 298 \pm 28.8$ K for the non-rotated patterns and $T_c = 11.2 \pm 14.9$ K for the rotated structures. This and all additional fits passed Pearson's χ^2 test. These temperatures differ by an order of magnitude due to the variable interaction strengths. Those strengths are higher for the non-rotated systems because the tips are more likely to be close to one another.

This highlights the potential of controlling critical temperatures through a variation of certain parameters such as disorder σ, in our particular case.

Plotting the correlation lengths as function of temperature (see Fig. 6.4e and f), the data is fitted to a power law $\xi(T) = A|(T - T_c)/T_c|^{-\nu}$ using the T_c determined from the susceptibility and leaving A, a prefactor, and ν, the critical exponent, as fitting parameters. The grey dashed lines in Fig. 6.4e and f represent these fits, $\nu = 1.38 \pm 0.620$ and $\nu = 1.82 \pm 0.986$ for the rotated and non-rotated patterns, respectively. Comparing these exponents to those of the 2D- and 3D-spin glasses ($\nu = 3.559 \pm 0.025$ [85] and $\nu = 2.15(15)$ [6], respectively) and the 2D through 4D Ising models ($\nu = 1$, $\nu = 0.6310 \pm 0.0015$ and $\nu = 0.5$ for 2, 3 and 4 dimensions, respectively [57]) further indicates that the systems investigated here, while exhibiting complex behavior, are not forming spin glass phases. The critical exponent falls below the spin glass critical exponents for two ($\nu = 3.559 \pm 0.025$ [85]) and three dimensions ($\nu = 2.15(15)$ [6]) and, considering the error, lies somewhere in the vicinity of the two dimensional Ising model ($\nu = 1$ [57]).

6.4 Discussion

Seen as a whole, these systems do not form typical spin glasses but offer hints as to how artificial spin glasses may be constructed. The random configurations should balance ferromagnetic and anti-ferromagnetic interaction to avoid ordering by either of those dominant behaviors. Patterning nanomagnet arrays to mimic higher dimensional behaviors may achieve this, perhaps through concepts such as effective dimension [22]. If interactions are structured to be more tree-like, then spin glasses can approach system-wide correlation in multiple configurations. This would translate to higher entropies corresponding to higher critical temperatures. System geometry may be modified further by randomizing spin dilution or nanomagnet sizes [67], or by introducing random height offsets [33, 75] within the system. These modifications could leverage the long range nature of dipolar interactions to shape interaction structures in methods not typically approached by purely theoretical studies. The patterned permalloy thin films analyzed here and in so-called artificial spin ices always exhibit an obstacle in the form of finite blocking temperatures, but non-zero critical temperatures would work around this limitation. Once these steps are taken and spin glass phases are realized, the real-time dynamics of such artificial spin glasses may be explored in their entirety. This unique testing grounds could probe new questions about magnetic dynamics and systems with similar mathematic descriptions, such as artificial neural networks [46], EEG data [47], and sediment deposition [48]. Furthermore, the exploration of various temperature schedules and their effect on the low-energy state achieved [41], aging and memory effects [10, 68] in prospective artificial spin glasses will be the focus of potential future research, establishing direct links to naturally occurring spin glass systems.

Chapter 7

Increasing effective dimension via the Bethe lattice

7.1 Introduction

The Gaussian patterns of Ising-type nanomagnets, while exhibiting partial short-range order, fell short in accessing a typical spin glass phase, in part because of unbalanced competing anti-ferro- and ferromagnetic ordering. This raises several open questions, regarding the prospect of realizing an artificial spin glass system. For example, can a different system design be implemented that would better optimize the balance of competing interactions in such disordered systems, so that spin glass degeneracy might arise? Also, can this goal be achieved by designing structures that would exhibit a higher effective dimension [22]?

Here, we aim to address these questions by defining dipolar-coupled Ising-type nanomagnets onto Bethe lattices (see Fig. 7.1). These structures bear three main advantages: First,

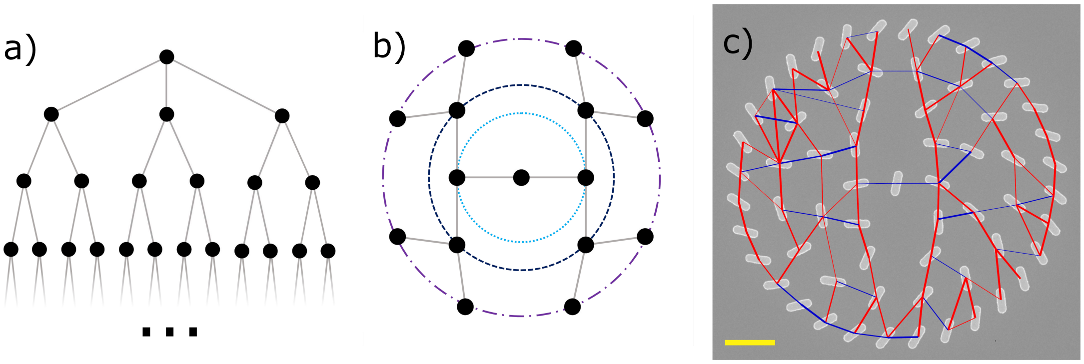

Figure 7.1: (a) An illustration of a Bethe lattice with coordination number $k = 3$. Black circles represent nodes connected by grey lines. (b) A segment of a Bethe lattice modified to be embedded in two dimensions. Each circle represents a step taken from the center of the lattice. (c) Scanning electron microscope (SEM) image of part of a Bethe lattice consisting of Ising-type nanomagnets with a length L = 300 nm, width W = 100 nm and a thickness t = 2.6 nm. The yellow scale bar corresponds to 600 nm. The tree-like structure is best understood when looking at the inter-nanomagnet dipolar couplings, which are highlighted with red (ferromagnetic coupling) and blue lines (antiferromagnetic coupling) connecting centers of nanomagnets.

their tree-like pattern increases the effective dimension [22], which is linked to accessing spin glass behavior [43]. Second, the balance of competing ferro- and antiferromagnetic interactions between the magnetic moments can be better tuned compared to structures with a simple Gaussian-type disorder [91]. Third, considering the complexity of the quest to achieve an artificial spin glass, these finite-size structures offer a comfortable building block approach in addressing this purpose. Such a bottom-up approach has already been successfully applied to gain an understanding of ordering phenomena in the highly-frustrated artificial kagome spin ice [30, 31]. We begin with a methods section that describes our theoretical approach and how dipolar Bethe structures are designed, fabricated, and characterized using X-ray photoemission electron microscopy (X-PEEM). This is followed by a section where we describe the obtained results, starting from discussing moment configurations achieved after thermal annealing and the characterization of these ordering patterns in terms of spin correlations, effective dimension, and potential links to glassy behavior. We then conclude with a summary and outlook section where we assess the advantages of our Bethe structures as promising building blocks for the generation of the first artificial spin glass systems.

7.2 Methods

The illustrated network was formed by first considering the dipolar coupling strength between islands i and j,

$$J_{ij} = -\frac{\mu_0}{4\pi}\left(\frac{\mathbf{S}_i \cdot \mathbf{S}_j}{r_{ij}^3} - 3\frac{(\mathbf{S}_i \cdot \mathbf{r}_{ij})(\mathbf{S}_j \cdot \mathbf{r}_{ij})}{r_{ij}^5}\right), \tag{7.1}$$

where μ_0 is the permittivity of free space, $\mathbf{S}_i$ is the magnetic moment of an island, and $\mathbf{r}_{ij}$ is the vector joining the center of two islands. If J_{ij} is less than zero, the coupling is anti-ferromagnetic (blue lines in Fig. 7.1c), and if it is higher than zero, the coupling is ferromagnetic (red lines in Fig. 7.1c). Where the magnitude of their dipole-dipole coupling was greater than 20% of maximum magnitude, two spins are considered connected. Visualizing this network (see red and blue lines in Fig. 7.1c), a randomly modified tree-like network is apparent. The most prominent violations to pure tree-like structures occur in the outer ring as crowding increases interaction strengths. Overall, we designed, fabricated and imaged 21 individual randomly generated Bethe structures using this theoretical concept. The interaction networks of these lattices are used to assess the effective dimension of the magnetic systems.

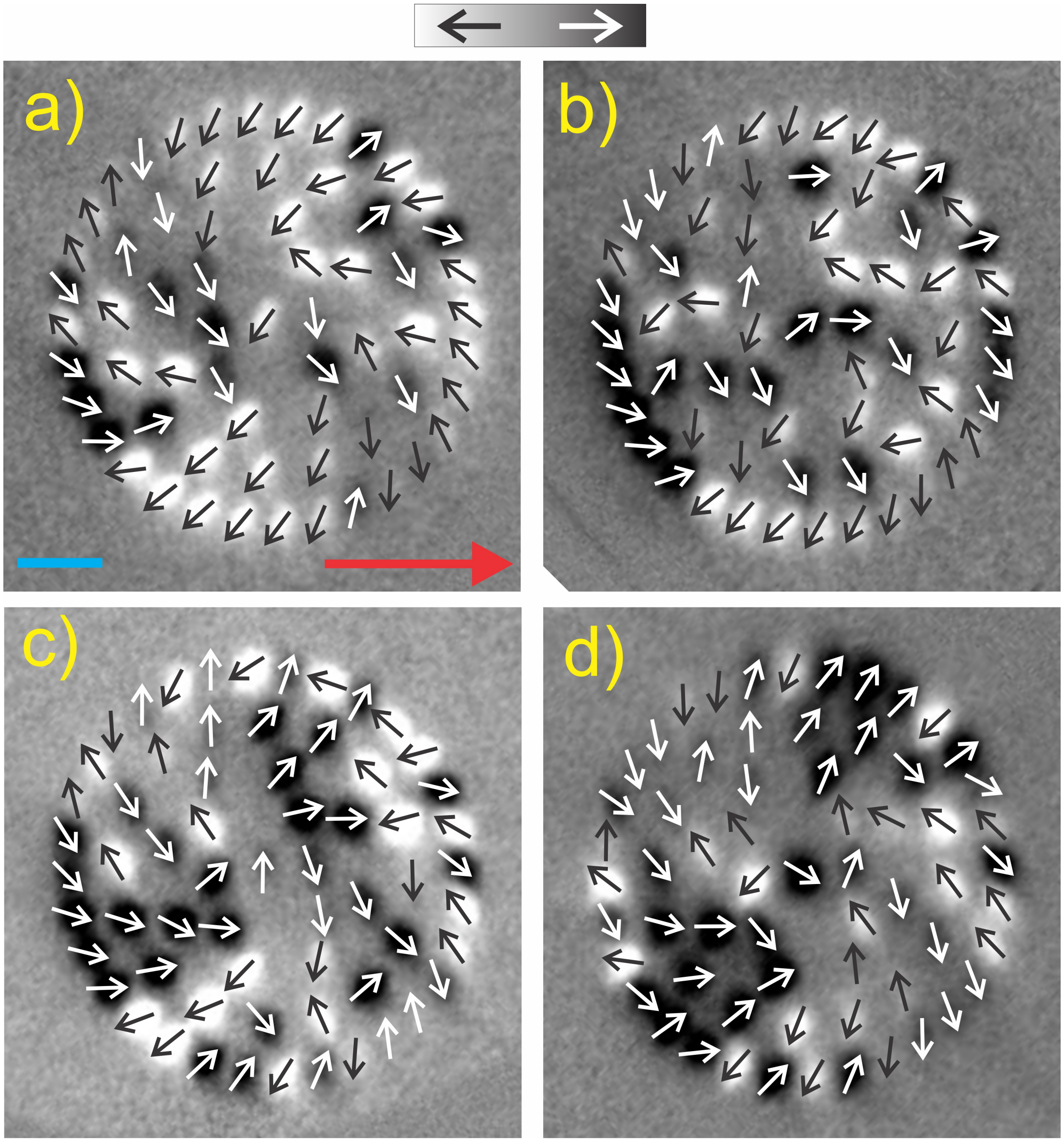

Figure 7.2: (a)-(d) XMCD images of low-energy states achieved in four different Bethe structures, after thermal annealing. Moments pointing towards the incoming x-rays (big red arrow) will appear dark, while moments opposing the incoming x-ray direction will appear bright. The blue bar indicates a length of 600 nm.

7.2.1 Sample fabrication and XMCD imaging

Following sample fabrication, and after a waiting period of three days in high vacuum at room temperature (T = 298 K), the samples are transferred into a photoemission electron microscope (PEEM) [59]. There, the sample was cooled down to temperatures around 120 K, ensuring that magnetic moments stay frozen within the timescale of hours, and magnetic imaging was performed employing x-ray magnetic circular dichroism (XMCD) at the Fe L_3 edge[97]. The dark and bright contrast in a so-called XMCD image is a direct measure of the orientation of the magnetic moment of a nanomagnet relative to the x-ray polarization vector (see Fig. 7.2).

7.3 Results

7.3.1 Spin-spin correlations and ordering preferences

The relatively small size of these systems does not provide enough statistical relevance for a reliable extraction of typical or spin glass correlation lengths. However, since our concern is equalizing anti-ferro- and ferromagnetic ordering, we focus on local correlations. Using a similar approach as in our most recent work [91], we introduce a neighbor correlation function:

$$[C]_{\mathrm{N}} = \frac{1}{N_{pair}} \sum_{ij}^{\mathrm{N}} \langle \Theta(\mathbf{S}_i \cdot \mathbf{S}_j) \rangle_T . \tag{7.2}$$

$\Theta(x) = -1$ if x is less than zero and $\Theta(x) = 1$ otherwise, the sum was either taken over nearest neighbor (NN, $r_{ij} \leq a$), next-nearest neighbor (NNN, $r_{ij} \leq 2a$), or next-next-nearest neighbor (NNNN, $r_{ij} \leq 3a$) pairs, and N_{pair} is the number of those pairs in a particular sum. This provides a consistent basis for measuring local correlations in these systems without translational

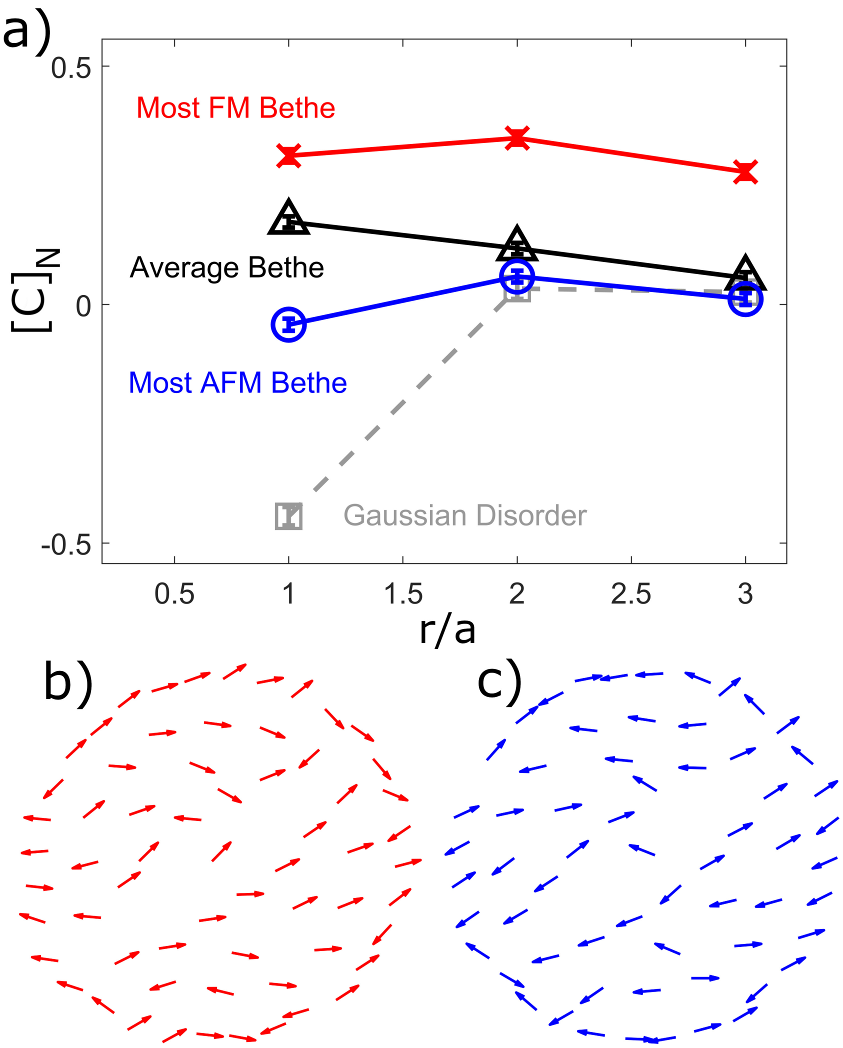

Figure 7.3: Neighbor correlations in randomized magnetic systems. In (a), the nearest-neighbor ($r/a = 1$), next-nearest-neighbor ($r/a = 2$), and next-next-nearest neighbor ($r/a = 3$) correlations are plotted for the most ferromagnetically ordered Bethe system (red crosses), the average Bethe system (black triangles), the most anti-ferromagnetically ordered Bethe system (blue circles) and the most disordered system from a previously investigated artificial spin system with Gaussian disorder[91] (gray squares). (b) Moment configurations of the Bethe structure with the highest degree of ferromagnetic-type ordering [red crosses and lines in (a)]. (c) Moment configurations of the Bethe structure with the strongest anti-ferromagnetic spin ordering [blue circles and lines in (a)].

invariance. A value below zero indicates predominantly antiferromagnetic coupling while one above zero indicates ferromagnetic coupling. These correlations are plotted for all systems of interest in Fig. 7.3a.

A glance at these correlation measures reveals that nearest-neighbor correlations in the Bethe structures have a weaker anti-ferromagnetic tendency when compared to structures with Gaussian disorder [91] (compare blue, black and red lines with dotted grey line in Fig 7.3a.). There seems a tendency towards more ferromagnetic-type ordering in the Bethe structures, which can even be visually seen when looking at magnetic configurations shown in Fig. 7.2 through the small clusters of moments pointing in the same direction. Overall, the balance of ferro- and antiferromagnetic correlations is significantly improved in comparison to structures with Gaussian disorder [91], as indicated by nearest-neighbor correlations that are closer to zero (see Fig. 7.3a). As seen in Fig. 7.3b-c, this is manifested by a reduction of the ferromagnetic cluster size and regions of anti-ferromagnetic ordering. These results provide a first strong indication that such tree-like structures are better candidates in achieving artificial spin glasses. However, a finite non-zero spin glass transition temperature is still an obstacle that needs to be overcome [43, 91]. One strategy moving towards that goal relies on elevating the effective dimensions of such disordered structures, which is discussed in the following subsection.

7.3.2 Effective dimension

The dipolar Bethe lattices discussed here, as any other artificial frustrated system, can be viewed as a network that consists of nodes (nanomagnets) and their connections (dipolar coupling between nanomagnets). While this network is embedded in two-dimensional space,

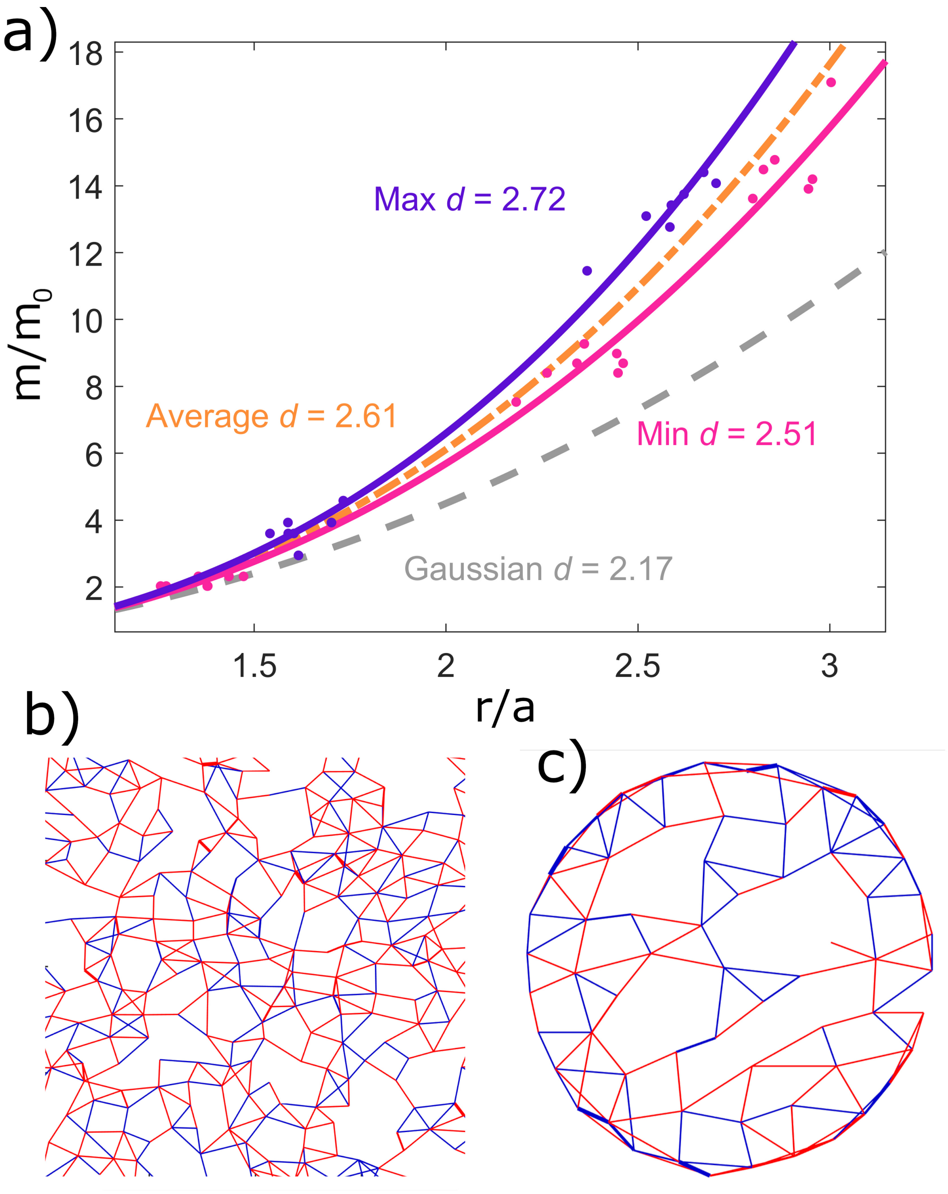

Figure 7.4: Effective dimension of randomized magnetic systems. (a) $m(r)$ and its fits are plotted to demonstrate effective dimension d. The purple and pink circles represent data from the Bethe lattices with the largest ($d = 2.72$) and smallest ($d = 2.51$) effective dimensions, respectively, while the curves of corresponding color are their fits. The dashed curve represents the average effective dimension of all 21 investigated Bethe structures ($d = 2.61$). The dashed grey line corresponds to the effective dimension ($d = 2.17$) of a system with mere Gaussian disorder [91]. (b) and (c) Representative graphs of interactions for systems with Gaussian disorder and a typical Bethe lattice, respectively.

inter-nanomagnet connections via dipolar coupling go beyond neighboring nanomagnets. As we will explain here, this can be used to elevate effective dimension [22]. The notion of an effective network dimension may be understood in terms of how ”scale” and ”mass” relate to one another in different dimensions. One could consider a hypothetical shape existing in an arbitrary dimension, d'. Its size may be changed by altering a length scale r' (the side length of a cube or a golden rectangle, for example). How does mass, or some other quantity present in the space, encompassed by this shape relate to this scale? If the density is constant and the dimension is an integer, the answer is simple. $m'(r') = m'_0 r'^{d'}$ where $m'(r')$ is the mass, m'_0 is the mass of the shape when $r' = 1$, r' is the scale of that shape, and d' is the dimension. Because d' is the exponent, we can tell that larger dimensions allow access to more ”stuff” (mass, charge, magnetic moments etc.) with less scale. If the density is not constant or there are different ways of leaping from place to place, more or less stuff may be accessed than what is considered typical for dimension d'. In these more complex systems, d' is replaced with d and is allowed to vary as a real number, taking on the name ”effective dimension” [22]. This definition is non-trivial as it allows the comparison of theoretical models on non-integer dimensions to real models with non-integer effective dimensions [22]. In spin glass models, the spin glass transition temperature depends on the effective dimension and for a critical dimension of $d_c = 2.520$ the spin glass transition temperature has been predicted to be finite [24]. We will compare the effective dimension of our systems to this critical value to assess their viability as spin glasses.

To calculate the effective dimension of our experimental spin systems, a spin i corresponding to a point $\mathbf{r}_{l=0}$ was chosen. l labels the degree of separation from this spin. All spins connected to spin i, those with coupling strength J_{ij} exceeding 20% the maximum strength, were accessed. The average distance between connected spins and the initial spin, $r_{l=1}$, was calculated. This can be considered the ”scale” of the network’s ”shape.” The total number of spins with this proximity, $m(r_{l=1})$ (in analogy the mass of a shape), were counted. This was repeated for further steps away from the center ($l = 2$ through 5, see the colored dots in Fig. 7.4a). The process was reiterated for all spins i less than 1.3 μm from the center of the lattice to avoid edge effects. The resulting data were fit to $m(r) = m_0 r^d$ via linear regression to determine d, the effective dimension (see curves of best fit and text in Fig. 7.4a). Notably, a true Bethe lattice’s density of nodes would exponentially grow from the origin, thus making the effective dimension infinite. In our case, the effective dimensions of the finite-sized Bethe lattices exceed that of previously studied systems with Gaussian disorder [91], $d = 2.17$ (see Fig. 7.4a) and the critical dimension $d_c = 2.520$. They exhibit average effective dimension of 2.61 and a maximum d = 2.72 (see Fig. 7.4a). Fig. 7.4b-c shows that the Bethe lattice interaction structures expand this effective dimension with their tree like arrangement. Though this is not infinite and never could be due to the constraints of two dimensional embedding, it is high enough to anticipate a change in system dynamics. We conclude that a prospective extended structure built on an interaction concept similar to Fig. 7.4c could have the appropriate effective dimension and balance of competing interactions that would allow the realization of the first artificial Ising spin glass.

7.4 Discussion

Despite the inherent difficulties in building tree like interaction networks in two dimensions, our artificial Bethe glass building blocks overcome previous limitations in artificial spin glass systems. However, not all randomly generated samples possess the same physics because of variations in the balancing ferro- and antiferromagnetic interactions. The finite size of our samples produces fluctuations from average ordering (black triangles in Fig. 3a), allowing individual samples to exhibit more ideally balanced ordering ($[C]_N \approx 0$, see blue circles in Fig. 3a). This tunability is a substantial improvement over ordering in systems with Gaussian disorder (gray squares in Fig 3a). Though less markedly variable, the effective dimension of the Bethe lattice is also tunable, ranging from just below d_c at $d = 2.51$ all the way to $d = 2.72$. Even though long range interactions break the perfect Bethe lattice structure (see Fig. 7.4c), its dimension almost always remains high enough to allow a finite temperature spin glass transition. By contrast, the purely Gaussian-disordered system [91] did not alter its interactions into a network with high enough effective dimension (Fig. 4b), so that finite-temperature spin glass phase could be accessed.

This work has taken two outstanding problems, unbalanced ordering and low effective dimension, and condensed them into one: making a larger Bethe lattice system. This clear next step would allow for a raised spin glass transition temperature and novel, direct observation of spin glass dynamics via XMCD imaging. By simulating combinations of Bethe lattices before they are fabricated, they may be vetted for balanced ordering and high effective dimension. This future work would use model systems to bridge the gap between spin glass theory and experiment by exploring non-equilibrium thermodynamics of the spin glass phase.

Chapter 8

Conclusion

As a whole, this former half of this work distinguishes important features of the spin ice field. All three systems investigated possessed geometric frustration, but their deviations from frustrated ground states differed. Though a diffuse structure factor was previously considered a trait of the Coulomb phase in square and pyrochlore lattices, such a feature also emerged in the trident lattice, which contains no magnetic analogue to Coulomb charges. Indeed, frustration pointed to by diffuse structure factors is needed for a unbiased, divergence free "vacuum" of the Coulomb phase[16, 44, 75], but definitive proof of charge like behavior requires further evidence in analogy to other models, such as the Debye-Hückel theory [53, 58, 17, 48]. The mixed coordination disorder of the Cairo lattice expressed another relevant feature: charge screening and resulting polarons [34, 20]. Since coordination three vertices never become charge neutral, the charge energetics favor screening of fields rather than free monopoles. Further, the notion of vertex type enforced ergodicity (1/3 type I vertices and 2/3 type II) is superseded by the topological order forcing a fifty-fifty ratio of the two [38]. Presumably there are even more undiscovered forms of competition that lead to alternate spin textures to coexist and different emergent states to develop.

Spin glasses require a bit more fine tuning before they are accessible in artificial spin systems. The preliminary work within this thesis explores the intermediate temperature, low dimension sector of a conceptual "phase space." At an ideal balance of ferromagnetic and anti-ferromagnetic interaction, the transition to a spin glass phase may be sought [10]. Our first spin glass chapter showed the importance of rotational disorder in balancing these interactions, while the second increased the transition temperature through elevated effective dimension. Unfortunately, this heightened dimension sacrificed system size, making the statistics inadequate to analyze whether or not the spin glass phase existed. Knowing it is possible to raise effective dimension [22], their are three plausible routes forward: carefully balance statistics and effective dimension with the same tree-like structures, define an extensive structure with increased effective dimension, or forgo the concept of effective dimension entirely and focus on another feature correlated with increased spin glass transition temperature.

In terms of broader impact, the details of the Coulomb phase in the offset square lattice and spin glass phase are of primary importance to fundamental science. They are at once model systems for the microscopic equivalents of these phases and their own beasts entirely, confined by the rules of spin by spin relaxation and the requirement of overcoming internal coercivity [49]. Recent publications have begun to unravel the connection between complicated relaxation pathways and tweaked Coulomb phases. Further, just observing the relaxation itself and connecting said relaxation with out of equilibrium dynamics predicted by Debye-Hückel

[58], Onsager-Wien [51], and other plasma theories requires much more experimentation. Once spin glass phases are accessible, probing the spin glass ground state will be helpful to understanding equivalent NP hard problems [108] and brain science models [47]. The freedom to tweak these system's geometry will allow representation of other computing problems. It has already been shown that nanomagnetic systems may potentially approach the Landauer limit at room temperature [56] and thus make excellent candidates for low energy computing. Altogether, access to these system's thermodynamics and details of interaction strength allows for a rich tool in comprehending novel phases.

Bibliography

[1] Sergey G Abaimov. Correlations, susceptibility, and the fluctuation–dissipation theorem. pages 289–364, 2015.

[2] P. Amornpitoksuk, D. Ravot, A. Mauger, and J. C. Tedenac. Structural and magnetic properties of the ternary solid solution between cosb and fe$_{1+\delta}$Sb. *Phys. Rev. B*, 77:144405, Apr 2008.

[3] V. K. Anand, D. T. Adroja, A. D. Hillier, J. Taylor, and G. André. Signatures of spin-glass behavior in the induced magnetic moment system prrusi$_3$. *Phys. Rev. B*, 84:064440, Aug 2011.

[4] L Anghinolfi, H Luetkens, J Perron, MG Flokstra, O Sendetskyi, A Suter, T Prokscha, PM Derlet, SL Lee, and LJ Heyderman. Thermodynamic phase transitions in a frustrated magnetic metamaterial. *Nature communications*, 6:8278, 2015.

[5] Unnar B Arnalds, Jonathan Chico, Henry Stopfel, Vassilios Kapaklis, Oliver Bärenbold, Marc A Verschuuren, Ulrike Wolff, Volker Neu, Anders Bergman, and Björgvin Hjörvarsson. A new look on the two-dimensional ising model: thermal artificial spins. *New Journal of Physics*, 18(2):023008, 2016.

[6] H. G. Ballesteros, A. Cruz, L. A. Fernández, V. Martín-Mayor, J. Pech, J. J. Ruiz-Lorenzo, A. Tarancón, P. Téllez, C. L. Ullod, and C. Ungil. Critical behavior of the three-dimensional ising spin glass. *Phys. Rev. B*, 62:14237–14245, Dec 2000.

[7] Deb Sankar Banerjee. *Direct calculation of Madelung constant*. PhD thesis, thesis, Indian Institute of Technology Madras, 2012.

[8] Ludovic Berthier and Giulio Biroli. Theoretical perspective on the glass transition and amorphous materials. *Rev. Mod. Phys.*, 83:587–645, Jun 2011.

[9] V. S. Bhat, F. Heimbach, I. Stasinopoulos, and D. Grundler. Magnetization dynamics of topological defects and the spin solid in a kagome artificial spin ice. *Phys. Rev. B*, 93:140401, Apr 2016.

[10] K. Binder and A. P. Young. Spin glasses: Experimental facts, theoretical concepts, and open questions. *Rev. Mod. Phys.*, 58:801–976, Oct 1986.

[11] V. Brajuskovic, A. Addi, C. Phatak, and A. K. Petford-Long. Observation of transient states during magnetization reversal in a quasicrystal artificial spin ice. *Phys. Rev. B*, 98:094424, Sep 2018.

[12] Steven T Bramwell and Michel JP Gingras. Spin ice state in frustrated magnetic pyrochlore materials. *Science*, 294(5546):1495–1501, 2001.

[13] ME Brooks-Bartlett, Simon T Banks, Ludovic DC Jaubert, Adam Harman-Clarke, and Peter CW Holdsworth. Magnetic-moment fragmentation and monopole crystallization. *Physical Review X*, 4(1):011007, 2014.

[14] Benjamin Canals, Ioan-Augustin Chioar, Van-Dai Nguyen, Michel Hehn, Daniel Lacour, François Montaigne, Andrea Locatelli, Tevfik Onur Menteş, Benito Santos Burgos, and Nicolas Rougemaille. Fragmentation of magnetism in artificial kagome dipolar spin ice. *Nature communications*, 7:11446, 2016.

[15] JM Carlson, JT Chayes, L Chayes, JP Sethna, and DJ Thouless. Critical behavior of the bethe lattice spin glass. *EPL (Europhysics Letters)*, 5(4):355, 1988.

[16] Claudio Castelnovo, Roderich Moessner, and Shivaji L Sondhi. Magnetic monopoles in spin ice. *Nature*, 451(7174):42, 2008.

[17] Claudio Castelnovo, Roderich Moessner, and Shivaji Lal Sondhi. Debye-hückel theory for spin ice at low temperature. *Physical Review B*, 84(14):144435, 2011.

[18] Gia-Wei Chern and Paula Mellado. Magnetic monopole polarons in artificial spin ices. *EPL (Europhysics Letters)*, 114(3):37004, 2016.

[19] Gia-Wei Chern, Paula Mellado, and O Tchernyshyov. Two-stage ordering of spins in dipolar spin ice on the kagome lattice. *Physical review letters*, 106(20):207202, 2011.

[20] Gia-Wei Chern and Oleg Tchernyshyov. Magnetic charge and ordering in kagome spin ice. *Philosophical Transactions of the Royal Society A: Mathematical, Physical and Engineering Sciences*, 370(1981):5718–5737, 2012.

[21] IA Chioar, Benjamin Canals, D Lacour, M Hehn, B Santos Burgos, TO Menteş, A Locatelli, F Montaigne, and Nicolas Rougemaille. Kinetic pathways to the magnetic charge crystal in artificial dipolar spin ice. *Physical Review B*, 90(22):220407, 2014.

[22] Li Daqing, Kosmas Kosmidis, Armin Bunde, and Shlomo Havlin. Dimension of spatially embedded networks. *Nature Physics*, 7(6):481, 2011.

[23] C Dasgupta, AV Indrani, Sriram Ramaswamy, and MK Phani. Is there a growing correlation length near the glass transition? *EPL (Europhysics Letters)*, 15(3):307, 1991.

[24] Mehmet Demirtaş, Aslı Tuncer, and A Nihat Berker. Lower-critical spin-glass dimension from 23 sequenced hierarchical models. *Physical Review E*, 92(2):022136, 2015.

[25] Andrew Doran, Matthew Church, Tom Miller, Greg Morrison, Anthony T Young, and Andreas Scholl. Cryogenic peem at the advanced light source. *Journal of Electron Spectroscopy and Related Phenomena*, 185(10):340–346, 2012.

[26] Jasper Drisko, Thomas Marsh, and John Cumings. Topological frustration of artificial spin ice. *Nature communications*, 8:14009, 2017.

[27] David J Earl and Michael W Deem. Parallel tempering: Theory, applications, and new perspectives. *Physical Chemistry Chemical Physics*, 7(23):3910–3916, 2005.

[28] A Farhan, PM Derlet, A Kleibert, A Balan, RV Chopdekar, M Wyss, L Anghinolfi, F Nolting, and Laura J Heyderman. Exploring hyper-cubic energy landscapes in thermally active finite artificial spin-ice systems. *Nature Physics*, 9(6):375, 2013.

[29] Alan Farhan, Peter M Derlet, Luca Anghinolfi, Armin Kleibert, and Laura J Heyderman. Magnetic charge and moment dynamics in artificial kagome spin ice. *Physical Review B*, 96(6):064409, 2017.

[30] Alan Farhan, Peter M Derlet, Armin Kleibert, Ana Balan, Rajesh V Chopdekar, Marcus Wyss, Jonathan Perron, Andreas Scholl, Frithjof Nolting, and Laura J Heyderman. Direct observation of thermal relaxation in artificial spin ice. *Physical review letters*, 111(5):057204, 2013.

[31] Alan Farhan, Armin Kleibert, Peter M Derlet, Luca Anghinolfi, Ana Balan, Rajesh V Chopdekar, Marcus Wyss, Sebastian Gliga, Frithjof Nolting, and Laura J Heyderman. Thermally induced magnetic relaxation in building blocks of artificial kagome spin ice. *Physical Review B*, 89(21):214405, 2014.

[32] Alan Farhan, Charlotte F Petersen, Scott Dhuey, Luca Anghinolfi, Qi Hang Qin, Michael Saccone, Sven Velten, Clemens Wuth, Sebastian Gliga, Paula Mellado, et al. Nanoscale control of competing interactions and geometrical frustration in a dipolar trident lattice. *Nature communications*, 8(1):995, 2017.

[33] Alan Farhan, Michael Saccone, Charlotte F Petersen, Scott Dhuey, Rajesh V Chopdekar, Yen-Lin Huang, Noah Kent, Zuhuang Chen, Mikko J Alava, Thomas Lippert, et al. Emergent magnetic monopole dynamics in macroscopically degenerate artificial spin ice. *Science advances*, 5(2):eaav6380, 2019.

[34] Alan Farhan, Andreas Scholl, Charlotte F Petersen, Luca Anghinolfi, Clemens Wuth, Scott Dhuey, Rajesh V Chopdekar, Paula Mellado, Mikko J Alava, and Sebastiaan Van Dijken. Thermodynamics of emergent magnetic charge screening in artificial spin ice. *Nature Communications*, 7:12635, 2016.

[35] B. Farmer, V. S. Bhat, A. Balk, E. Teipel, N. Smith, J. Unguris, D. J. Keavney, J. T. Hastings, and L. E. De Long. Direct imaging of coexisting ordered and frustrated sublattices in artificial ferromagnetic quasicrystals. *Phys. Rev. B*, 93:134428, Apr 2016.

[36] Mingxuan Fu, Takashi Imai, Tian-Heng Han, and Young S Lee. Evidence for a gapped spin-liquid ground state in a kagome heisenberg antiferromagnet. *Science*, 350(6261):655–658, 2015.

[37] Sean R Giblin, Steven T Bramwell, Peter CW Holdsworth, Dharmalingam Prabhakaran, and Ian Terry. Creation and measurement of long-lived magnetic monopole currents in spin ice. *Nature Physics*, 7(3):252–258, 2011.

[38] Ian Gilbert, Gia-Wei Chern, Sheng Zhang, Liam O'Brien, Bryce Fore, Cristiano Nisoli, and Peter Schiffer. Thermodynamics of emergent magnetic charge screening in artificial spin ice. *Nature Physics*, 10:670, 2014.

[39] Ian Gilbert, Yuyang Lao, Isaac Carrasquillo, Liam O'Brien, Justin D Watts, Michael Manno, Chris Leighton, Andreas Scholl, Cristiano Nisoli, and Peter Schiffer. Emergent reduced dimensionality by vertex frustration in artificial spin ice. *Nature Physics*, 12(2):162, 2016.

[40] Sebastian Gliga, Attila Kákay, Riccardo Hertel, and Olle G. Heinonen. Spectral analysis of topological defects in an artificial spin-ice lattice. *Phys. Rev. Lett.*, 110:117205, Mar 2013.

[41] Gary S. Grest, C. M. Soukoulis, and K. Levin. Cooling-rate dependence for the spin-glass ground-state energy: Implications for optimization by simulated annealing. *Phys. Rev. Lett.*, 56:1148–1151, Mar 1986.

[42] Mark J Harris, ST Bramwell, DF McMorrow, TH Zeiske, and KW Godfrey. Geometrical frustration in the ferromagnetic pyrochlore ho 2 ti 2 o 7. *Physical Review Letters*, 79(13):2554, 1997.

[43] A. K. Hartmann and A. P. Young. Lower critical dimension of ising spin glasses. *Phys. Rev. B*, 64:180404, Oct 2001.

[44] Christopher L Henley. The "coulomb phase" in frustrated systems. *Annu. Rev. Condens. Matter Phys.*, 1(1):179–210, 2010.

[45] CL Henley. Power-law spin correlations in pyrochlore antiferromagnets. *Physical Review B*, 71(1):014424, 2005.

[46] John J Hopfield. Neurons with graded response have collective computational properties like those of two-state neurons. *Proceedings of the national academy of sciences*, 81(10):3088–3092, 1984.

[47] Anthony G Hudetz, Colin J Humphries, and Jeffrey R Binder. Spin-glass model predicts metastable brain states that diminish in anesthesia. *Frontiers in systems neuroscience*, 8:234, 2014.

[48] Ludovic DC Jaubert and Peter CW Holdsworth. Signature of magnetic monopole and dirac string dynamics in spin ice. *Nature Physics*, 5(4):258, 2009.

[49] Johannes H Jensen, Anders Strømberg, Odd Rune Lykkebø, Arthur Penty, Magnus Själander, Erik Folven, and Gunnar Tufte. flatspin: A large-scale artificial spin ice simulator. *arXiv preprint arXiv:2002.11401*, 2020.

[50] M. B. Jungfleisch, W. Zhang, E. Iacocca, J. Sklenar, J. Ding, W. Jiang, S. Zhang, J. E. Pearson, V. Novosad, J. B. Ketterson, O. Heinonen, and A. Hoffmann. Dynamic response of an artificial square spin ice. *Phys. Rev. B*, 93:100401, Mar 2016.

[51] Vojtech Kaiser, Steven T Bramwell, Peter CW Holdsworth, and Roderich Moessner. Onsager's wien effect on a lattice. *Nature materials*, 12(11):1033, 2013.

[52] Vassilios Kapaklis, Unnar B Arnalds, Alan Farhan, Rajesh V Chopdekar, Ana Balan, Andreas Scholl, Laura J Heyderman, and Björgvin Hjörvarsson. Thermal fluctuations in artificial spin ice. *Nature nanotechnology*, 9(7):514, 2014.

[53] Vladimir Kobelev, Anatoly B Kolomeisky, and Michael E Fisher. Lattice models of ionic systems. *The Journal of chemical physics*, 116(17):7589–7598, 2002.

[54] Sam Ladak, Dan Read, Tolek Tyliszczak, Will R Branford, and Lesley F Cohen. Monopole defects and magnetic coulomb blockade. *New Journal of Physics*, 13(2):023023, 2011.

[55] Sam Ladak, DE Read, GK Perkins, LF Cohen, and WR Branford. Direct observation of magnetic monopole defects in an artificial spin-ice system. *Nature Physics*, 6(5):359, 2010.

[56] Brian Lambson, David Carlton, and Jeffrey Bokor. Exploring the thermodynamic limits of computation in integrated systems: Magnetic memory, nanomagnetic logic, and the landauer limit. *Physical review letters*, 107(1):010604, 2011.

[57] Jean Claude Le Guillou and Jean Zinn-Justin. Accurate critical exponents for ising like systems in non-integer dimensions. *Journal de physique*, 48(1):19–24, 1987.

[58] Yan Levin. Electrostatic correlations: from plasma to biology. *Reports on progress in physics*, 65(11):1577, 2002.

[59] E Mengotti, LJ Heyderman, A Fraile Rodriguez, A Bisig, L Le Guyader, F Nolting, and HB Braun. Building blocks of an artificial kagome spin ice: Photoemission electron microscopy of arrays of ferromagnetic islands. *Physical Review B*, 78(14):144402, 2008.

[60] Marc Mézard and Giorgio Parisi. The bethe lattice spin glass revisited. *The European Physical Journal B-Condensed Matter and Complex Systems*, 20(2):217–233, 2001.

[61] Gunnar Möller and R Moessner. Artificial square ice and related dipolar nanoarrays. *Physical Review Letters*, 96(23):237202, 2006.

[62] Gunnar Möller and Roderich Moessner. Magnetic multipole analysis of kagome and artificial spin-ice dipolar arrays. *Physical Review B*, 80(14):140409, 2009.

[63] Jason P Morgan, Aaron Stein, Sean Langridge, and Christopher H Marrows. Thermal ground-state ordering and elementary excitations in artificial magnetic square ice. *Nature Physics*, 7(1):75, 2011.

[64] SA Morley, D Alba Venero, JM Porro, ST Riley, A Stein, P Steadman, RL Stamps, S Langridge, and CH Marrows. Vogel-fulcher-tammann freezing of a thermally fluctuating artificial spin ice probed by x-ray photon correlation spectroscopy. *Physical Review B*, 95(10):104422, 2017.

[65] Sophie A Morley, Susan T Riley, Jose-Maria Porro, Mark C Rosamond, Edmund H Linfield, John E Cunningham, Sean Langridge, and Christopher H Marrows. Effect of fepd alloy composition on the dynamics of artificial spin ice. *Scientific reports*, 8(1):4750, 2018.

[66] David Jonathan Pryce Morris, DA Tennant, SA Grigera, B Klemke, C Castelnovo, R Moessner, C Czternasty, M Meissner, KC Rule, J-U Hoffmann, et al. Dirac strings and magnetic monopoles in the spin ice dy2ti2o7. *Science*, 326(5951):411–414, 2009.

[67] Muir J Morrison, Tammie R Nelson, and Cristiano Nisoli. Unhappy vertices in artificial spin ice: new degeneracies from vertex frustration. *New Journal of Physics*, 15(4):045009, 2013.

[68] JA Mydosh. Spin glasses: redux: an updated experimental/materials survey. *Reports on Progress in Physics*, 78(5):052501, 2015.

[69] Cristiano Nisoli, Roderich Moessner, and Peter Schiffer. Colloquium: Artificial spin ice: Designing and imaging magnetic frustration. *Rev. Mod. Phys.*, 85:1473–1490, Oct 2013.

[70] Cristiano Nisoli, Roderich Moessner, and Peter Schiffer. Colloquium: Artificial spin ice: Designing and imaging magnetic frustration. *Reviews of Modern Physics*, 85(4):1473, 2013.

[71] Massimo Ostilli. Cayley trees and bethe lattices: A concise analysis for mathematicians and physicists. *Physica A: Statistical Mechanics and its Applications*, 391(12):3417–3423, 2012.

[72] Erik Östman, Henry Stopfel, Ioan-Augustin Chioar, Unnar B Arnalds, Aaron Stein, Vassilios Kapaklis, and Björgvin Hjörvarsson. Interaction modifiers in artificial spin ices. *Nature Physics*, 14(4):375, 2018.

[73] Vineeth Mohanan Parakkat, Kaichen Xie, and Kannan M. Krishnan. Tunable ground state in heterostructured artificial spin ice with exchange bias. *Phys. Rev. B*, 99:054429, Feb 2019.

[74] Linus Pauling. The structure and entropy of ice and of other crystals with some randomness of atomic arrangement. *Journal of the American Chemical Society*, 57(12):2680–2684, 1935.

[75] Yann Perrin, Benjamin Canals, and Nicolas Rougemaille. Extensive degeneracy, coulomb phase and magnetic monopoles in artificial square ice. *Nature*, 540(7633):410, 2016.

[76] Jonathan Perron, Luca Anghinolfi, Bharati Tudu, Nicolas Jaouen, J-M Tonnerre, Maurizio Sacchi, Frithjof Nolting, Jan Lüning, and Laura J Heyderman. Extended reciprocal space observation of artificial spin ice with x-ray resonant magnetic scattering. *Physical Review B*, 88(21):214424, 2013.

[77] Charlotte F Petersen, Alan Farhan, Scott Dhuey, Zuhuang Chen, Mikko J Alava, Andreas Scholl, and Sebastiaan Van Dijken. Tuning magnetic ordering in a dipolar square-kite tessellation. *Applied Physics Letters*, 112(9):092403, 2018.

[78] D Pomaranski, LR Yaraskavitch, S Meng, KA Ross, HML Noad, HA Dabkowska, BD Gaulin, and JB Kycia. Absence of pauling's residual entropy in thermally equilibrated dy 2 ti 2 o 7. *Nature Physics*, 9(6):353, 2013.

[79] JM Porro, A Bedoya-Pinto, A Berger, and P Vavassori. Exploring thermally induced states in square artificial spin-ice arrays. *New Journal of Physics*, 15(5):055012, 2013.

[80] Yi Qi, Todd Brintlinger, and John Cumings. Direct observation of the ice rule in an artificial kagome spin ice. *Physical Review B*, 77(9).

[81] Arthur Pdf Ramirez, A Hayashi, Robert Joseph Cava, R Siddharthan, and BS Shastry. Zero-point entropy in 'spin ice'. *Nature*, 399(6734):333, 1999.

[82] Ibon Recio and Joaquín J Torres. Emergence of low noise frustrated states in e/i balanced neural networks. *Neural Networks*, 84:91–101, 2016.

[83] Ph Refregier, E Vincent, J Hammann, and M Ocio. Ageing phenomena in a spin-glass: effect of temperature changes below tg. *Journal de Physique*, 48(9):1533–1539, 1987.

[84] Michael Reissner, Walter Steiner, Z Seidov, and G Guseinov. Mössbauer investigation of fe 0.5 in 1.5 s 3. In *ICAME 2005*, pages 1305–1308. Springer, 2006.

[85] Heiko Rieger, Ludger Santen, Ulrich Blasum, Martin Diehl, Michael Jünger, and Giovanni Rinaldi. The critical exponents of the two-dimensional ising spin glass revisited: exact ground-state calculations and monte carlo simulations. *Journal of Physics A: Mathematical and General*, 29(14):3939, 1996.

[86] M. Rojas, Onofre Rojas, and S. M. de Souza. Frustrated ising model on the cairo pentagonal lattice. *Phys. Rev. E*, 86:051116, Nov 2012.

[87] Nicolas Rougemaille, F Montaigne, Benjamin Canals, A Duluard, D Lacour, M Hehn, R Belkhou, Olivier Fruchart, S El Moussaoui, A Bendounan, et al. Artificial kagome arrays of nanomagnets: a frozen dipolar spin ice. *Physical Review Letters*, 106(5):057209, 2011.

[88] I. Rousochatzakis, A. M. Läuchli, and R. Moessner. Quantum magnetism on the cairo pentagonal lattice. *Phys. Rev. B*, 85:104415, Mar 2012.

[89] Michael Saccone, Kevin Hofhuis, David Bracher, Armin Kleibert, Sebastiaan van Dijken, and Alan Farhan. Elevated effective dimension in tree-like nanomagnetic cayley structures. *Nanoscale*, 12(1):189–194, 2020.

[90] Michael Saccone, Kevin Hofhuis, Yen-Lin Huang, Scott Dhuey, Zuhuang Chen, Andreas Scholl, Rajesh V Chopdekar, Sebastiaan van Dijken, and Alan Farhan. Dipolar cairo lattice: Geometrical frustration and short-range correlations. *Physical Review Materials*, 3(10):104402, 2019.

[91] Michael Saccone, Andreas Scholl, Sven Velten, Scott Dhuey, Kevin Hofhuis, Clemens Wuth, Yen-Lin Huang, Zuhuang Chen, Rajesh V. Chopdekar, and Alan Farhan. Towards artificial ising spin glasses: Thermal ordering in randomized arrays of ising-type nanomagnets. *Phys. Rev. B*, 99:224403, Jun 2019.

[92] Oles Sendetskyi, Luca Anghinolfi, Valerio Scagnoli, Gunnar Möller, Naëmi Leo, Aurora Alberca, Joachim Kohlbrecher, Jan Lüning, Urs Staub, and Laura Jane Heyderman. Magnetic diffuse scattering in artificial kagome spin ice. *Physical Review B*, 93(22):224413, 2016.

[93] David Sherrington and Scott Kirkpatrick. Solvable model of a spin-glass. *Phys. Rev. Lett.*, 35:1792–1796, Dec 1975.

[94] Dong Shi, Zoe Budrikis, Aaron Stein, Sophie A Morley, Peter D Olmsted, Gavin Burnell, and Christopher H Marrows. Frustration and thermalization in an artificial magnetic quasicrystal. *Nature Physics*, 14(3):309, 2018.

[95] Joseph Sklenar, Yuyang Lao, Alan Albrecht, Justin D Watts, Cristiano Nisoli, Gia-Wei Chern, and Peter Schiffer. Field-induced phase coexistence in an artificial spin ice. *Nature Physics*, 15(2):191, 2019.

[96] Nicolas Sourlas. Spin-glass models as error-correcting codes. *Nature*, 339(6227):693–695, 1989.

[97] J Stöhr, Y Wu, BD Hermsmeier, MG Samant, GR Harp, S Koranda, D Dunham, and BP Tonner. Element-specific magnetic microscopy with circularly polarized x-rays. *Science*, 259(5095):658–661, 1993.

[98] Robert H Swendsen and Jian-Sheng Wang. Replica monte carlo simulation of spin-glasses. *Physical review letters*, 57(21):2607, 1986.

[99] Y Tabata, H Kadowaki, Kazuyuki Matsuhira, Z Hiroi, N Aso, E Ressouche, and B Fåk. Kagome ice state in the dipolar spin ice dy 2 ti 2 o 7. *Physical review letters*, 97(25):257205, 2006.

[100] John Taylor. *Introduction to error analysis, the study of uncertainties in physical measurements*. 1997.

[101] DJ Thouless. Spin-glass on a bethe lattice. *Physical review letters*, 56(10):1082, 1986.

[102] Alexander A. Tsirlin, Ioannis Rousochatzakis, Dmitry Filimonov, Dmitry Batuk, Matthias Frontzek, and Artem M. Abakumov. Spin-reorientation transitions in the cairo pentagonal magnet $\mathbf{bi_4fe_5o_{13}F}$. *Phys. Rev. B*, 96:094420, Sep 2017.

[103] Arne Vansteenkiste, Jonathan Leliaert, Mykola Dvornik, Mathias Helsen, Felipe Garcia-Sanchez, and Bartel Van Waeyenberge. The design and verification of mumax3. *AIP advances*, 4(10):107133, 2014.

[104] EY Vedmedenko. Dynamics of bound monopoles in artificial spin ice: How to store energy in dirac strings. *Physical review letters*, 116(7):077202, 2016.

[105] 1 RF Wang, C Nisoli, Rafael Sá de Freitas, J Li, W McConville, BJ Cooley, MS Lund, Nitin Samarth, C Leighton, Vincent Henry Crespi, et al. Artificial 'spin ice'in a geometrically frustrated lattice of nanoscale ferromagnetic islands. *Nature*, 439(7074):303–306, 2006.

[106] Yong-Lei Wang, Zhi-Li Xiao, Alexey Snezhko, Jing Xu, Leonidas E Ocola, Ralu Divan, John E Pearson, George W Crabtree, and Wai-Kwong Kwok. Rewritable artificial magnetic charge ice. *Science*, 352(6288):962–966, 2016.

[107] Y-L Xie, Z-Z Du, Z-B Yan, and J-M Liu. Magnetic-charge ordering and phase transitions in monopole-conserved square spin ice. *Scientific reports*, 5:15875, 2015.

[108] Burcu Yucesoy, Jonathan Machta, and Helmut G Katzgraber. Correlations between the dynamics of parallel tempering and the free-energy landscape in spin glasses. *Physical Review E*, 87(1):012104, 2013.

[109] Sheng Zhang, Ian Gilbert, Cristiano Nisoli, Gia-Wei Chern, Michael J Erickson, Liam O'brien, Chris Leighton, Paul E Lammert, Vincent H Crespi, and Peter Schiffer. Crystallites of magnetic charges in artificial spin ice. *Nature*, 500(7464):553, 2013.